UC San Diego
UC San Diego Electronic Theses and Dissertations

Title

Inherent Area Selective Oxide deposition for Nanoscale Semiconductor Device Fabrication

Permalink
https://escholarship.org/uc/item/0tw9z7f2

Author
Cho, Yunil

Publication Date
2022

Peer reviewed|Thesis/dissertation

eScholarship.org Powered by the California Digital Library
University of California

UNIVERSITY OF CALIFORNIA SAN DIEGO

Inherent Area Selective Oxide deposition for Nanoscale Semiconductor Device Fabrication

A dissertation submitted in partial satisfaction of the
requirements for the degree Doctor of Philosophy

in

Electrical and Computer Engineering
(Nanoscale Devices and Systems)

by

Yunil Cho

Committee in Charge:

Professor Andrew C. Kummel, Chair
Professor Yu-Hwa Lo, Co-Chair
Professor Peter M. Asbeck
Professor Prabhakar Bandaru

2022

©

Yunil Cho, 2022

All Rights Reserved

The Dissertation of Yunil Cho is approved, and it is acceptable in quality and form for publication on microfilm and electronically.

University of California San Diego

2022

DEDICATION

This work is dedicated to my parent, who always believed in me and gave me this opportunity, and to my sister, who is preparing for the same challenge I am finishing now.

EPIGRAPH

"Failure is mother of Success"

TABLE OF CONTENTS

Dissertation Approval Page....................iii

Dedication....................iv

Epigraph....................v

Table of Contents....................vi

List of Symbols and Abbreviations....................viii

List of Figures....................ix

Acknowledgments....................xiii

Vita....................xv

Abstract of the Dissertation....................xvii

Chapter 1....................1
Inherently Selective Water-Free Deposition of Titanium Dioxide on the Nanoscale: Implication for Nanoscale Patterning

1.1 Abstract....................1

1.2 Introduction....................2

1.3 Experimental....................6

1.4 Results and Discussion....................9

1.4.1 TiO_2 ALD with $Ti(O^iPr)_4$ and AcOH....................9

1.4.2 TiO_2 ALD with $Ti(O^iPr)_4$ and HCO_2H....................15

1.4.3 TiO_2 single precursor thermal CVD with $Ti(O^iPr)_4$....................17

1.4.4 Nano-scale selectivity of TiO_2 CVD 22

1.5 Conclusions....................25

Chapter 2....................27

Inherent Selective Pulsed Chemical Vapor Deposition of Amorphous Hafnium Oxide / Titanium Oxide Nanolaminates

2.1 Abstract....27

2.2 Introduction....28

2.3 Experimental....32

2.4 Results and Discussion....36

2.4.1 Selectivity and crystallization study on single oxide film....36

2.4.2 Selectivity study of the HfO_2/TiO_2 nanolaminate film....40

2.4.3 Crystallization study of the HfO_2/TiO_2 nanolaminate film....46

2.4.4 Selectivity in nm scale region for the HfO_2/TiO_2 nanolaminate film....48

2.5 Conclusions....52

Chapter 3....54
Inherent Selective Pulsed Chemical Vapor Deposition of Aluminum Oxide in nm scale

3.1 Abstract....54

3.2 Introduction....55

3.3 Experimental....58

3.4 Results and Discussion....61

3.4.1 Selectivity of the AlO_x pulsed CVD with Aluminum tri-sec butoxide....61

3.4.2 Selectivity of the AlO_x pulsed CVD with Aluminum tri-sec butoxide and TMA....64

3.4.3 Mechanism and Nanoscale selectivity of the AlO_x pulsed CVD (TMA+ATSB)....73

3.4.4 Film Morphology and Electrical Characteristics of the AlO_x film....77

3.5 Conclusions....79

References....81

LIST OF SYMBOLS AND ABBREVIATIONS

Å	angstrom
AFM	atomic force microscopy
ALD	atomic layer deposition
CVD	chemical vapor deposition
EDX	Energy Dispersive X-ray
eV	electron volt
GIXRD	grazing incidence X-ray diffraction
I	electric current
µm	micrometer
MOSFET	metal oxide semiconductor field effect transistor
nm	nanometer
RMS	root mean square
SDDP	spacer defined double patterning
TEM	transmission electron microscopy
UHV	ultra-high vacuum
V	volts
XPS	x-ray photoelectron spectroscopy
XRD	x-ray diffraction

LIST OF FIGURES

Figure 1.1 Schematic showing the process for spacer defined double patterning................3

Figure 1.2 XPS chemical composition and AFM image of TiO_2 films after a total of 240 ALD cycles of $Ti(O^iPr)_4$ and AcOH at 250°C..10

Figure 1.3 AFM image of degreased SiCOH surface without any oxide deposition.........11

Figure 1.4 Carbon 1s XPS spectra of a TiO_2 film grown on Si after $Ti(O^iPr)_4$ and AcOH half-cycles at 250°C...12

Figure 1.5 Table showing each deposition, film thickness, and incremental thickness for each dosing process and XPS chemical composition during multiple pulses of $Ti(O^iPr)_4$ and AcOH on Si...13

Figure 1.6 Reaction schematic showing the ALD reaction between $Ti(O^iPr)_4$ and AcOH on Si/SiO_2 and SiCOH...14

Figure 1.7 XPS chemical composition and AFM image of TiO_2 films after 20 ALD cycles of $Ti(O^iPr)_4$ and HCO_2H at 250°C...16

Figure 1.8 XPS chemical composition and AFM after doses of $Ti(O^iPr)_4$ at 250°C and 295°C..18

Figure 1.9 GIXRD curves for Si and SiO_2 after TiO_2 CVD at 295°C...............................21

Figure 1.10 XPS chemical composition and AFM on SiO_2 after 400 $Ti(O^iPr)_4$ pulses at 300°C..21

Figure 1.11 XPS chemical composition of passivated SiCOH and passivated Cu/SiCOH nanoscale patterned sample before and after 300 pulses of $Ti(O^iPr)_4$ at 295°C................23

Figure 1.12 TEM of Selective TiO_2 deposition on a Cu/SiCOH patterned sample...........24

Figure 2.1 A Schematic of UHV chamber for HfO_2/TiO_2 nanolaminate CVD and XPS analysis......33
Figure 2.2 Analysis of Pulsed CVD TiO_2 Films at 300°C......36
Figure 2.3 Analysis of HfO_2 Pulsed CVD with $Hf(O^tBu)_4$ at 300°C......38
Figure 2.4 The chemical structures of $Ti(O^iPr)_4$ and $Hf(O^tBu)_4$ and the proposed reaction mechanism for the HfO_2/TiO_2 nanolaminate film......40
Figure 2.5 Analysis of 300°C Pulsed CVD of Highly Ti-rich HfO_2/TiO_2 Films......41
Figure 2.6 Analysis of Ti-rich HfO_2/TiO_2 nanolaminate Pulsed CVD at 300°C......43
Figure 2.7 Analysis of Hf-rich HfO_2/TiO_2 nanolaminate Pulsed CVD at 300°C......44
Figure 2.8 Film thickness on Si, SiO_2, and SiCOH for three different Hf:Ti ratio HfO_2/TiO_2 nanolaminates by pulsed CVD......45
Figure 2.9 AFM and XRD study on the Effect of Sublayer Thickness on Crystallinity....47
Figure 2.10 XPS of Selective CVD of Highly Ti-rich HfO_2/TiO_2 nanolaminates on a Nanoscale Patterned Sample......49
Figure 2.11 TEM Analysis of Selective CVD of a Highly Ti-rich HfO_2/TiO_2 nanolaminates on a Nanoscale Patterned Sample......50
Figure 2.12 Application of selective HfO_2/TiO_2 nanolaminate film deposition on gate electrodes......51
Figure 3.1 Analysis of the AlO_x pulsed CVD with ATSB at 300°C (10 seconds purge time)......61
Figure 3.2 Analysis of the AlO_x pulsed CVD with ATSB at 300°C (60 seconds purge time)......61

Figure 3.3 Analysis of the AlO_x pulsed CVD with ATSB at 300°C (240 seconds purge time)....................62
Figure 3.4 Analysis of the AlO_x pulsed CVD with ATSB at 330°C (10 seconds purge time)....................64
Figure 3.5 Analysis of AlO_x pulsed CVD with one pulse of TMA and 160 pulses of ATSB per supercycle at 300°C....................65
Figure 3.6 Analysis of AlO_x pulsed CVD with one pulse of TMA and 120 pulses of ATSB per supercycle at 300°C....................66
Figure 3.7 Analysis of AlO_x pulsed CVD with one pulse of TMA and 80 pulses of ATSB per supercycle at 300°C....................67
Figure 3.8 Analysis of AlO_x pulsed CVD with 120 pulses of ATSB and one pulse of TMA per supercycle (reverse order of precursors) at 300°C....................69
Figure 3.9 Analysis of AlO_x pulsed CVD with one pulse of TMA and 120 pulses of ATSB per supercycle at 330°C....................70
Figure 3.10 The growth curve of AlO_x pulsed CVD with ATSB on Si and SiO_2 at 300°C and at 330°C....................71
Figure 3.11 Analysis of AlO_x pulsed CVD with one pulse of TMA and 80 pulses of ATSB per supercycle at 330°C....................72
Figure 3.12 Proposed reaction mechanism of the AlO_x pulsed CVD with TMA and ATSB....................73
Figure 3.13 XPS of Selective AlO_x pulsed CVD with ATSB and TMA on a Cu/SiCOH Nanoscale Patterned Sample....................75

Figure 3.14 STEM Analysis of the Selective AlO_x pulsed CVD with ATSB and TMA on a Nanoscale Patterned Sample…..76

Figure 3.15 AFM image of AlO_x films on Si and SiO_2 deposited by the pulsed CVD with ATSB and TMA at 330°C..77

Figure 3.16 Electrical characteristics of the AlO_x film deposited by the pulsed CVD with ATSB and TMA at 330°C………..78

Figure 3.17 XPS chemical composition of the AlO_x film, deposited by the selective CVD with ATSB and TMA at 330°C, before and after each post-deposition anneal..................79

ACKNOWLEDGEMENTS

I would like to first thank my advisor, Professor Andrew Kummel, for his support and guidance throughout my Ph.D. course. He was always open to discussion and didn't hesitate to advise his vast knowledge of the semiconductor industry. I would also like to thank him for helping me find a job in the semiconductor industry.

Second, I would like to thank my lab mate James Huang for being the best lab mate anyone could hope for. We worked together on our research projects. As a team, we could solve various obstacles and achieve the research results. He was one of the diligent and kind men I worked with. I will miss having the privilege of working with James.

I would like to thank my senior colleagues, Dr. Jong Choi and Dr. Chris Ahles, for helping me settle into this lab. They taught me how to manage the UHV chamber and various things in the lab. They were also enjoyable people to play with. It was sad we only had a short time together in the lab. Without them, my 1st year in the lab would be more challenging.

I would like to acknowledge all the current and previous members of the group for always being more than willing to help in the lab and for all of the great times we had: Dr. Steven Wolf, Dr. Michael Breeden, Dr. Scott Ueda, Victor Wang, Jimmy Kuo, Ashay Anurag, Aaron McLeod, Harshil Kashyap, Ping Che Lee, Chelsea Swank-Anderson, Changyoung Kim, SeongUk Kim, and Woojae Lee. In addition, I want to thank Zichen Zhang and Kesong Wang for helping my experiments when I needed some experiment or analysis from NANO3.

I want to thank my committee members for actively participating in my Qualifying exam and thesis defense presentations. My committee includes Professor Andrew Kummel, Professor Peter Asbeck, Professor Prbhakar Bandaru, and Professor Yu-Hwa Lo.

I want to give my thanks for the continuous care and support from my family. I would like to thank my parent, Hyuck Cho and Namsu Ann, for always believing in me and supporting me. I would like to thank my sister Kyungmin Cho who could share the common experiences and difficulties while living and studying abroad.

I want to acknowledge that this work was funded by Applied Materials.

Chapter 1, in full, is a reprint of the material as it appears in ACS Applied Nano Materials. Y. Cho, C. F. Ahles, J. Y. Choi, J. Huang, A. Jan, K. Wong, S. D. Nemani, E. Yieh, and A.C. Kummel, "Inherently Selective Water-Free Deposition of Titanium Dioxide on the Nanoscale: Implications for Nanoscale Patterning", *ACS Appl. Nano Mater.5, 1, 476-485 (2022).* The dissertation author was the primary investigator and author of this paper.

Chapter 2, in full, is a reprint of the material as it appears in Applied Surface Science. Y. Cho, J. Huang, C.F. Ahles, Z. Zhang, K. Wong, S. D. Nemani, E. Yieh, and A.C. Kummel, "Inherent Selective Pulsed Chemical Vapor Deposition of Amorphous Hafnium Oxide / Titanium Oxide Nanolaminates", *Applied Surface Science vol.600*, 154010 (2022). The dissertation author was the primary investigator and author of this paper.

Chapter 3, in full, is currently being prepared for submission for publication of the material. Y. Cho, J. Huang, Z. Zhang, K. Wang, P.C. Lee, C. Kim, K. Wong, S. D. Nemani, E. Yieh, and A.C. Kummel. The dissertation author was the primary investigator and author of this material.

VITA

EDUCATION

2012 Bachelor of Science in Electrical Engineering, Korea Advanced Institute of Science and Technology

2014 Master of Science in Electrical Engineering, Korea Advanced Institute of Science and Technology

2022 Doctor of Philosophy in Electrical and Computer Engineering (Nanoscale Devices and Systems), University of California San Diego

PUBLICATIONS

• S.M. Lee, **Y. Cho**, D.Y. Kim, J.S. Chae and K.C. Choi, "Enhanced Light Extraction from Mechanically Flexible Nanostructured Organic Light-Emitting Diodes with Plasmonic Nanomesh Electrodes",*Advanced Optical Materials vol.3*, 1240-1247, 2015.

• J.Y. Choi, C.F. Ahles, **Y. Cho**, A. Anurag, K.T. Wong, S.D. Nemani, E. Yieh and A.C. Kummel, "Selective Pulsed chemical vapor deposition of water-free HfO_x on Si in preference to SiCOH and passivated SiO_2", *Applied Surface Science vol.512*, 145733, 2020.

• **Y. Cho**, C.F. Ahles, J.Y. Choi, J. Huang, A. Jan, K. Wong, S. D. Nemani, E. Yieh, and A.C. Kummel, "Inherently Selective Water-Free Deposition of Titanium Dioxide on the Nanoscale: Implications for Nanoscale Patterning", *ACS Appl. Nano Mater.5, 1, 476-485, 2022.*

- J. Huang, **<u>Y. Cho</u>**, Z. Zhang, A. Jan, K. T. Wong, S. D. Nemani, E. Yieh, and A.C. Kummel, "Selective Pulsed Chemical Vapor Deposition of Water-Free TiO_2/Al_2O_3 and HfO_2/Al_2O_3 Nanolaminates on Si and SiO_2 in preference to SiCOH", *ACS Appl. Nano Mater.5, 1, 476-485, 2022.*

- **<u>Y. Cho</u>**, J. Huang, C.F. Ahles, Z. Zhang, K. Wong, S. D. Nemani, E. Yieh, and A.C. Kummel, "Inherent Selective Pulsed Chemical Vapor Deposition of Amorphous Hafnium Oxide / Titanium Oxide Nanolaminates", *Applied Surface Science vol.600*, 154010, 2022.

- **<u>Y. Cho</u>**, J. Huang, Z. Zhang, K. Wang, P.C. Lee, C.Y. Kim, K. Wong, S. D. Nemani, E. Yieh, and A.C. Kummel, "Inherent Selective Pulsed Chemical Vapor Deposition of Aluminum Oxide in nanometerscale", In prep.

FIELD OF STUDY

Major Field: Electrical and Computer Engineering

Studies in Surface Science and Physical Chemistry
Professor Andrew C. Kummel

ABSTRACT OF THE DISSERTATION

Inherent Area Selective Oxide deposition for

Nanoscale Semiconductor Device Fabrication

by

Yunil Cho

Doctor of Philosophy in Electrical and Computer Engineering
(Nanoscale Devices and Systems)

University of California San Diego, 2022

Professor Andrew C. Kummel, Chair
Professor Yu-Hwa Lo, Co-Chair

Nanoscale fabrication is the key issue in the fabrication of leading-edge commercial semiconductor devices. Selective deposition methods are being developed to use in conjunction with double patterning techniques for nanoscale patterning. The need for selective deposition is acute in backend metallization when multiple metals and low k dielectric layers (SiCOH) with high aspect ratios are employed. The selective oxide deposition can also be applied in nanoscale fabrication for various purposes, such as etch stop layer and dielectric-on-dielectric structure. For selective oxide deposition in backend

fabrication, water-free deposition is more desirable since it can not only induce higher selectivity but also prevent damage to metals and SiCOH.

This study studied the inherent selective deposition of various oxides on Si and SiO_2 in preference to SiCOH. SiCOH is alkyl ($-C_xH_y$) terminated SiO_2, used as a non-reactive surface. Through the reactivity difference between precursors and different surfaces, inherent selective deposition was achieved. The selective oxide deposition was also tested in the nm scale patterned region to check whether the process can be applied in nanoscale fabrication.

Chapter 1 of this dissertation describes the inherent selective TiO_2 deposition process. The process showed >10 nm of selective TiO_2 deposition and insight into using metal alkoxide precursor in a single precursor pulsed thermal CVD process. However, the TiO_2 CVD process showed the limit of the process; the selectively deposited TiO_2 film became rough due to the crystallization.

Chapter 2 of this dissertation describes the inherent selective HfO_2/TiO_2 nanolaminates pulsed CVD process. To solve the film roughness issue from Chapter 1, the nanolaminate structure of two different oxides was studied. The selective HfO_2/TiO_2 nanolaminate CVD process showed >10 nm of selective and amorphous HfO_2/TiO_2 nanolaminate deposition, which obtained selective deposition and smooth film.

Chapter 3 of this dissertation describes the inherent selective AlO_x pulsed CVD process. As AlO_x stays amorphous when the thickness increases and is easier to etch compared to the nanolaminate structure of two different oxides from Chapter 2, this process can be an ideal selective oxide deposition process for nanoscale fabrication as a spacer or etch stop layer.

Chapter 1

Inherently Selective Water-Free Deposition of Titanium Dioxide on the Nanoscale: Implications for Nanoscale Patterning

1.1 Abstract

Water-free inherent selective deposition of TiO_2 on Si and SiO_2 in preference to SiCOH has been studied via atomic layer deposition (ALD) and pulsed chemical vapor deposition (CVD). SiCOH is a non-reactive low-k dielectric material, consisting of highly porous alkylated SiO_2. Water-free deposition was studied to protect SiCOH and increase selectivity. The titanium precursor used in all studies was $Ti(O^iPr)_4$ (titanium(IV) isopropoxide) and contains four oxygen atoms enabling it to form TiO_2 through single precursor CVD. At 250°C substrate temperature, selective water-free ALD of TiO_2 using $Ti(O^iPr)_4$ and either acetic acid (AcOH) or formic acid (HCO_2H) as a second precursor was studied. By the both ALD processes, around 2 nm of TiO_2 was deposited on Si and SiO_2 without any deposition on SiCOH. The TiO_2 ALD films had an RMS roughness of 2-3 Å. In-situ X-ray photoelectron spectroscopy (XPS) showed that $Ti(O^iPr)_4$ + AcOH ALD occurred via ligand exchange between -OiPr and AcO-. Atomic layer deposition with formic acid, which is a 10x stronger proton donor than acetic acid, displayed similar selectivity but with a 10x higher growth rate than ALD with acetic acid. Single precursor pulsed CVD with $Ti(O^iPr)_4$ was also studied at 250 ˚C and 295 ˚C substrate temperatures. At 250 °C, TiO_2 growth on any substrate was minuscule (< 1 nm for 400 pulses). Single precursor pulsed CVD (2,000 pulses) at 295°C displayed the highest selectivity among all processes studied: 16.9 nm and 40.1 nm TiO_2 were deposited on Si and SiO_2, respectively, while less than a monolayer of TiO_2 was deposited on SiCOH. The pulsed CVD at 295°C showed ~20 nm of

selective TiO_2 deposition on nanoscale patterned samples. It is expected that the selective TiO_2 CVD can be applicable in nanoscale patterning process in metal oxide semiconductor field effect transistor (MOSFET) fabrication.

1.2 Introduction

Atomic layer deposition (ALD) and chemical vapor deposition (CVD) are widely used techniques in the semiconductor industry. Atomic layer deposition uses self-limiting chemical reactions in which an oxidant (for example H_2O) and a reductant (typically an organometallic precursor) are pulsed into a vacuum chamber containing the substrate in succession (half cycles); in each half cycle, ligand exchange occurs between surface species and gaseous precursor species. Thermal CVD is typically performed using oxidizing and reducing precursors that are continuously and simultaneously dosed into a chamber containing the substrate at a higher sample temperature than ALD. The increased surface temperature results in decomposition of the precursors and reaction to form a thermodynamically favorable material. For CVD of oxide materials, this leaves a highly reactive surface terminated by hydroxyl (-OH) groups, which then react with further precursor to quickly deposit the material of interest.[1] While ALD is self-limiting in reaction progression and typically forms smooth and conformal films, CVD dosing conditions must be carefully controlled to produce smooth and conformal films.[2]

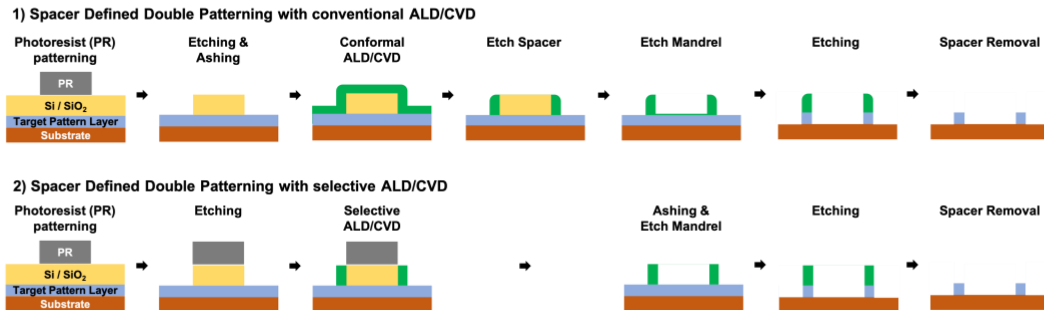

Figure 1.1 Schematic showing the process for spacer defined double patterning (SDDP) With 1) conventional ALD/CVD and 2) selective ALD/CVD. Selective oxide deposition enables a reduction in the number of process steps (etch spacer step).

ALD and CVD methods have been used in the semiconductor industry[3], and selective deposition may enable their use in nanoscale fabrication.[4] For example, selective oxide deposition can be integrated into patterning methods such as spacer defined double patterning (SDDP). This method can reduce the mask misalignment issue during MOSFET scaling.[5,6] Conventional non-selective ALD and CVD can also be employed in SDDP; however, selective deposition reduces the number of process steps (etch spacer step), as shown in Figure 1.1, which can reduce cost and time.

Three selective deposition methods can be used: inherent selective deposition, selective passivation, and selective activation. Inherent selective deposition is based on the reactivity difference for precursor mediated chemisorption of one or both precursors on different surfaces. This method is most desirable because it requires only one step for the selective deposition; however, only limited research has been reported.[7-10] The majority of current selective depositions relies on selective passivation, where a molecule, such as long chain alkane, selectively reacts on a specific surface and prevents any deposition on that

surface.[11-15] Selective activation, which induces deposition only on the surface with certain pretreatments (e.g. electron beam induced deposition), has also been reported.[16-19]

For highly selectivity oxide deposition, it is preferred to have an oxygen source other than water (H_2O), e.g. a metal alkoxide precursor or a carboxylic acid, since water can react on almost any surface and induce oxidation. There have been many reports of TiO_2 deposition via ALD and CVD including water-free ALD of TiO_2 using $Ti(O^iPr)_4$ and $TiCl_4$.[1,20,21] There are two mechanisms for the combination of these two precursors, depending on the sample temperature.[21] The chemical equations for each mechanism are shown below.

1. Low temperature (125-225 °C)

$$\text{Si-O-H}_{(s)} + \text{Ti-[O-C-(CH}_3)_2]_4\,_{(g)} \rightarrow \text{Si-O-Ti-[O-C-(CH}_3)_2]_3\,_{(s)} + \text{H-O-C-(CH}_3)_2\,_{(g)}$$

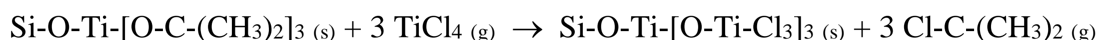

$$\text{Si-O-Ti-[O-C-(CH}_3)_2]_3\,_{(s)} + 3\ \text{TiCl}_4\,_{(g)} \rightarrow \text{Si-O-Ti-[O-Ti-Cl}_3]_3\,_{(s)} + 3\ \text{Cl-C-(CH}_3)_2\,_{(g)}$$

2. High temperature (250-300 °C)

$$\text{Ti-[O-C-(CH}_3)_2]_4\,_{(physisorbed)} \rightarrow \text{Ti-[O-H]}_4\,_{(physisorbed)} + 4\ [\text{C-C}_2\text{H}_5]_{(g)}$$

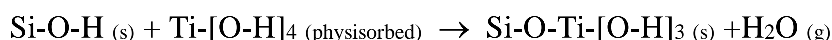

$$\text{Si-O-H}_{(s)} + \text{Ti-[O-H]}_4\,_{(physisorbed)} \rightarrow \text{Si-O-Ti-[O-H]}_3\,_{(s)} + \text{H}_2\text{O}_{(g)}$$

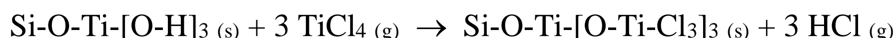

$$\text{Si-O-Ti-[O-H]}_3\,_{(s)} + 3\ \text{TiCl}_4\,_{(g)} \rightarrow \text{Si-O-Ti-[O-Ti-Cl}_3]_3\,_{(s)} + 3\ \text{HCl}_{(g)}$$

At low temperature (125-225 °C), $Ti(O^iPr)_4$ reacts on the surface and produces Ti-O-^{i}Pr adsorbates. Sequentially dosed $TiCl_4$ reacts with this -O-^{i}Pr ligand on the surface and produces Ti-O-Ti bonds. Conversely at high temperature (250-300 °C), the Ti-O-^{i}Pr bonds on the physisorbed $Ti(O^iPr)_4$ thermally decompose and form hydroxyl ligands (Ti-OH bonds). The hydroxyl ligands react with subsequential $TiCl_4$ to produce Ti-O-Ti bonds. To summarize the reaction mechanism at high/low temperature, ALD reaction is dominated at low temperature, but at high temperature, the reaction is a mixture of thermal CVD and ALD.

The drawback of this process is that halogens e.g. Cl, can corrode metals, so that this process is incompatible with middle or back of the line processing.

Water-free TiO_2 ALD using $Ti(O^iPr)_4$ and AcOH was also reported with the mechanism below.[22]

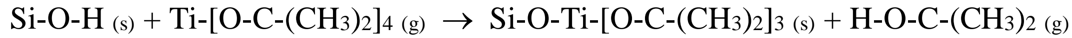

$$Si\text{-}O\text{-}H_{(s)} + Ti\text{-}[O\text{-}C\text{-}(CH_3)_2]_{4\,(g)} \rightarrow Si\text{-}O\text{-}Ti\text{-}[O\text{-}C\text{-}(CH_3)_2]_{3\,(s)} + H\text{-}O\text{-}C\text{-}(CH_3)_{2\,(g)}$$

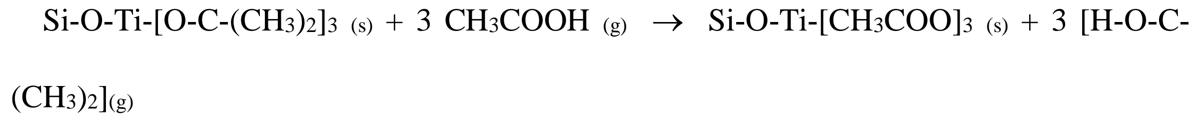

$$Si\text{-}O\text{-}Ti\text{-}[O\text{-}C\text{-}(CH_3)_2]_{3\,(s)} + 3\ CH_3COOH_{(g)} \rightarrow Si\text{-}O\text{-}Ti\text{-}[CH_3COO]_{3\,(s)} + 3\ [H\text{-}O\text{-}C\text{-}(CH_3)_2]_{(g)}$$

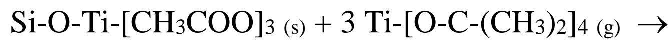

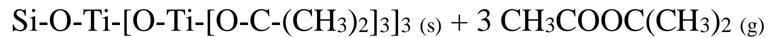

$$Si\text{-}O\text{-}Ti\text{-}[CH_3COO]_{3\,(s)} + 3\ Ti\text{-}[O\text{-}C\text{-}(CH_3)_2]_{4\,(g)} \rightarrow Si\text{-}O\text{-}Ti\text{-}[O\text{-}Ti\text{-}[O\text{-}C\text{-}(CH_3)_2]_3]_{3\,(s)} + 3\ CH_3COOC(CH_3)_{2\,(g)}$$

In this study, $Ti(O^iPr)_4$ reacts on Si-OH surface and produces Ti-O-^{i}Pr adsorbates at 200 °C. Subsequently dosed CH_3COOH (AcOH) performs a ligand exchange reaction with -O-^{i}Pr ligand on the surface and produces Ti-OAc bonds. This Ti-OAc then further reacts with $Ti(O^iPr)_4$ and forms Ti-O-Ti-O-^{i}Pr bonds; subsequent ALD cycles thus deposit TiO_2 films. These processes do not use H_2O as a second precursor, which protects low-k dielectrics (SiCOH) and increases the probability of selective deposition; however, selective deposition was not reported.

In this study, water-free inherent selective ALD and CVD of TiO_2 using $Ti(O^iPr)_4$ and HCO_2H or AcOH on Si, SiO_2, and SiCOH was investigated. $Ti(O^iPr)_4$ is a metal alkoxide precursor which contains oxygen atom in each ligand, so that this precursor can not only be used in ALD reactions but also be employed for unimolecular thermal CVD. HCO_2H and AcOH are the second precursors for ALD reaction. SiCOH, which is alkylated porous SiO_2,

has Si-OC_xH_y or Si-C_xH_y groups on the surface and does not contain reactive sites such as -OH groups. Therefore, SiCOH in this sample set was used as the non-reactive surface.[23-26]

ALD reactions with both second precursors were performed at 250 °C substrate temperature. Both ALD showed ~2 nm of smooth (2-3 Å RMS roughness) TiO_2 deposition on Si and SiO_2 before appreciable deposition (~0.4 nm) was observed on SiCOH. The single precursor pulsed CVD at 295 °C showed even higher selectivity with ~17 nm and ~40 nm films of TiO_2 on Si and SiO_2, respectively. With ~20 nm of selective deposition on nanoscale region, the pulsed CVD process showed its potential in nanoscale semiconductor fabrication, such as nanoscale patterning by merging with SDDP. However, high roughness (> 1nm RMS roughness) due to the presence of nanocrystalline grains on the surface need to be resolved for its application in nanoscale patterning, using known techniques such as nanolaminate formation.[27,28]

1.3 Experimental

In this study, selective ALD and CVD were tested on three different substrates: Si, SiO_2 and SiCOH. Each substrate was diced and degreased with acetone, methanol and deionized water for 15 seconds. To remove the surface native oxide, degreased Si and SiO_2 substrates were immersed in a 0.5% hydrofluoric acid solution for 30 seconds. After the cleaning process, substrates were loaded to the UHV chamber on a single sample holder to go through same dosing process.

Patterned Cu on SiCOH substrates were used to examine selective deposition in nanoscale features. These substrates degreased using the process previously described. Since the SiCOH region of the patterned sample was damaged from the initial fabrication process

and, therefore, not fully terminated with -OC_xH_y or -C_xH_y groups, an additional passivation was performed with a proprietary passivation process from Applied Materials.

ALD and CVD were performed in a home-made reaction chamber. The precursor dosing was controlled by pneumatic valves and no carrier gas was used. Each precursor was transferred to a glass precursor bottle and connected to the chamber. The $Ti(O^iPr)_4$ bottle was heated up to 80 °C while the AcOH and HCO_2H bottles were kept at room temperature (~21 °C). A constant N_2 purge was used to evacuate residual precursor from the chamber. All of the precursor dosings were controlled with the pressure inside the reaction chamber. The constant N_2 purge was controlled by a needle valve, and the pressure size of the precursor pulse was controlled by the precursor bottle temperature and the pneumatic valve open time. The dosing time for $Ti(O^iPr)_4$ were set to 50 ms to keep the pressure size rise small to avoid unwanted CVD reaction. The dosing times for AcOH and HCO_2H were set to 90ms (AcOH) and 60ms (HCO_2H) to have similar size second precursor pressure. During single precursor TiO_2 CVD, $Ti(O^iPr)_4$ were dosed with the above dosing conditions. For ALD and CVD, multiple short precursor pulses are commonly used instead of single long pulses to avoid pumping high pressures with the turbomolecular pump. The repeated short pulses also allow time for residues to desorb from the reaction surface in ALD reactions and in unimolecular pulsed CVD reactions. Between each $Ti(O^iPr)_4$ pulse, a 5 second purge was used to remove residual precursor and reaction byproducts. For the ALD process to deposit appreciable TiO_2, 20 pulses of $Ti(O^iPr)_4$ were required per 1 pulse of AcOH or HCO_2H. The purge duration between $Ti(O^iPr)_4$ and the second precursor (AcOH or HCO_2H) was 60 seconds.

After deposition, each sample was transferred to an X-ray photoelectron spectroscopy (XPS) system for *in-vacuo* XPS analysis. The XPS measurement used a

monochromatic Al Kα source (1486.7 eV) with an XM 1000 MkII/SPHERA X-ray source from Omicron Nanotechnology. The spectra were measured with constant analyzer energy with a pass energy of 50 eV and a step width of 0.1 eV. The angle between the analyzer normal and the sample surface was 30°. The peak shape analysis was performed with CASA XPS v.2.3 program using Shirley background subtraction. After deposition and XPS, atomic force microscopy (AFM) and grazing incidence X-ray diffraction (GIXRD) were performed ex situ.

The TiO_2 film thickness was derived using the inelastic mean free path (IMFP) and attenuation length of an electron from the Si substrate as below.[6]

$$t = \lambda \sin\theta \, ln(\frac{I_0}{I})$$
$$\lambda = \frac{143}{E^2} + 0.054\sqrt{E}$$

t is the film thickness on the substrate, λ is the IMFP of the electrons from the Si substrate, θ is the angle of an emitted electron from the surface, I is the intensity of the substrate signal (after deposition), I_0 is the intensity of the unattenuated substrate signal (before deposition), and E is the kinetic energy of the electrons. The thickness derived from the equation above showed similar thickness (a few angstrom difference) compare to the thickness from the ellipsometry. However, if the deposition on the Si substrate exceeds ~4 nm, the Si substrate peak is fully attenuated (I=0), and the above equation is not applicable. Therefore, when the Si substrate peak was fully attenuated, the thickness was measured with ex-situ ellipsometry. When the deposition was below ~1 nm, it is possible that the deposition is not a continuous film and only TiO_2 nuclei are present. However, even for sub 1 nm films, the XPS attenuation equation was employed to determine a nominal film thickness.

1.4 Results and Discussion

1.4.1 TiO_2 ALD with $Ti(O^iPr)_4$ and AcOH

Consistent with previous research on water-free ALD by K. Ramos *et al.*[21], the selective ALD of TiO_2 using $Ti(O^iPr)_4$ and AcOH was tested on Si, SiO_2, and SiCOH. Each ALD cycle contained 20 pulses of $Ti(O^iPr)_4$ and 1 pulse of AcOH, as mentioned in detail in the Experimental section. Figure 1.2 shows the chemical composition as determined by XPS of three samples and AFM images of the surfaces after the TiO_2 deposition. The XPS results show that after the first 40 ALD cycles, 10% and 8% of Ti were detected on Si and SiO_2 surfaces, while no significant Ti was detected from SiCOH surface. After additional 100 ALD cycles, 1.7 nm and 1.3 nm of TiO_2 was deposited on Si and SiO_2. The thicknesses of TiO_2 films were calculated based on attenuation of Si substrate signals.[6] After these 100 additional cycles, nucleation was observed on SiCOH with 3% of Ti, which is still less than a monolayer of TiO_2 (~0.4 nm)[29]. After an additional 100 ALD cycles (240 ALD cycles total), the thickness of TiO_2 was 2.8 nm on Si and 2.3 nm on SiO_2. Since XPS is a surface-sensitive measurement, as deposition increases beyond ~2 nm with the same deposition process, TiO_2 films with similar O, C, Ti ratio are deposited and show nearly constant O, C, and Ti XPS fractions. The TiO_2 thickness on Si and SiO_2 were similar in 2-3 nm range as AcOH reacted on both surfaces and induced similar reactivities on both surfaces; it is likely both surface had sufficient -OAc group to nucleate reaction with the precursors. On SiCOH, 0.4 nm of TiO_2 film had accumulate; nucleation was slower on SiCOH than on Si and SiO_2.

This is consistent with Si-OC_xH_y or Si-C_xH_y groups on the SiCOH surface preventing reaction with precursors thus inducing inherently selective deposition.

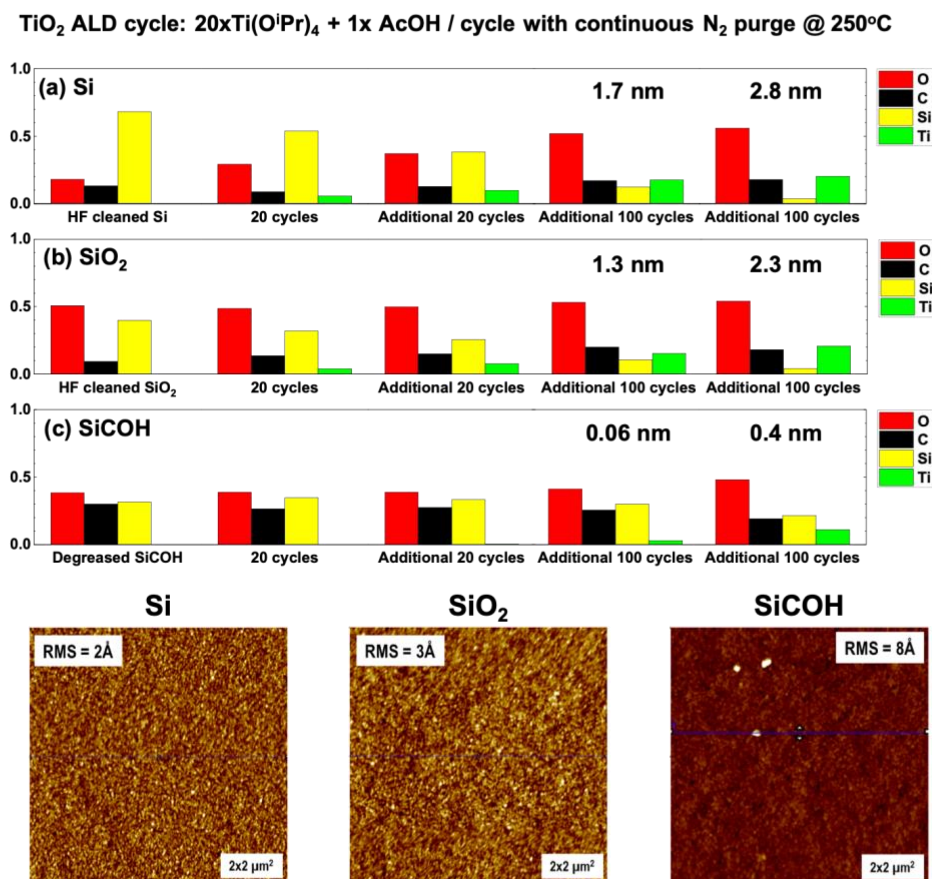

Figure 1.2 XPS chemical composition (Above) and AFM image (Below) of TiO_2 films after a total of 240 ALD cycles of Ti(O^{i}Pr)$_4$ and AcOH at 250 °C. (a) On HF etched Si: 2.8nm of TiO_2 was deposited and the film was smooth with an RMS roughness of 2 Å. (b) On HF etched SiO_2: 2.3 nm of TiO_2 was deposited and the film was smooth with a RMS roughness of 3 Å. (c) On Degreased SiCOH: ~0.4nm of TiO_2 was deposited (calculated based on attenuation of Si substrate signal), and the surface RMS roughness was 8 Å with several ~6nm particles which were present on the SiCOH surface prior to deposition.

After deposition, *ex situ* AFM was performed to quantify the surface morphology (Figure 1.2.). The TiO_2 film on Si, which had total thickness of 2.8 nm, showed 2 Å RMS roughness. The TiO_2 on SiO_2, which had total thickness of 2.3 nm, showed 3 Å RMS roughness. Both films were smooth with low RMS roughness and no significant particles. The TiO_2 on SiCOH, which had total thickness of 0.4 nm, showed 8 Å RMS roughness. Several particles with ~6 nm height were detected on the SiCOH surface. However, these particles with high RMS roughness were also observed on a degreased SiCOH surface with no deposition as shown in Figure 1.3. Since the deposition tends to occur earlier on heterogeneous surfaces such as step edges or defect sites, which are plentiful on particles and high roughness surfaces[10], it might be possible to obtain higher selectivity if SiCOH with lower surface roughness was employed.

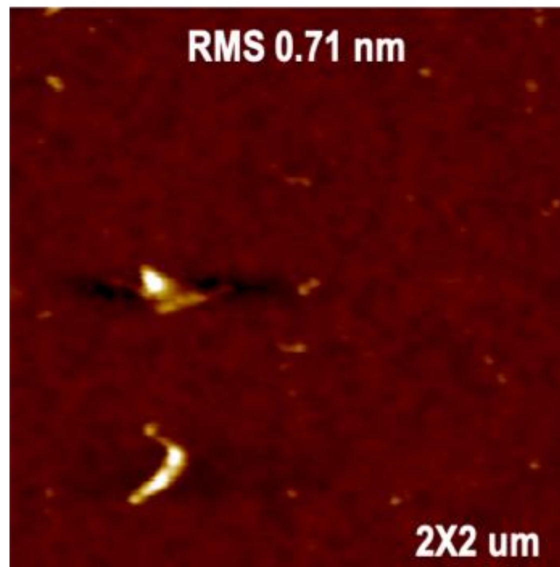

Figure 1.3 AFM image of degreased SiCOH surface without any oxide deposition. Several particles are observed which can be mistakenly interpreted as TiO_2 nuclei when a small amount of oxide is deposited on SiCOH.

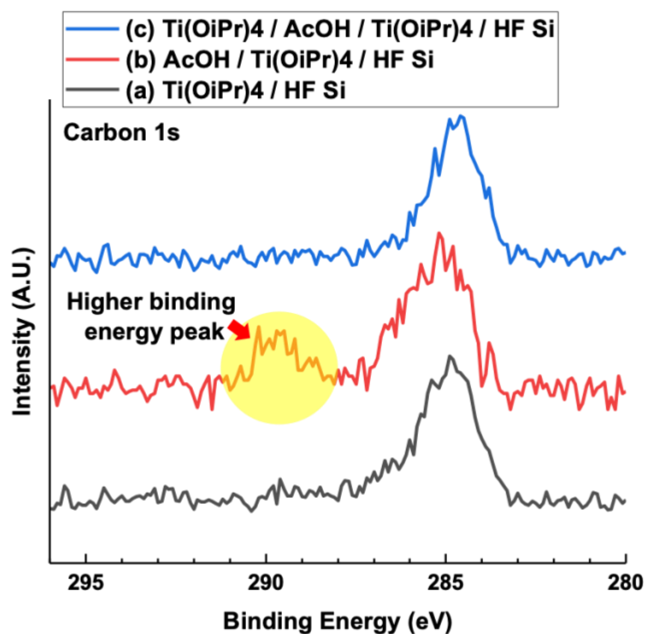

Figure 1.4 Carbon 1s XPS spectra of a TiO_2 film grown on Si after $Ti(O^iPr)_4$ and AcOH half-cycles at 250 °C. (a) The Carbon 1s peak after a total 2,000 pulses of $Ti(O^iPr)_4$ at 250 °C. (b) The Carbon 1s peak after dosing AcOH. (c) The Carbon 1s peak after additional dosing of $Ti(O^iPr)_4$

To verify the TiO_2 ALD reaction between $Ti(O^iPr)_4$ and AcOH, the reaction mechanism was studied with XPS. Figure 1.4 shows the carbon 1s XPS spectra of a TiO_2 film grown on Si after sequential doses of each precursor at 250 °C. Each curve was the sum of 10 XPS sweeps to reduce the background noise. After 2,000 pulses of $Ti(O^iPr)_4$, nucleation occurred on the Si surface, and carbon had a binding energy of 284-287 eV (Figure 1.4a) which corresponds to the $Ti\text{-}O^iPr$ bonds.[30] When AcOH was sequentially dosed, a peak at higher binding energy appeared (Figure 1.4b). This higher binding energy peak is consistent with surface -OAc bonds from -OAc groups remaining on the surface after AcOH doses. However, the subsequently dosed $Ti(O^iPr)_4$ had the ligand exchange with surface -OAc bond and bonded on the surface (Figure 1.4c). Due to this ligand exchange, the -OAc bonds were

removed, and -OiPr bonds were on the surface. Consequently, the Figure 1.4c spectrum did not have a high binding energy peak but showed similar binding energy to Figure 3a spectrum. The XPS spectra show that the precursors in each half cycle had ALD reactions with ligand exchange.

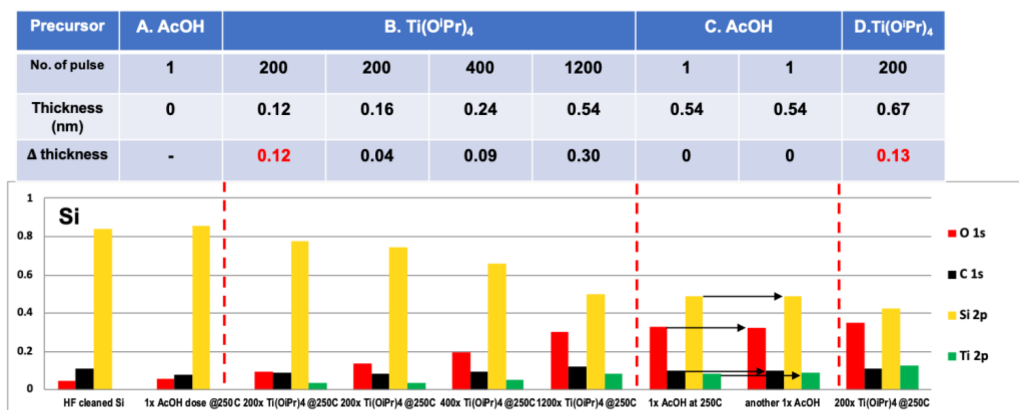

Precursor	A. AcOH	B. $Ti(O^iPr)_4$				C. AcOH		D.$Ti(O^iPr)_4$
No. of pulse	1	200	200	400	1200	1	1	200
Thickness (nm)	0	0.12	0.16	0.24	0.54	0.54	0.54	0.67
Δ thickness	-	0.12	0.04	0.09	0.30	0	0	0.13

Figure 1.5 Table showing each deposition, film thickness, and incremental thickness for each dosing process (above) and XPS chemical composition during multiple pulses of $Ti(O^iPr)_4$ and AcOH on Si (below).

In addition, an experiment on TiO_2 growth with multiple pulses of $Ti(O^iPr)_4$ and AcOH showed that the TiO_2 growth is mainly due to the ALD reaction between $Ti(O^iPr)_4$ and AcOH with a minor thermal CVD component from $Ti(O^iPr)_4$ as shown in Figure 1.5. Analysis of thickness increase after multiple pulses of $Ti(O^iPr)_4$ and AcOH half cycles was performed to check the self-limiting behavior of each precursor. One pulse of AcOH (A) and 200 $Ti(O^iPr)_4$ pulses at 250 °C showed ~0.12 nm TiO_2 deposition. However, additional 1,800 $Ti(O^iPr)_4$ pulses at 250 °C showed continuous film growth, meaning $Ti(O^iPr)_4$ thermally decomposed at 250 °C (B). However, this thermal CVD growth is small: 200 $Ti(O^iPr)_4$ pulses at 250 °C deposited ~0.04 nm film growth; in contrast, ALD with $Ti(O^iPr)_4$ and AcOH at 250 °C showed ~0.12 nm film growth with the same amount of $Ti(O^iPr)_4$. In the 2nd round of

AcOH dosing (C), AcOH dosing at 250 °C was doubled. However, XPS did not show any change from the additional AcOH pulse, as arrowed in Figure 1.5. In addition, sequentially dosed 200 $Ti(O^iPr)_4$ at 250 °C pulses showed 0.13nm growth, which is similar to the growth after the 1st 200 $Ti(O^iPr)_4$ pulses with 1 AcOH pulse (A). This result implies that AcOH has the saturation behavior. In conclusion, the ALD process with $Ti(O^iPr)_4$ and AcOH at 250 °C has a small CVD component due to the thermal decomposition of $Ti(O^iPr)_4$; however, the growth mainly occurred from the ALD reaction between the two precursors.

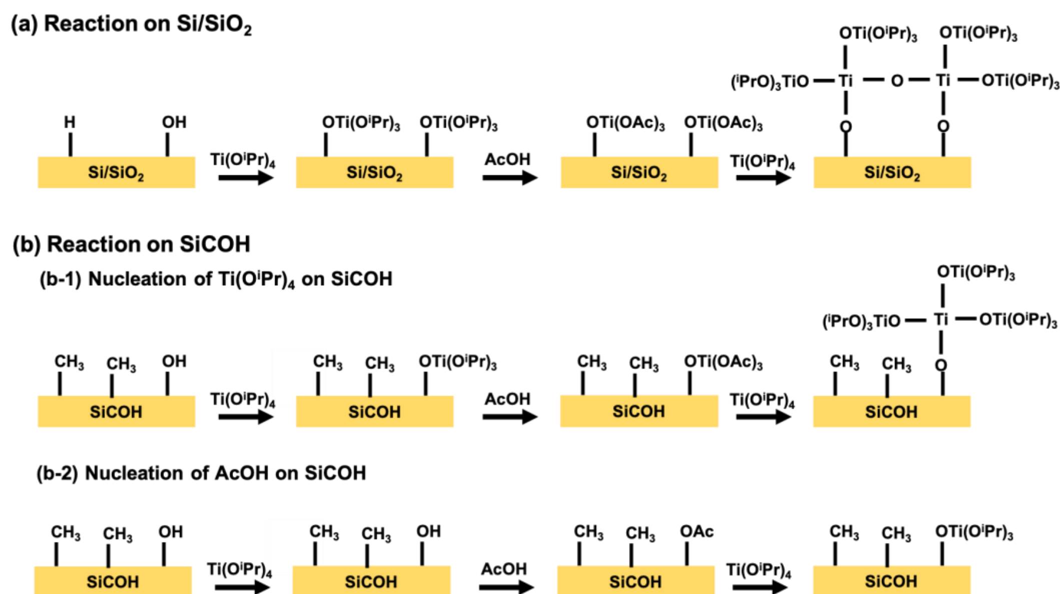

Figure 1.6 Reaction schematic showing the ALD reaction between $Ti(O^iPr)_4$ and AcOH on Si/SiO_2 and SiCOH. (a) On Si/SiO_2, as each precursor is sequentially dosed, ligand exchange between $-O^iPr$ and -OAc bonds occurs and forms TiO_2. (b) SiCOH surface is predominantly terminated with alkyl groups. Therefore, $Ti(O^iPr)_4$ (b-1) and AcOH (b-2) can react only on a small number of -OH defects, but these induce the loss of selectivity.

The carbon X-ray photoelectron spectra study confirmed the ALD mechanism as shown in Figure 1.6. On Si/SiO_2, $Ti(O^iPr)_4$ starts to nucleate on the surface and forms -O-Ti-O^iPr bonds. As AcOH is subsequently dosed, ligand exchange between $-O^iPr$ and -OAc

occurs and forms surface bound -O-Ti-OAc. The higher binding energy carbon 1s peak from Figure 1.4b is from the -OAc group. This -OAc group is reactive towards subsequent $Ti(O^iPr)_4$ and induces subsequent ligand exchange and thus, the higher binding energy carbon peak disappeared (Figure 1.4c). With this ligand exchange, TiO_2 is formed on Si surface. In contrast to Si and SiO_2, the SiCOH surface is predominantly terminated with alkyl groups. These alkyl groups are less reactive to precursors compared to the -H termination on Si and -OH termination on SiO_2. On SiCOH, the precursors can only react on sparse defect -OH sites and thus nucleate slowly. However, since SiCOH is SiO_2 passivated with Si-OC_xH_y or Si-C_xH_y group[24-26], the exact density of -OH defect sites among major Si-OC_xH_y or Si-C_xH_y groups on SiCOH cannot be quantified with a standard XPS spectrometer such as the one employed in the present study. This nucleation on defects eventually induces the loss of selectivity as dosing continues.

1.4.2 TiO_2 ALD with $Ti(O^iPr)_4$ and HCO_2H

From the above experiment, it was found that TiO_2 ALD can occur with $Ti(O^iPr)_4$ and AcOH through the ligand exchange. Based on this finding, it was hypothesized that other carboxylic acids may also have similar reaction with $Ti(O^iPr)_4$. Formic acid (HCO_2H) has a pKa of 3.7 while acetic acid has a pKa of 4.7. This stronger acidity means formic acid can be 10x stronger proton donor than acetic acid. As formic acid may have 10x higher reactivity in ALD reactions[26], it can induce a larger portion of the subsequently dosed $Ti(O^iPr)_4$ to react with the surface formate bonds than the acetate bonds from AcOH. The ALD reaction with $Ti(O^iPr)_4$ and formic acid was tested to verify whether it shows faster growth and greater selectivity.

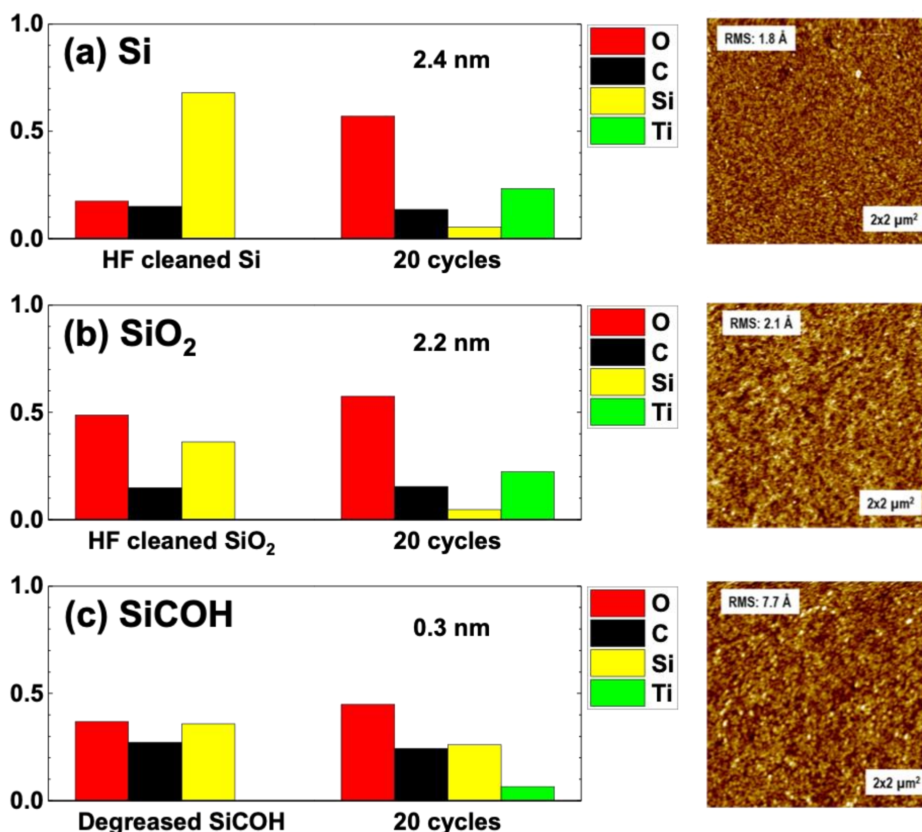

Figure 1.7 XPS chemical composition (Left) and AFM image (Right) of TiO_2 film after 20 ALD cycles of Ti(O^{i}Pr)$_4$ and HCO_2H at 250 °C. (a) HF cleaned Si: 2.4nm of TiO_2 was deposited and the film was smooth with a RMS roughness of 1.8 Å. (b) HF cleaned SiO_2: 2.2 nm of TiO_2 was deposited and the film was smooth with a RMS roughness of 2.1 Å. (c) Degreased SiCOH: Around 0.3 nm of TiO_2 was deposited and the surface RMS roughness was 7.7 Å, which is similar to that of bare SiCOH surface.

Figure 1.7 shows the XPS chemical composition and AFM images of each substrate after 20 ALD cycles of Ti(O^{i}Pr)$_4$ and HCO_2H. After 20 ALD cycles, 2.4 nm and 2.2 nm of TiO_2 were deposited on Si and SiO_2, respectively. Conversely, only ~0.3 nm, TiO_2 was detected on SiCOH. As expected, the HCO_2H was more reactive than AcOH; 20 ALD cycles with HCO_2H had similar thickness of TiO_2 deposition to 240 ALD cycles with AcOH

indicating that HCO_2H has around 10x higher reactivity than AcOH. However, even though different carboxylic acids were used, both experiments showed similar selectivity of around 2-3 nm of TiO_2 deposition on Si and SiO_2 and around a monolayer deposition (~0.4 nm)[29] on SiCOH (sub 1 nm deposition on SiCOH can be TiO_2 nuclei; however, even for the films, the XPS attenuation equation was employed to determine a nominal film thickness.). This observation shows that the carboxylic acid second precursors have only a minor effect on selectivity. Therefore, the loss of selectivity of TiO_2 ALD could be mainly due to the reaction of $Ti(O^iPr)_4$ with the SiCOH surface; As a metal alkoxide precursor, $Ti(O^iPr)_4$ contains oxygen atoms and can therefore react with defect sites to nucleate on SiCOH. This ultimately causes a loss of selectivity.

Figure 1.7 shows the AFM images of the TiO_2 films on Si, SiO_2 and SiCOH. The RMS roughness of the TiO_2 film on Si and SiO_2 were 1.8 Å and 2.1 Å, respectively. The RMS roughness on SiCOH was 7.7 Å similar to that of a degreased SiCOH surface. These results show that TiO_2 ALD using HCO_2H has 10x greater growth rate but produces films with similar selectivity and roughness compared to ALD with AcOH.

1.4.3 TiO_2 single precursor thermal CVD with $Ti(O^iPr)_4$

It was previously reported that $Ti(O^iPr)_4$ thermally decomposes and undergoes unimolecular CVD at 250 °C.[1] Therefore, single precursor pulsed CVD with $Ti(O^iPr)_4$ was performed to determine the inherent selectivity.

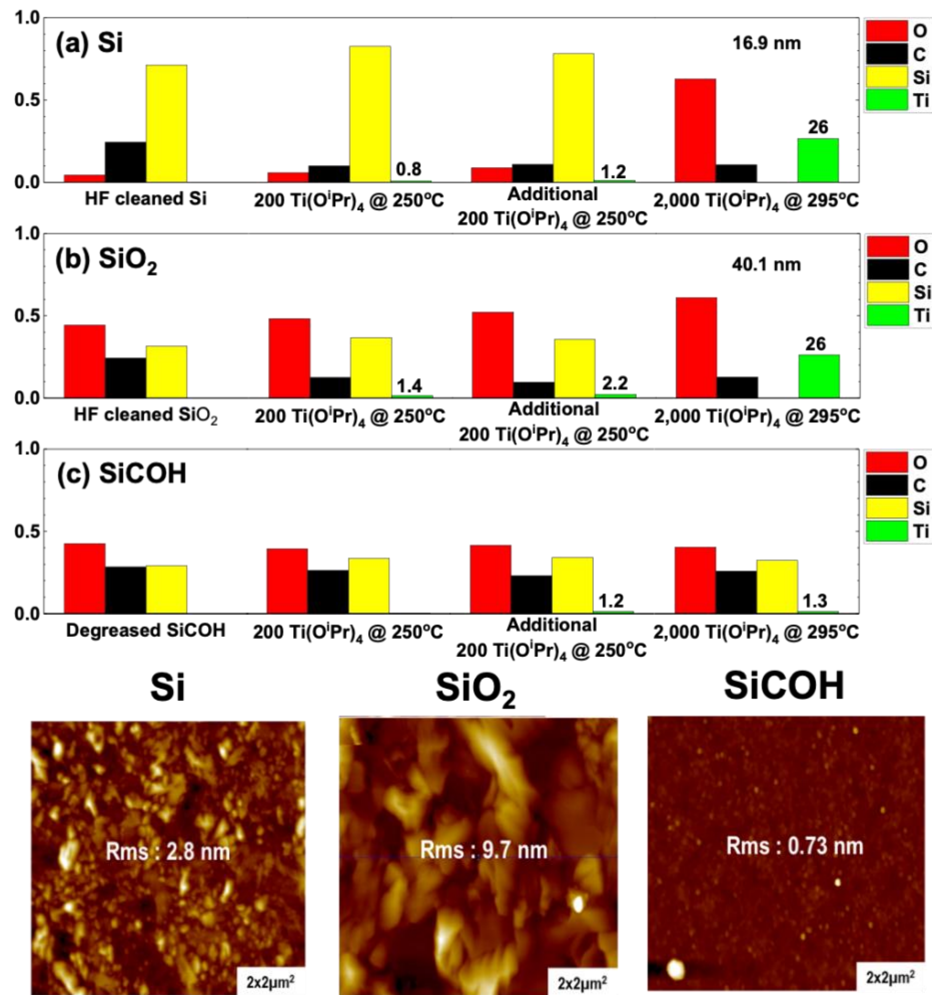

Figure 1.8 XPS chemical composition (Above) and AFM (Below) of (a) HF cleaned Si, (b) HF cleaned SiO_2 and (c) degreased SiCOH after doses of $Ti(O^iPr)_4$ at 250 °C and 295 °C. After 400 pulses of $Ti(O^iPr)_4$ at 250 °C, there is only a small amount of Ti on all three samples. After 2,000 pulses of $Ti(O^iPr)_4$ at 295 °C, there is 16.9 nm TiO_2 deposited on Si and 40.1 nm TiO_2 on SiO_2 while there is only 1.3% Ti on SiCOH. AFM images show that the TiO_2 films on Si, SiO_2 and SiCOH have RMS roughness of 2.8, 9.7 and 0.7 nm, respectively.

Figure 1.8 shows XPS chemical composition of TiO_2 films on Si, SiO_2 and SiCOH deposited by the pulsed CVD process. At first, CVD was tested at 250 °C: after 400 pulses of $Ti(O^iPr)_4$, Ti compositions of 1.2%, 2.2%, and 1.2% were observed on Si, SiO_2, and

SiCOH, respectively. This indicates that only TiO_2 nuclei were formed on each substrate. Compared to the 2-3 nm of TiO_2 deposited on Si and SiO_2 during ALD with HCO_2H with the same number of $Ti(O^iPr)_4$ pulses, the growth rate by unimolecular CVD at 250 °C was minuscule. This indicates that the precursor does not undergo significant thermal decomposition on a 250 ˚C substrate.

Since CVD at 250 °C left an almost clean SiCOH surface, an additional inherent selectivity test with higher temperature CVD was made on the same SiCOH sample. The sample temperature was increased to 295 °C to promote thermal decomposition in the pulsed CVD reaction. After 2,000 pulses of $Ti(O^iPr)_4$, Si peaks (Si 2p) were fully attenuated on Si and SiO_2 substrates, which means that more than ~4 nm (without knowing the exact film thickness on Si and SiO_2 from XPS result) of TiO_2 was deposited on both substrates. From ellipsometry, the precise thicknesses of TiO_2 on Si and SiO_2 were 16.9 nm and 40.1 nm, respectively. Compared to previous ALD results, which showed films of equivalent thicknesses, significantly more TiO_2 deposition occurred on SiO_2 than on Si, which showed potential in selective TiO_2 deposition on SiO_2 in preference to Si. This shorter induction period on SiO_2 is attributed to the higher reactivity of the hydroxyl terminated surface on SiO_2 than the hydrogen terminated surface on Si. For the pulsed unimolecular thermal CVD process, after 2,000 $Ti(O^iPr)_4$ pulses at 295 °C, a composition of only 1.3% of Ti was detected on SiCOH (most of this was deposited during the prior 250 °C CVD test), showing that CVD reaction at 295 °C has high selectivity.

These ALD and CVD experiments at two different sample temperatures show that temperature can affect the selectivity. From ALD with two different carboxylic acids, it was proven that the carboxylic acids have minor effect on selectivity. The loss of selectivity could

be due to the nucleation of $Ti(O^iPr)_4$ on SiCOH surface. Therefore, the higher selectivity at 295 °C unimolecular CVD may be due to the higher sample temperature promoting the desorption of $Ti(O^iPr)_4$ on SiCOH surface before it nucleates.

Ex situ AFM was performed to check the film morphology. Figure 1.8 shows the atomic force micrograph of each sample. Si and SiO_2, which had thick TiO_2 deposition of 16.9 nm and 40.1 nm, respectively, showed 2.8 nm and 9.7 nm RMS roughness, respectively. Sparse TiO_2 nuclei are observed on SiCOH and the RMS roughness was 0.73 nm, which was close to that of a degreased SiCOH. The increase in RMS roughness on Si and SiO_2 surface is due to the crystallization of the TiO_2 film. Figure 1.9 shows the GIXRD results for the films on Si and SiO_2 from Figure 1.8. The 16.9 nm-thick TiO_2 film on Si showed a small anatase (100) peak (inset of Figure 1.9a). The crystallization became more significant for the TiO_2 film on SiO_2 (40.1 nm) since it was a thicker film than the film on Si (Figure 1.9b).[31] GIXRD for SiO_2 showed anatase (100), (200), and (204) peaks. In addition, the intensity for (100) peak from SiO_2 substrate was higher than that from Si substrate because the film on SiO_2 was thicker. The peaks observed at 51° and 55° are from Si (113) peak and the XRD sample stage, respectively. In addition, 2 nm TiO_2 film from the same CVD process showed a smooth film with 0.4 nm RMS roughness (Figure 1.10). These results show that the thicker TiO_2 film was more crystalline, which is consistent with the increased roughness observed by AFM (Figure 1.8). This effect is well-known in the literature; the crystallization temperature of an oxide film decreases as the film thickness increases.[31] This crystallization issue can be problematic for potential application of selective TiO_2 deposition in nanoscale patterning and could be avoided by periodically inserting a second oxide layer into the film to form a nanolaminate structure.[27, 28]

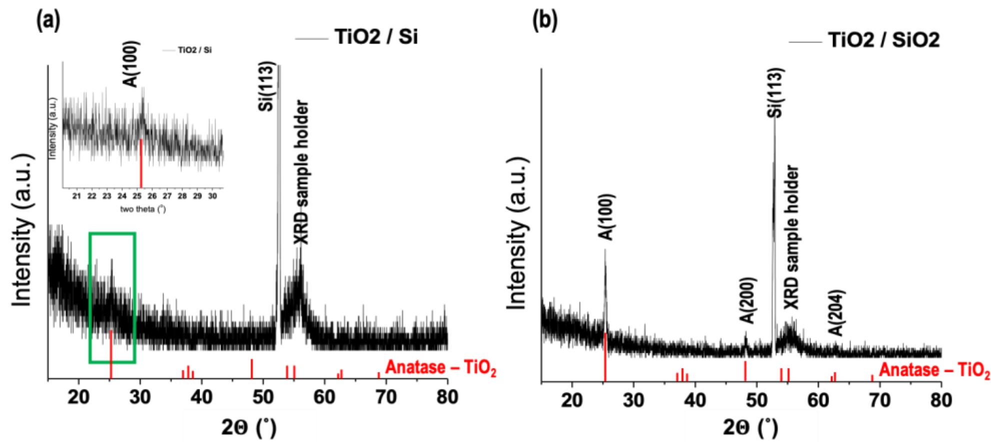

Figure 1.9 GIXRD curves for (a) Si and (b) SiO_2 after TiO_2 CVD at 295 °C (samples from Figure 1.8). (a) 16.9 nm TiO_2 on Si showed small TiO_2 anatase (100) peak as shown in inset of (a). (b) 40.1 nm TiO_2 on SiO_2 showed TiO_2 anatase (100), (200) and (204) peaks. The peaks observed at 51° and 55° from both samples are from Si (113) peak from the substrates and the XRD sample holder, respectively.

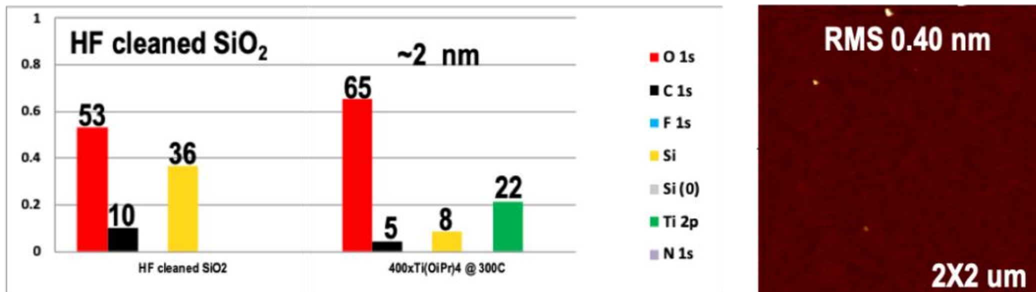

Figure 1.10 XPS chemical composition (Left) and AFM (Right) on SiO_2 after 400 $Ti(O^iPr)_4$ pulses at 300 °C. Unlike the 40 nm TiO_2 film on SiO_2 (Figure 1.8), this thin TiO_2 film showed a smooth film, proving the high roughness is due to the crystallization as the film thickness increases.

1.4.4 Nano-scale selectivity of TiO_2 CVD

Selectivity tests for TiO_2 ALD and pulsed unimolecular CVD process showed that the pulsed unimolecular CVD process with $Ti(O^iPr)_4$ at 295 °C had the highest selectivity. Therefore, TiO_2 CVD at 295 °C was tested on Cu/SiCOH nanoscale patterned samples to determine the selectivity of deposition on the nanometer scale. Nano-scale selective deposition for the ALD process was not tested, as ALD had low selective deposition (~2 nm), which is difficult to detect with TEM. As mentioned in the experimental section, since the SiCOH region of the patterned sample was damaged and likely contained significantly more defect sites than a blanket SiCOH wafer surface, additional passivation (proprietary passivation process from Applied Materials) was performed before loading the sample into the deposition chamber. The Cu region of the patterned sample also went through the passivation process; however, the passivant on the Cu surface desorbed during a subsequent UHV anneal (350 °C for 30 min, as determined by XPS of the carbon from Figure 1.11) before the CVD process. In this way, only the SiCOH region of the patterned sample was selectively passivated against TiO_2 deposition. When loading the above patterned sample, a blanket SiCOH sample with the same passivation was also loaded to serve as a reference.

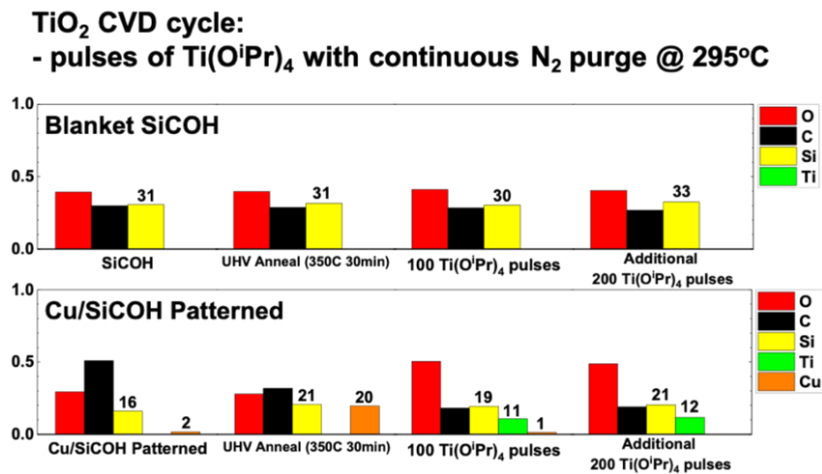

Figure 1.11 XPS chemical composition of passivated SiCOH and passivated Cu/SiCOH nanoscale patterned sample before and after 300 pulses of Ti(O^{i}Pr)$_4$ at 295 °C. After 300 pulses of Ti(O^{i}Pr)$_4$ in total, the blanket SiCOH still remained clean without any Ti peak. For the Cu/SiCOH patterned sample, after 300 Ti(O^{i}Pr)$_4$ pulses, the Cu 2p peak is attenuated and 12% of Ti 2p was observed. This is consistent with a TiO_2 film covering the Cu surface. Si (Si 2p) peak maintained similar atomic composition consistent with no TiO_2 deposition on the SiCOH region of the patterned sample, similar to the lack of deposition on the blanket SiCOH sample.

Figure 1.11 shows the XPS chemical composition of a passivated SiCOH and a passivated Cu/SiCOH patterned sample before and after doses of Ti(O^{i}Pr)$_4$ at 295 °C. After 300 pulses of Ti(O^{i}Pr)$_4$, the blanket SiCOH substrate still remained deposition-free, with no Ti peaks observed by XPS. For the Cu/SiCOH patterned sample, after 300 Ti(O^{i}Pr)$_4$ pulses, the Cu 2p peak disappeared and a Ti 2p peak corresponding to 12 at% Ti appeared. This means that a TiO_2 film was deposited on the exposed Cu surface of the patterned substrate. The Si peak maintained similar XPS abundance before and after deposition on the patterned sample, suggesting that there was no TiO_2 deposition on the SiCOH region of the patterned sample, as also observed on the blanket SiCOH substrate.

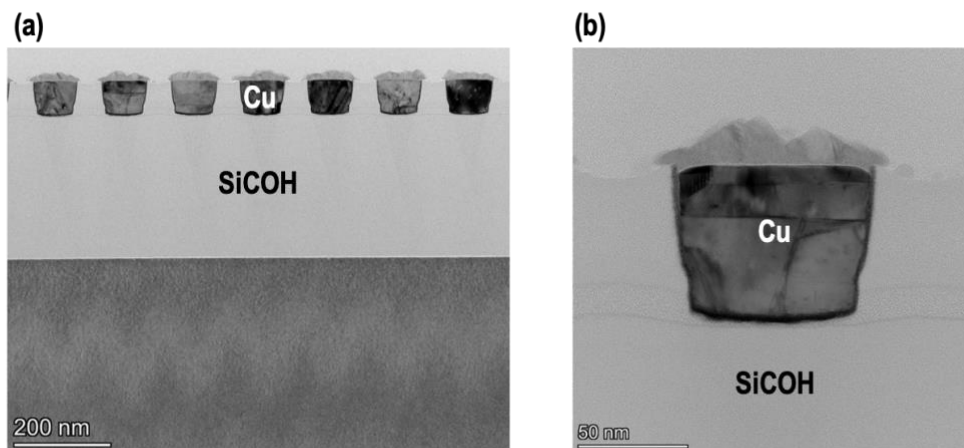

Figure 1.12 TEM of Selective TiO_2 deposition on a Cu/SiCOH patterned sample (a) TEM image after TiO_2 unimolecular CVD with $Ti(O^iPr)_4$ at 295 °C (300 pulses total) on a Cu/SiCOH patterned sample and (b) The magnified view of a Cu inlay. As can be seen from TEM images, TiO_2 was selectively deposited on the Cu surface only. The film thickness was around 20 nm and the film roughened, likely due to crystallization as in previous experiments.

The selectivity of the process was documented using cross-sectional transmission electron microscopy, as shown in Figure 1.12. The width of Cu and SiCOH regions on the sample surface were ~90 nm and ~50 nm, respectively. The low-magnification micrograph (Figure 1.12a) shows that the TiO_2 was only deposited on the Cu regions of the patterned sample. No significant TiO_2 deposition was observed on any SiCOH surface. The magnified view of the patterned inlay (Figure 1.12b) shows around 20 nm of TiO_2 deposited on the Cu with slight protrusion onto the neighboring SiCOH due to lateral growth of the TiO_2 material. This lateral growth of TiO_2 could be due to physisorbed $Ti(O^iPr)_4$ precursor on SiCOH surface, which diffused and reacted on the sidewall of TiO_2 film on Cu, however, further study is required. It is again seen from TEM image on Figure 1.12 that the TiO_2 film on Cu showed very rough surface which is likely due to the crystallization, but as previously noted using nanolaminates can produce smooth films.[27,28] Therefore, based on TEM study of TiO_2

unimolecular CVD at 295 °C, it is proven that the process can selectively deposit TiO_2 film in nanoscale regions.

1.5 Conclusions

Inherent selective TiO_2 deposition on Si and SiO_2 in preference to SiCOH (a porous low-k dielectric) with ALD and CVD was investigated. Water-free deposition was tested to both protect the SiCOH and to enhance selectivity. At 250 °C sample temperature, selective water-free ALD of TiO_2 using $Ti(O^iPr)_4$ and AcOH was accomplished. This ALD process achieved around 1.5 nm of selective TiO_2 deposition on Si and SiO_2 while less than a monolayer (3% Ti from XPS measurement) was deposited on SiCOH. AFM showed that the TiO_2 films on Si and SiO_2 were smooth with 2 Å and 3 Å RMS roughness, respectively. An XPS study showed that TiO_2 was deposited through ligand exchange reaction between isopropoxide ligand ($-O^iPr$) of $Ti(O^iPr)_4$ and acetate ligand (-OAc) of AcOH. For ALD with $Ti(O^iPr)_4$ and HCO_2H at 250 °C sample temperature, the growth rate increased by a factor of ~10x compared to ALD with AcOH while maintaining similar selectivity. This is consistent with chemical intuition that HCO_2H acts as a stronger proton donor than AcOH. The TiO_2 films deposited by ALD using HCO_2H were smooth with RMS roughness of around 2 Å on Si and SiO_2. The selectivity of both ALD showed that the loss of selectivity is mainly due to nucleation of $Ti(O^iPr)_4$ on SiCOH surface and not related to carboxylic acid co-reactors such as AcOH and HCO_2H. Single precursor CVD by thermal decomposition of $Ti(O^iPr)_4$ was studied; at 295 °C, highly selective deposition of TiO_2 was achieved with 16.9 nm on Si, 40.1 nm on SiO_2. However, these thick TiO_2 films were prone to crystallization and had RMS roughness of more than one nanometer. The nanolaminate structure can solve

this crystallization issue[27,28] thus, further study on inherent selective nanolaminate oxide deposition is required. In addition, TiO_2 film from both ALD and CVD showed 10-20 % surface carbon; if there is high carbon in the entire depth of the film, the carbon may degrade its electrical performance. As observed by TEM, single precursor CVD at 295 °C on patterned substrates exhibits selective deposition on Cu with minimal deposition on SiCOH, which demonstrates the utility of the unimolecular CVD process in nanoscale patterning applications. Further optimization with a nanolaminate CVD process will form a high selective smooth film and further enable its applications in the patterning process for nm scale MOSFET fabrication.

Chapter 1, in full, is a reprint of the material as it appears in ACS Applied Nano Materials. Y. Cho, C. F. Ahles, J. Y. Choi, J. Huang, A. Jan, K. Wong, S. D. Nemani, E. Yieh, and A.C. Kummel, “Inherently Selective Water-Free Deposition of Titanium Dioxide on the Nanoscale: Implications for Nanoscale Patterning”, *ACS Appl. Nano Mater.5, 1, 476-485 (2022).* The dissertation author was the primary investigator and author of this paper.

Chapter 2

Inherent Selective Pulsed Chemical Vapor Deposition of Amorphous Hafnium Oxide / Titanium Oxide Nanolaminates

2.1 Abstract

Water-free Inherent selective pulsed chemical vapor deposition (CVD) of HfO_2/TiO_2 nanolaminates on Si and SiO_2 in preference to SiCOH has been studied. SiCOH is highly porous alkylated SiO_2, which is used as a nonreactive low-k dielectric. $Ti(O^iPr)_4$ [titanium(IV) isopropoxide] and $Hf(O^tBu)_4$ [Hafnium tert butoxide] were used in the CVD study. Previous studies showed that metal alkoxide precursors could form oxide films through thermal decomposition. However, single oxide films greater than 2 nm can be rough due to crystallization. To solve this issue, HfO_2/TiO_2 nanolaminate structures were studied. With sequential dosing of each precursor in a supercycle at 300°C sample temperature, HfO_2/TiO_2 nanolaminate films with thin (< 3 nm) sublayers were selectively deposited. The films were smooth with root mean square (RMS) roughness lower than 0.5 nm and almost amorphous from XRD analysis; this is unexpected since both oxides readily crystalize. Amorphous nanolaminate oxide film deposition with high selectivity was achieved by controlling each sublayer thickness and the Hf:Ti ratio. TEM studies proved that ~20 nm of the nanolaminate film could also be selectively deposited on nanoscale patterned surfaces. This selective amorphous nanolaminate oxide CVD process has a potential to be applicable in the nanoscale patterning in MOSFET fabrication.

2.2 Introduction

Atomic layer deposition (ALD) and chemical vapor deposition (CVD) are commonly used in the semiconductor industry.[3] Among various methods, thermal deposition (as opposed to plasma-enhanced deposition) is one of the primary methods for ALD and CVD on three dimensional topologies. Within a specific sample temperature range, also known as the 'ALD window', a self-limiting chemical reaction between the ligands of each precursor occurs, which deposits approximately one atomic level layer on the surface. As the sample temperature increases above the 'ALD window', often self-limiting ALD reactions no longer dominate the deposition, but thermal CVD prevails. At the CVD temperature, the ligands of metal precursor decompose and desorb or form reactive ligands such as hydroxyl (-OH), which promote fast film growth.[32] Due to its self-limiting nature, ALD forms smooth and conformal films. However, with careful control of dosing conditions, CVD can also produce smooth and conformal films.[2]

Nanoscale patterning is a crucial issue in fabricating leading-edge commercial semiconductor devices. The need for novel patterning is acute in backend metallization when metals and dielectric layers with high aspect ratios in nanometer-scale are employed. Area selective oxide deposition in conjunction with the double patterning technique is possible for nanoscale patterning.[5,32] For selective oxide deposition in backend fabrication, water-free deposition is favorable since it can not only induce higher selectivity[1] but also prevent damage of metals and low k dielectric, e.g., SiCOH. There are three methods of selective deposition: inherent selective deposition, selective passivation, and selective activation. The inherent selective deposition is based on reactivity differences of different surfaces during precursor mediated chemisorption. The binding energy difference between precursor and

different surface bonds can induce selective deposition on a specific surface.[7-9,32,33] The inherent selective deposition is advantageous since it does not require additional steps to add or remove passivants. However, the majority of selective depositions are based on selective passivation. Specific molecules, such as a long-chain alkane, can inhibit the nucleation of precursors. Therefore, by selectively reacting the passivant on a particular surface, selective deposition on surfaces without the passivant occurs with consequent selective ALD/CVD.[11-15] In addition, selective activation, such as electron beam-induced ALD (EEALD), can also induce selective deposition on the pretreated surface.[16-19]

In many cases, thick oxide deposition is desired, including the nanoscale patterning application. However, previous studies showed that many oxide films, including TiO_2[32], HfO_2[31], crystallize with increasing film thickness. The crystallization is not preferable if a smooth film is required. Making a nanolaminate structure with two or more oxides can solve this issue.[27,28,34-38] There have been many studies that the nanolaminate structure of different oxide films inhibits crystallization. Al_2O_3 is known to be amorphous regardless of its thickness; therefore, many nanolaminate structures using Al_2O_3 have been studied.[34-37] G. E. Testoni et al. proved that TiO_2 film can stay amorphous by making a nanolaminate structure adding Al_2O_3 monolayers.[34] Testoni et al. showed that even a monolayer of Al_2O_3 between two TiO_2 sublayers could inhibit crystallization. However, it was also shown that crystallization could not be inhibited if each TiO_2 sublayer is more than ~3 nm in thickness. The research on the nanolaminate structure using two different oxides that are both prone to crystallization has also been studied.[27,28,38] D. H. Triyoso et al. proved that the nanolaminate structures of HfO_2/TiO_2 can form amorphous films.[27] With an ALD using titanium tetrachloride ($TiCl_4$), hafnium tetrachloride ($HfCl_4$), and water, nanolaminate structures with

various Hf:Ti ratios were tested. All films were amorphous and showed lower RMS roughness than pure HfO_2 and TiO_2 films. The drawback of this process is that halogens, e.g., Cl and F, can corrode metals while the H_2O will degrade SiCOH, so the process is incompatible with the middle or back of the line processing. Moreover, most of the research about the oxide nanolaminate structure studied the film's mechanical, electrical, and optical characteristics but not about their selective deposition.

The authors previously reported pulsed chemical vapor deposition (CVD) of TiO_2 at around 300°C with inherent selectivity for deposition on Si or SiO_2, but not on SiCOH, a non-reactive low k dielectric material; ~17 nm and ~40 nm of TiO_2 were selectively deposited on Si and SiO_2, respectively, while less than 0.1nm was deposited on SiCOH.[32] However, the thick TiO_2 film formed nano-crystallites which induced rough surface formation. This roughness needs to be reduced for application to nanoscale patterning. The authors also recently reported selective pulsed CVD of TiO_2/Al_2O_3 and HfO_2/Al_2O_3 nanolaminates by sequential pulses of titanium isopropoxide ($Ti(O^iPr)_4$) / trimethylaluminum (TMA) and hafnium tertbutoxide ($Hf(O^tBu)_4$) / TMA, respectively.[39] Around 20 nm of a nanolaminate film with an RMS roughness lower than 0.5 nm was selectively deposited on Si and SiO_2, in preference to SiCOH. However, as TMA does not contain oxygen, too much TMA dosing (Al richer nanolaminate) could inhibit the film growth.

In the present study, sequential pulsed CVD at 300°C sample temperature using $Ti(O^iPr)_4$ and $Hf(O^tBu)_4$ to form HfO_2/TiO_2 nanolaminate films was studied. $Hf(O^tBu)_4$ and $Ti(O^iPr)_4$ are metal alkoxide precursors which contain four oxygen atoms per metals atom inside their ligands so that these precursors can solely be used to deposit oxide film by thermal decomposition at 300°C. This is a unique approach for nanolaminate formation since

two oxygen-containing metal precursors were employed; for nanolaminate oxide formation, usually, only one oxygen-containing precursor (ex: H_2O) is employed with two different metal precursors (ex: $TiCl_4$, $HfCl_4$). Success with dual oxygen-containing metal precursors enables a large variety of halogen-free precursors to be employed.

Inherent selectivity of the process was tested on hydrogen-terminated silicon, hydroxyl-terminated SiO_2, and SiCOH. SiCOH was alkyl ($-C_xH_y$) terminated SiO_2 and was used as a non-reactive surface.[23-26] After confirming the selectivity and crystallization in single oxide films, both the amorphousness and selectivity of HfO_2/TiO_2 nanolaminates film were documented. The test was done with three different Hf:Ti ratio nanolaminate films to verify the effect of the selectivity of each single oxide on that of the nanolaminate film. In addition, X-ray diffraction (XRD) was employed to determine the roles of the HfO_2/TiO_2 nanolaminate structure and sublayer thickness influence on crystallization. Finally, HfO_2/TiO_2 nanolaminate selective pulsed CVD was tested on Cu/SiCOH nanoscale patterned sample to evaluate the potential for nanoscale patterning applications. While the selectivity of the HfO_2/TiO_2 nanolaminate pulsed CVD deposition is similar to TiO_2/Al_2O_3 nanolaminate pulsed CVD also reported by the authors[39], HfO_2/TiO_2 are expected to be easier to etch than TiO_2/Al_2O_3 nanolaminates and therefore advantageous.[40-43] In addition, by employing chemically similar precursors for the Ti and Hf, it is possible to determine how the selectivity of each precursor contributes to the overall selectivity of the nanolaminate deposition.

2.3 Experimental

In this study, the selective pulsed CVD process for HfO_2/TiO_2 nanolaminate film was tested on three different substrates: Si, SiO_2, and SiCOH. Each substrate was diced into ~2 x ~12 mm rectangles so that three samples could be loaded on one sample holder. Samples were wet-cleaned before loading into the UHV chamber. The three samples were sequentially degreased with acetone, methanol, and deionized water for 15 seconds. To remove the surface native oxide, degreased Si and SiO_2 samples were immersed in a 0.5% diluted hydrofluoric acid solution for 30 seconds. After the wet cleaning, three samples were blown with an N_2 air gun to remove residual solution on the substrate surface. The samples were loaded to the UHV chamber on a single sample holder to go through the same dosing process to check the inherent selectivity. In addition to the selectivity test, HfO_2/TiO_2 nanolaminate pulsed CVD process was performed on a Cu/SiCOH nanoscale patterned sample. Cu/SiCOH patterned sample was wet-cleaned with degreasing process explained above. Since the SiCOH region of the patterned sample was damaged from the initial fabrication process and, therefore, not fully covered with $-OC_xH_y$ or $-C_xH_y$ bonds, an additional passivation process was done with a proprietary passivation process from Applied Materials. After the passivation, the Cu/SiCOH patterned sample was loaded to the UHV chamber, together with a blanket SiCOH sample to check selective deposition on the Cu region only.

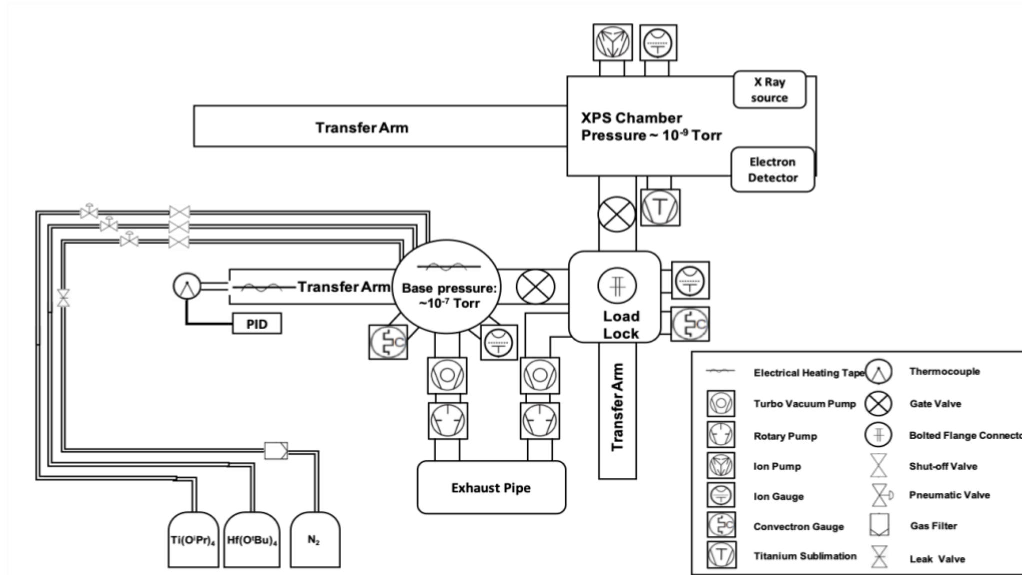

Figure 2.1 A schematic of UHV chamber for HfO_2/TiO_2 nanolaminate CVD and XPS analysis. The system consists of three chambers: load lock chamber for sample loading, deposition chamber for CVD process, and UHV XPS chamber for XPS analysis.

Figure 2.1 shows a chamber schematic. A load lock chamber was employed to load and retrieve samples. The load lock chamber was pumped by a turbopump (Pfeiffer TPU 060) and a mechanical backing pump (Edwards RV3). The deposition chamber is also pumped by a turbopump (Pfeiffer TPU 060) and a mechanical backing pump (Edwards RV3). The base pressure of the deposition chamber was about 10^{-7} Torr. The deposition chamber contained a manipulator with a Cu sample mounting holder. A cartridge heater, inserted inside the Cu platform, heated the samples. Dosing lines for the precursors and nitrogen purge gas were connected to the deposition chamber. The precursor pulse pressure was controlled through a pneumatic valve, and no push gas was used. The deposition chamber wall and dosing lines were kept at 150°C. The connected chamber was employed for *in-vacuo* X-ray photoelectron spectroscopy (XPS). The chamber was maintained at UHV pressure (low 10^{-9}

Torr) and pumped by an ion pump (Agilent Varian VacIon 300 StarCell). An *in-vacuo* transfer was performed between deposition and XPS analysis so that the samples were not exposed to the ambient air prior to XPS, which could cause unwanted contamination or oxidation.

N_2 gas was continuously purged during the pulsed CVD process to remove the residual precursors inside the dosing chamber. Precursor dosing was monitored by the pressure spikes inside the deposition chamber and controlled by the precursor bottle temperature and the pneumatic valve open time. The $Ti(O^iPr)_4$ bottle was kept at room temperature (~21°C), and the $Hf(O^tBu)_4$ bottle was heated up to 40°C. The dosing time for each precursor was set to 50 ms and 200 ms for $Ti(O^iPr)_4$ and $Hf(O^tBu)_4$, respectively.

To check the crystallization from single oxide deposition and the selectivity of pulsed CVD for single oxide film deposition, single precursor pulsed CVD of TiO_2 and HfO_2 with $Ti(O^iPr)_4$ and $Hf(O^tBu)_4$, respectively, were studied. For TiO_2 pulsed CVD, multiple pulses of $Ti(O^iPr)_4$ were dosed between 250 °C and 300 °C sample temperature. Multiple pulses were employed instead of long single pulses due to the turbomolecular pumping of the ALD chamber. Between each $Ti(O^iPr)_4$ pulse, 5 seconds of purging time was employed to remove residual and physisorbed precursor. For HfO_2 pulsed CVD, multiple pulses of $Hf(O^tBu)_4$ were dosed at 300 °C with 60 seconds interval between pulses. For HfO_2/TiO_2 nanolaminate CVD, the sample temperature was kept at 300°C. Multiple pulses of $Ti(O^iPr)_4$ and $Hf(O^tBu)_4$ were dosed in each cycle. The purge time between $Ti(O^iPr)_4$ pulses and $Hf(O^tBu)_4$ pulses was 5 and 60 seconds, respectively. The number of pulses per cycle was controlled between 20 and 100 pulses for $Ti(O^iPr)_4$ and 1 and 5 for $Hf(O^tBu)_4$ to tune the Hf:Ti ratio of the nanolaminate film. The $Hf(O^tBu)_4$ is more reactive than the $Ti(O^iPr)_4$ precursor; therefore,

less $Hf(O^tBu)_4$ pulse was dosed per cycle. The purge time between $Ti(O^iPr)_4$ and $Hf(O^tBu)_4$ was 60 seconds to remove all the residue from previous pulses.

After the pulsed CVD process, the samples were transferred to the XPS chamber, and *in-vacuo* XPS analysis was performed. A monochromatic Al Kα source (1486.7 eV) and a hemispherical analyzer (XM 1000 MkII/SPHERA, Omicron Nanotechnology) were employed. The anode voltage and the filament emission current were set to 10 kV and 25 mA, respectively, with hemisphere analyzer pass energy of 50 eV. The XPS detector was aligned to 60° from the sample surface normal. The peak shape analysis was performed with CASA XPS v.2.3 program and utilized Shirley background subtraction. The chemical compositions were normalized to the sum of all elements. After the whole in-situ CVD and XPS process, the morphology of the film was analyzed with ex-situ atomic force microscopy (AFM) (Agilent 5500) in tapping mode. For film thickness measurement, the oxide film thickness was derived based on Si substrate XPS signal attenuation when Si substrate signal was still detectable (film thickness less than 6 nm).[6,32] When Si signal was not detected (film thickness more than 6 nm), the film thickness was later measured by ex-situ ellipsometry (J. A. Woollam M-2000D). For crystallization study and nanoscale selectivity test, grazing incidence X-ray diffraction (GIXRD) (Rigaku SmartLab, Cu anode operating at 2kW, parallel beam configuration, fixed 1.005° incidence angle) and transmission electron microscopy (TEM) were performed.

2.4 Results and Discussion

2.4.1 Selectivity and crystallization study on single oxide film

To check both the selectivity and the crystallization in single oxide films, single oxide pulsed CVD was tested. Since metal alkoxide precursors [$Ti(O^iPr)_4$ and $Hf(O^tBu)_4$] contain oxygen in their ligands, $Ti(O^iPr)_4$ and $Hf(O^tBu)_4$ can form oxide film by unimolecular thermal decomposition.[6,32]

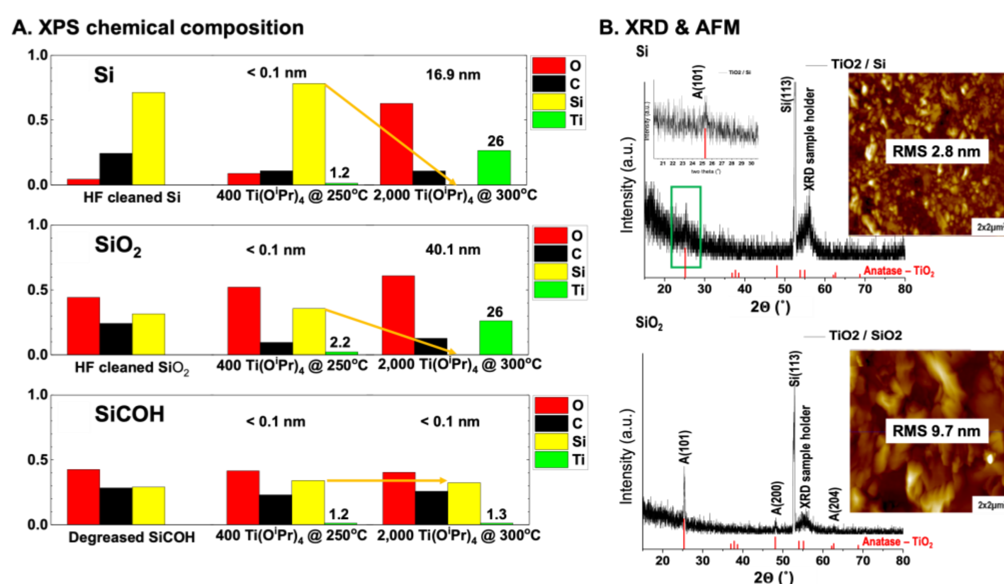

Figure 2.2 Analysis of Pulsed CVD TiO_2 Films at 300°C. (A) XPS chemical composition of HF cleaned Si, HF cleaned SiO_2 and degreased SiCOH after doses of $Ti(O^iPr)_4$ at 250 °C (negligible amount of nucleation) and 300 °C, and (B) XRD and AFM images of TiO_2 film on Si and SiO_2.

Figure 2.2 shows the XPS chemical composition on Si, SiO_2, and SiCOH during the TiO_2 pulsed CVD process, which the authors previously reported.[32] At 250°C, 400 pulses of $Ti(O^iPr)_4$ barely decomposed and induced only a negligible CVD reaction (less than one monolayer) on any substrates. As the sample temperature increased to 300 °C, $Ti(O^iPr)_4$ induced a pulsed CVD reaction through thermal decomposition. After 2,000 pulses at 300

°C, Si peaks (Si 2p) were fully attenuated from Si and SiO_2. The thickness of TiO_2 on Si and SiO_2 were 16.9 nm and 40.1 nm, respectively. On SiCOH, however, 1.3% of Ti was detected, which corresponds to less than a monolayer of TiO_2. This selective deposition was due to the inherent reactivity difference for precursor mediated chemisorption of $Ti(O^iPr)_4$ on each surface.

Ex-situ AFM was performed to check the film morphology. As shown in Figure 2.2, the thick TiO_2 films on Si and SiO_2 had 2.8 nm and 9.7 nm RMS roughness. GIXRD analysis proved that the rough TiO_2 films on Si and SiO_2 were due to crystallization. The 16.9 nm TiO_2 film on Si exhibited a small anatase (101) peak. For the 40.1 nm TiO_2 film on SiO_2, crystallization became more significant. GIXRD for the 40.1 nm TiO_2 film on SiO_2 showed anatase (101), (200), and (204) peaks, and the intensity of the (101) peak was higher than the intensity of the peak from Si substrate. These results are consistent with crystallization increasing with TiO_2 film thickness. This crystallization issue, which caused nm scale film roughness, can be a problem for its application to nanoscale patterning.

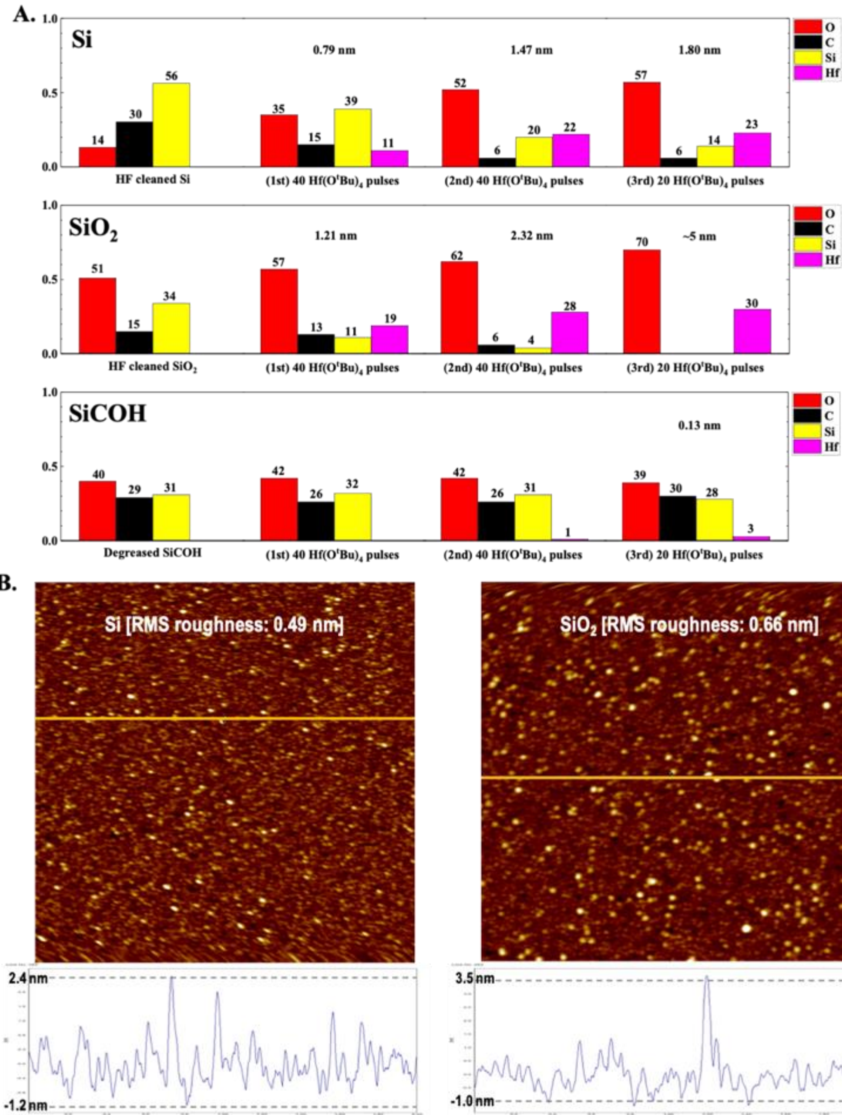

Figure 2.3 Analysis of HfO_2 Pulsed CVD with $Hf(O^tBu)_4$ at 300 °C (A) XPS chemical composition of HF cleaned Si, HF cleaned SiO_2, and degreased SiCOH after the HfO_2 CVD process and (B) AFM images and line traces of HfO_2 film on Si and SiO_2.

HfO_2 CVD with $Hf(O^tBu)_4$ was tested at 300 °C. The XPS chemical composition and the AFM images for HfO_2 films on the substrates are shown in Figure 2.3. After 100 $Hf(O^tBu)_4$ pulses, 1.8 nm and 5.0 nm of HfO_2 film were deposited on Si and SiO_2 at 300°C,

while SiCOH had less than a monolayer (0.13 nm) of HfO_2. Compared to TiO_2 CVD with $Ti(O^iPr)_4$ above, HfO_2 CVD showed lower selectivity. The lower selectivity could be due to the difference in surface reactivity of isopropoxide (O^iPr) ligand and butoxide (O^tBu) ligand precursor. HfO_2 films on Si and SiO_2 showed RMS roughness of 0.49 nm and 0.66 nm, respectively, with 2-4 nm tall particles. The particles could be due to the onset of crystallization as thicker HfO_2 films on SiO_2 showed higher roughness than the thinner HfO_2 films on Si. XRD was not performed because the films were sub 5 nm, but previous research proved that the HfO_2 process induces crystallization at 300 °C as the film thickness increases.[31]

The single precursor CVD of TiO_2 with $Ti(O^iPr)_4$ and HfO_2 with $Hf(O^tBu)_4$ proved that selective oxide deposition could be achieved with a metal alkoxide precursor. The selectivity was determined by the precursor for each process. However, as shown with the TiO_2 films in this study and by others[31,32], oxide films have increased crystallinity and corresponding roughness with increasing film thickness. To solve this crystallization issue, a nanolaminate structure with HfO_2 and TiO_2 was studied.

2.4.2 Selectivity study of the HfO_2/TiO_2 nanolaminate film

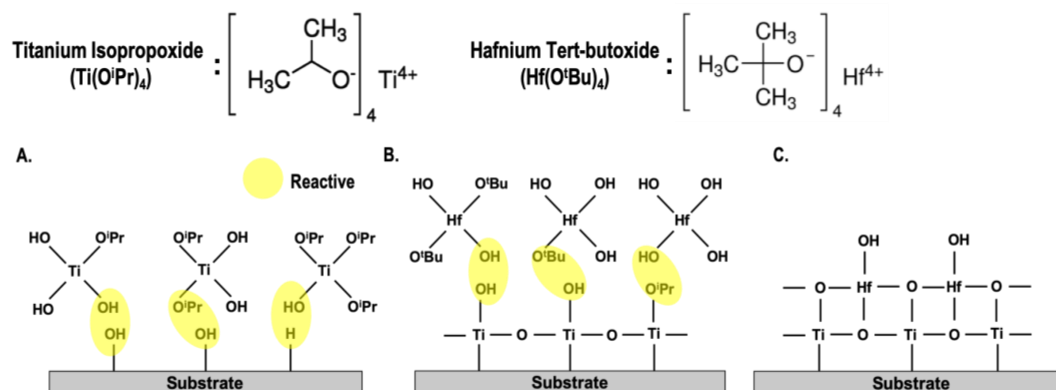

Figure 2.4 The chemical structures of $Ti(O^iPr)_4$ and $Hf(O^tBu)_4$ and the proposed reaction mechanism for the HfO_2/TiO_2 nanolaminate film. (A). Thermal decomposition of $Ti(O^iPr)_4$ forms hydroxyl ligand which readily react with hydroxyl (SiO_2) or hydrogen (Si) bonds on the substrate surface and nucleate pulsed CVD. (B). Sequentially dosed $Hf(O^tBu)_4$) also thermally decomposes and reacts on TiO_2 on the surface. (C). HfO_2/TiO_2 nanolaminate film deposited.

A proposed reaction mechanism of the HfO_2/TiO_2 nanolaminate film is described in Figure 2.4, consistent with other published mechanisms.[6,32] In the 1st step (Figure 2.4A), $Ti(O^iPr)_4$ is dosed on the substrate at 300 °C. Due to the high temperature, $Ti(O^iPr)_4$ decomposes and forms hydroxyl ligands. The hydroxyl is more reactive than the isopropoxide so that the decomposed precursor starts to react with hydrogen bonds on Si and hydroxyl bonds on SiO_2 and forms a TiO_2 film. After the $Ti(O^iPr)_4$ pulse, $Hf(O^tBu)_4$ is dosed (Figure 2.4B). With the same mechanism, $Hf(O^tBu)_4$ decomposes and reacts on the TiO_2 and forms the nanolaminate structure (Figure 2.4 C). Since SiCOH has $-OC_xH_y$ or $-C_xH_y$ bond, which is not reactive, it is hypothesized that deposition will not occur on the ideal SiCOH surface, inducing selective deposition. However, the precursor starts to react on minor reactive defect sites or physisorbs on SiCOH, inducing loss of selectivity.

The HfO_2/TiO_2 nanolaminate CVD process was performed as described in the experimental section. Three different Hf:Ti ratio nanolaminate films were fabricated by controlling the number of $Ti(O^iPr)_4$ and $Hf(O^tBu)_4$ pulses per cycle. From their Hf:Ti ratios, the samples were denoted as Hf-rich (Hf:Ti ratio: ~4:1), Ti-rich (Hf:Ti ratio: 1:~2.5), and highly Ti-rich (Hf:Ti ratio: 1:~7) nanolaminate films.

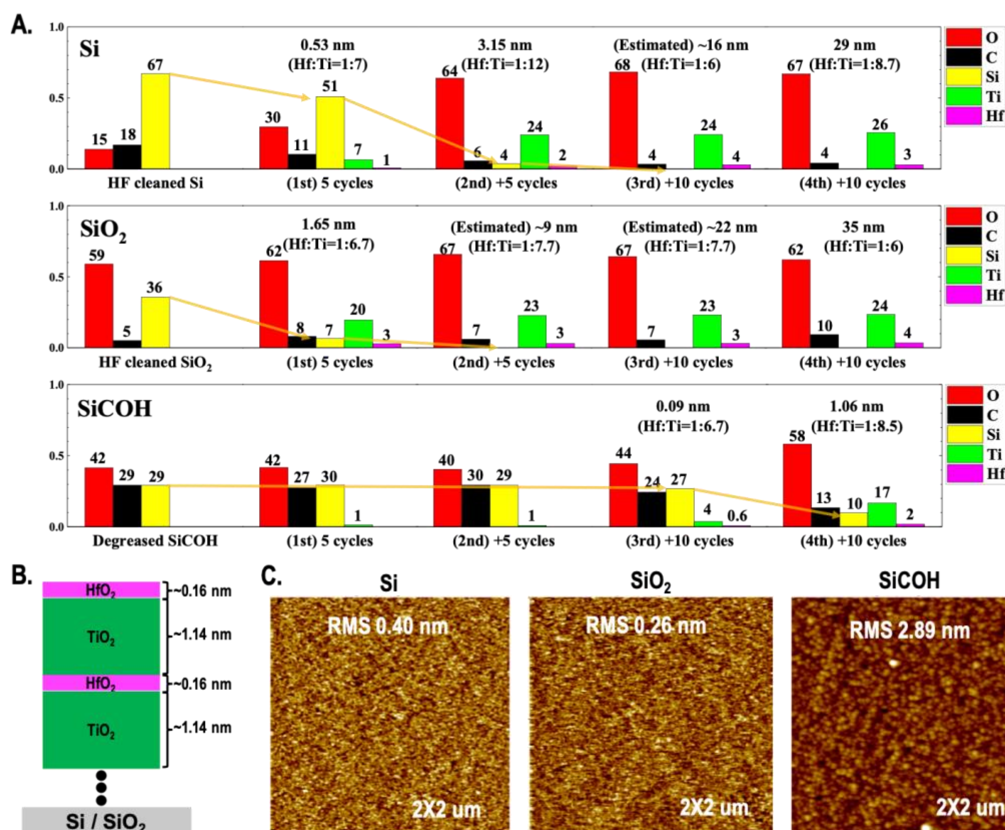

Figure 2.5 Analysis of 300°C Pulsed CVD of Highly Ti-rich HfO_2/TiO_2 Films. (A) XPS chemical composition, (B) estimated nanolaminate structure, and (C) AFM of Si, SiO_2, and SiCOH after total 30 cycles of the highly Ti-rich HfO_2/TiO_2 nanolaminate CVD process.

Figure 2.5 shows XPS chemical composition, estimated nanolaminate structure, and AFM images of the highly Ti-rich HfO_2/TiO_2. For the highly Ti-rich nanolaminates, 100 pulses of $Ti(O^iPr)_4$ and 1 pulse of $Hf(O^tBu)_4$ were dosed per cycle. During the first few

cycles, the samples were in the nucleation period; growth was slow, consistent with nuclei formation on the substrate surface. However, after additional deposition, the film had fast and constant deposition per cycle. For example, for the Si sample in Figure 2.5, during the 1st 10 cycles, Si had 3.15 nm deposition, which means the average growth rate during 1st 10 cycles was around 0.32 nm/cycle. However, after an additional 20 cycles, the overall film thickness on Si was 29 nm, corresponding to a growth of 1.3nm/cycle during the last 20 cycles. With this constant growth rate after the nucleation period and Hf:Ti ratio, the nanolaminate structure was estimated, as shown in Figure 2.5B. The SiO_2 substrate also had a nucleation period with slow growth. However, consistent with the hydroxyls on the SiO_2 surface being more reactive than hydrogens on the Si surface, SiO_2 exhibited faster nucleation than Si.

The selective deposition of highly Ti-rich HfO_2/TiO_2 nanolaminate can be observed in Figure 2.5A. After the 1st 10 cycles, 3.15 nm and 9 nm of films were deposited on Si and SiO_2, respectively, while only a 1% Ti peak and no Hf peak were detected from the SiCOH surface. After 10 more cycles, around ~16 nm (estimation from the growth rate after nucleation period) and ~22 nm of the nanolaminate films were deposited on Si and SiO_2, respectively, while the SiCOH had less than a monolayer (0.09 nm). After the last 10 more cycles, the thicknesses on Si, SiO_2, and SiCOH were 29 nm, 35 nm, and 1.06 nm, respectively. Therefore, it was observed that SiCOH had a significant nucleation delay for highly Ti-rich HfO_2/TiO_2, but the selectivity relative to Si and SiO_2 of the pulsed CVD process decreased as the number of cycles increased.

Figure 2.5C shows AFM images of highly Ti-rich HfO_2/TiO_2 nanolaminate films on Si, SiO_2, and SiCOH. The nanolaminate films on Si and SiO_2 were smooth films with the

RMS roughness 0.40 nm and 0.26 nm, respectively, without any significant particles. Compared to the AFM images of pure TiO_2 and HfO_2 films shown in Figure 2.2 and Figure 2.3, the nanolaminate films showed smoother films (for comparable thicknesses) without any particles. Further study of the film roughness of the nanolaminate will be covered in the next section. The RMS roughness on SiCOH was high (2.89nm) because the deposition on SiCOH (1.06 nm) was not sufficient to cover the whole surface.

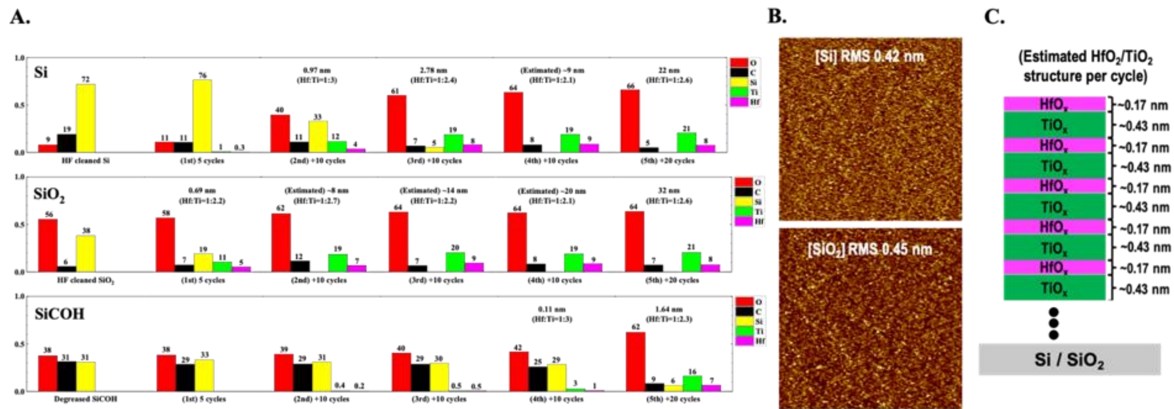

Figure 2.6 Analysis of Ti-rich HfO_2/TiO_2 nanolaminate Pulsed CVD at 300 °C. (A) XPS chemical composition of HF cleaned Si, HF cleaned SiO_2, and degreased SiCOH after the Ti-rich (Hf:Ti ratio: 1:~2.5) HfO_2/TiO_2 nanolaminate pulsed CVD process, (B) AFM images of nanolaminate films on Si and SiO_2 and (C) estimated nanolaminate structure.

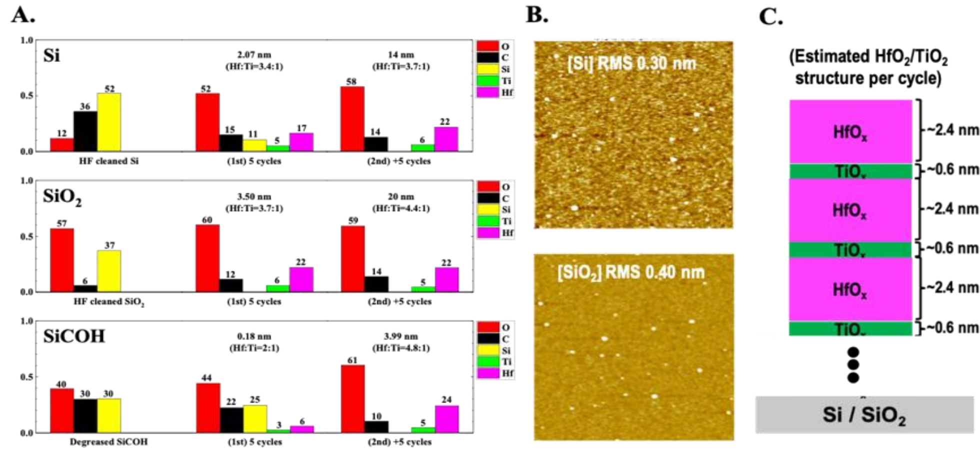

Figure 2.7 Analysis of Hf-rich HfO_2/TiO_2 nanolaminate Pulsed CVD at 300 °C. (A) XPS chemical composition of HF cleaned Si, HF cleaned SiO_2, and degreased SiCOH after the Hf-rich (Hf:Ti ratio: ~4:1) HfO_2/TiO_2 nanolaminate pulsed CVD process, (B) AFM images of nanolaminate films on Si and SiO_2 and (C) estimated nanolaminate structure.

XPS chemical compositions, AFM images, and estimated nanolaminate structure for Ti-rich and Hf-rich nanolaminates are shown in Figure 2.6 and 2.7, respectively. All four nanolaminate films on Si and SiO_2 showed a smooth surface with around 0.4 nm RMS roughness. Hf-rich nanolaminate films had a few particles in the AFM images. The particle formation is consistent with the HfO_2 sublayer for the Hf-rich nanolaminate film being ~2.4 nm, which is thicker than any other sublayers and could initiate crystallization.

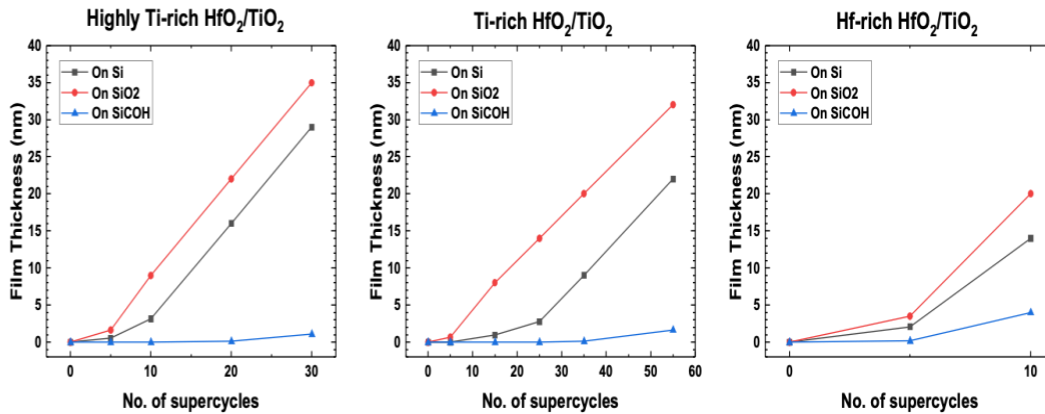

Figure 2.8 Film thickness on Si, SiO_2, and SiCOH for three different Hf:Ti ratio HfO_2/TiO_2 nanolaminates by pulsed CVD. Maximum y-axis (film thickness) values are set to 40 nm for all three graphs to compare thickness between the different processes.

To analyze the selectivity of the HfO_2/TiO_2 nanolaminate film in more detail, the nanolaminate film thickness on each sample on three different compositions is shown in Figure 2.8. As the Ti ratio increased, the nanolaminate films showed higher selectivity for thicker deposition, consistent with a greater nucleation delay on SiCOH for Ti-rich films. This tendency is affected by the selectivity of each single precursor CVD with $Ti(O^iPr)_4$ and $Hf(O^tBu)_4$. For example, TiO_2 CVD with $Ti(O^iPr)_4$ showed ~17 nm and ~40 nm selective deposition on Si and SiO_2, respectively. Conversely, HfO_2 CVD with $Hf(O^tBu)_4$ showed only ~2 nm and ~5 nm selective deposition on Si and SiO_2. In addition, the films on SiO_2 showed higher selectivity than the films on Si. It is consistent with the hydroxyl bonds on SiO_2 having higher reactivity than hydrogen bonds on Si, and, therefore, more rapid nucleation occurs on SiO_2.

2.4.3 Crystallization study of the HfO_2/TiO_2 nanolaminate film

AFM indicated that the nanolaminate films were smooth with less than 0.5 nm RMS roughness which was a clear difference in film roughness compared to the single oxide films with similar thickness. A detailed study on the effect of the nanolaminate structure on film crystallization was performed. To check both the effects of nanolaminate structure and sublayer thickness on film crystallization, XRD analysis was performed on two different samples. The 1st sample (Figure 2.9A) is highly Ti-rich HfO_2/TiO_2 nanolaminate film with thin sublayers on SiO_2, the same sample as shown in Fig. 2.5. The estimated sublayer thickness for this sample was around 1.14 nm and 0.16 nm for TiO_2 and HfO_2, respectively. The total thickness of the nanolaminate film was 35 nm. The 2nd sample had similar a Hf:Ti ratio (1:~7) and total thickness (~40 nm) but thicker sublayers (Figure 2.9B). The sublayer thicknesses were 12.4 nm and 1.6 nm for TiO_2 and HfO_2, respectively, around 10x thicker than those of the thin sublayer sample.

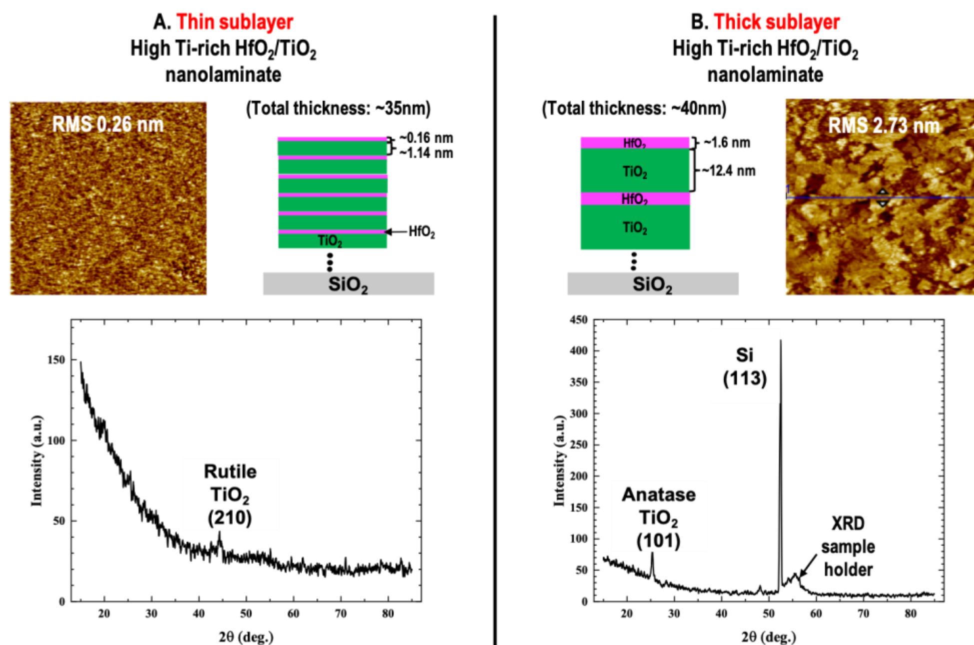

Figure 2.9 AFM and XRD Study on the Effect of Sublayer Thickness on Crystallinity. (A) The thin sublayer nanolaminate film had a smooth surface with 0.26 nm RMS roughness. The film was almost amorphous, with only a tiny rutile TiO_2 (210) peak. (B) The thick sublayer (~10 x thicker sublayer) nanolaminate film with similar total thickness had a rough surface with 2.73 nm RMS roughness. The film showed clear anatase TiO_2 (101) peak, indicating that the nanolaminate structure could not prevent crystallization.

The AFM images of the two samples showed a significant difference. The RMS roughness of the thin sublayer sample was 0.26 nm which was a similar range with other nanolaminate films. However, the RMS roughness of the thick sublayer sample was 2.73 nm, which is closer to that of the thick TiO_2 film shown in Figure 2.2. From the XRD pattern, the thin sublayer sample showed a tiny rutile TiO_2 (210) peak; however, no prominent peaks were detected consistent with an almost amorphous structure. However, the thick sublayer sample showed a clear anatase TiO_2 (101) peak, proving that the film had crystallization consistent with its rough surface. Conversely, the HfO_2 crystallization peak was not detected even from the thick sublayer sample; the HfO_2 sublayer thickness was around 1.6 nm, which

could be lower than its critical thickness to induce crystallization. It was shown from previous experiments that HfO_2 and TiO_2 single oxide films could induce crystallization as film thickness increases.[31,32] However, in the nanolaminate structure of these oxides, the crystallization could be suppressed as long as each HfO_2 and TiO_2 sublayer thickness is below their critical thicknesses to induce crystallization. It is noted that G. E. Testoni et al. documented similar limitations on sublayer thickness, but using at least one layer which is always amorphous, Al_2O_3.[34] In addition, previous research on HfO_2/TiO_2 structures also did not report on the limits on sublayer thickness for film crystallization.[27,28,38]

2.4.4 Selectivity in nm scale region for the HfO_2/TiO_2 nanolaminate film

To apply the HfO_2/TiO_2 nanolaminate CVD process to nanoscale patterning, the process was performed on the passivated Cu/SiCOH nanoscale patterned sample. The passivation on the Cu region desorbed during 350C UHV anneal (30 min) before the CVD process. Therefore, the passivation selectively passivated the damaged SiCOH. A passivated blanket SiCOH sample was loaded with the patterned sample to check any deposition on the SiCOH surface.

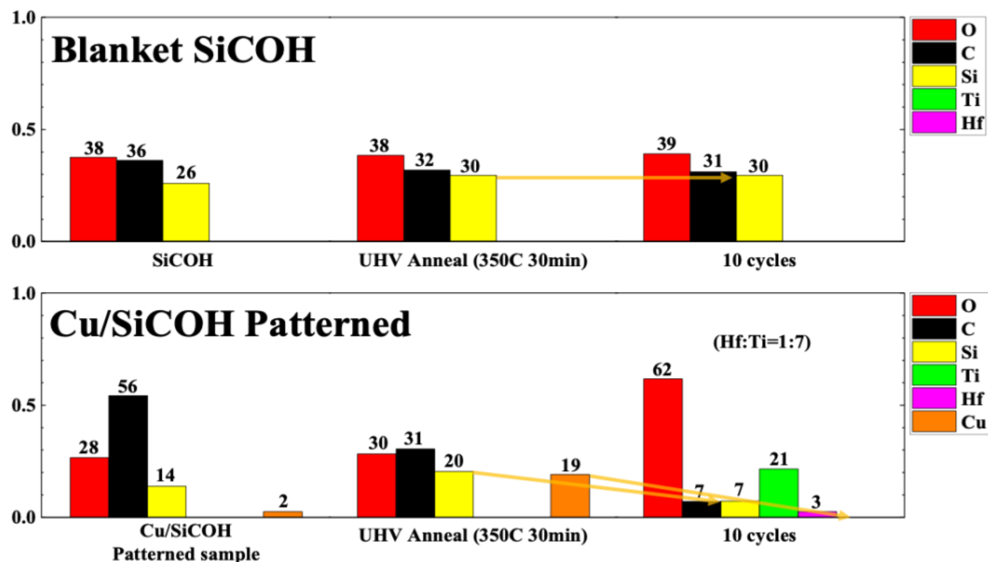

Figure 2.10 XPS of Selective CVD of Highly Ti-rich HfO_2/TiO_2 Nanolaminates on a Nanoscale Patterned Sample. XPS chemical composition of blanket SiCOH and Cu/SiCOH patterned samples before and after 10 cycles of highly Ti-rich HfO_2/TiO_2 nanolaminate CVD process.

Figure 2.10 shows the XPS chemical composition of the passivated blanket SiCOH and Cu/SiCOH patterned sample before and after 10 cycles of the highly Ti-rich HfO_2/TiO_2 nanolaminate pulsed CVD process. Before the pulsed CVD process, the samples were annealed in UHV (low 10^{-9} Torr region) at 350 °C for 30 min to remove the surface contaminants. After UHV anneal, it was seen that carbon fraction significantly decreased on the patterned sample (56% → 31%). This was consistent with both carbon contaminants on the sample from ambient air and carbon from the passivant on Cu being desorbed. After 10 cycles of highly Ti-rich HfO_2/TiO_2 nanolaminate CVD, the Cu peak was fully attenuated, consistent with deposition on the Cu surface. Hf:Ti ratio was 1:7, which is close to previous samples on Si and SiO_2. The Si percentage from the SiCOH surface of the patterned sample also decreased from 20 % to 7 %, while the blanket SiCOH was still clean. The reason for

the Si percentage decrease from the patterned sample became clear from the TEM image (Figure 2.11).

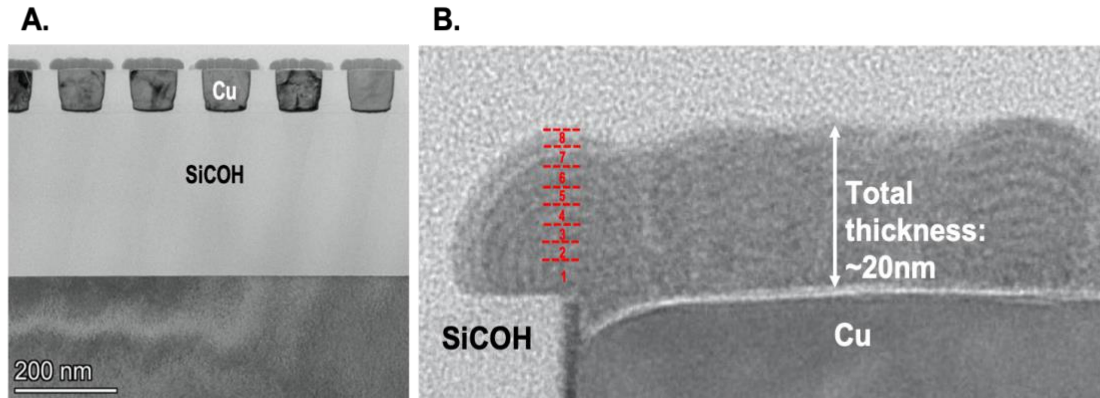

Figure 2.11 TEM Analysis of Selective CVD of a Highly Ti-rich HfO_2/TiO_2 nanolaminates on a Nanoscale Patterned Sample (A) TEM image of Cu/SiCOH patterned sample after 10 cycles of highly Ti-rich HfO_2/TiO_2 nanolaminate CVD. (B) Magnified view of a nanolaminate film on Cu inlay. As can be seen from the TEM images, the nanolaminate film was deposited only on Cu. From the magnified view (B), around 8 cycles of grey/black pattern were observed from the film, consistent with the nanolaminate structure.

Figure 2.11 shows the cross-sectional TEM image of the patterned sample from Figure 2.10 after the nanolaminate deposition. The patterned sample was composed of SiCOH and Cu surface, and the width of each surface was 90 nm for Cu and 50 nm for SiCOH. From the TEM images, around 20 nm of HfO_2/TiO_2 nanolaminate film was deposited on the Cu surface. However, the nanolaminate film had isotropic growth, inducing a lateral growth over the SiCOH region consistent with the Si % decrease in the XPS data, as shown in Figure 2.10. In the magnified view of the TEM image (Figure 2.11B), grey and black patterns were observed from the nanolaminate film. This pattern is consistent with the nanolaminate structure of HfO_2 and TiO_2 sublayers. The nanolaminate pattern had low contrast because each sublayer was ~1 nm. Around 8 black/grey patterns were observed from

the film, similar to the total number of cycles (10 cycles); this is consistent with the first two cycles forming a mixed oxide during the slow growth nucleation period. In conclusion, it is proven from the TEM study that the HfO_2/TiO_2 nanolaminate CVD process can have selective deposition in the nm scale region.

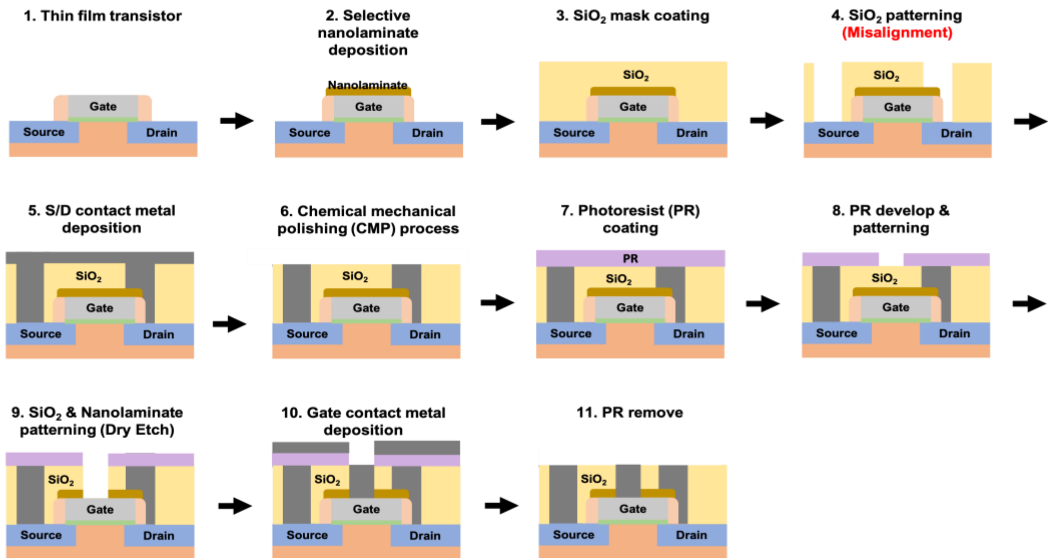

Figure 2.12 Application of selective HfO_2/TiO_2 nanolaminate film deposition on gate electrodes By selectively depositing HfO_2/TiO_2 nanolaminate film on the gate electrode, it can protect the gate from sequential etch processes and prevent short circuits with source/drain contact metals, which can be caused by misalignment. The HfO_2/TiO_2 nanolaminate film is patterned afterward for the gate contact deposition.

As the HfO_2/TiO_2 nanolaminate film showed selective deposition in the nm scale region, the above application in Figure 2.12 was proposed. The nanolaminate oxide film can be selectively deposited on the gate electrode before the source/drain contact metal connection is made. The nanolaminate layer can protect the gate electrode from sequential etching processes. In addition, as the transistor size decreases to the nm scale, there is more chance that patterning misalignment can induce electrical shorts between the source/drain contacts and the gate electrode. The nanolaminate oxide can prevent the electrical shorts even

if the misalignment occurs. After the source/drain contact metal connection, the nanolaminate film would be patterned for a gate contact metal connection. TiO_2/Al_2O_3 nanolaminate, previously reported by the authors[39], can be used in the same application. However, HfO_2/TiO_2 nanolaminate has an advantage in etching. Although, HfO_2, TiO_2, and Al_2O_3 can be dry-etched with the CF_4 + Ar plasma process, the HfO_2 etch rate is higher and closer to the TiO_2 etch rate than the Al_2O_3 etch rate.[40-43] Therefore, the HfO_2/TiO_2 nanolaminate film has a faster etch rate and may have higher etch selectivity to photoresist compared to the TiO_2/Al_2O_3 nanolaminate film. Due to this advantage in the etching process, HfO_2/TiO_2 nanolaminate is expected to be more favorable for certain applications.

2.5 Conclusions

Inherent selective deposition of amorphous HfO_2/TiO_2 nanolaminate film was studied. Metal alkoxide precursors, e.g., $Hf(O^tBu)_4$ and $Ti(O^iPr)_4$, can form oxide film without any oxygen co-reactant such as water. This enables investigation of halogen-free selective deposition on nanoscale patterned with a water-sensitive insulator such as SiCOH and halogen-sensitive metals such as Cu. Two precursors of a similar composition containing oxygen were studied, enabling investigation of the mechanisms of selectivity and crystallization control in a pulsed CVD process for selective nanolaminate formation. Due to the reactivity difference of precursors on Si, SiO_2, and SiCOH, the film was selectively deposited on Si and SiO_2 before nucleation occurred on SiCOH. The selectivity of the nanolaminate film was controlled by the ratio of each precursor. Since $Ti(O^iPr)_4$ showed higher selectivity than $Hf(O^tBu)_4$, up to ~20 nm of selective deposition on Si and SiO_2 was achieved with highly Ti-rich (Hf:Ti ratio: 1:~7) nanolaminate film before significant

nucleation occurred on SiCOH. The film was almost amorphous with less than 0.4 nm RMS roughness. However, if the sublayers were thicker than their critical thickness to induce crystallization, even the nanolaminate structure could not prevent crystallization. The nanolaminate CVD process showed around 20 nm of selective deposition on the Cu region from the Cu/SiCOH nanoscale patterned sample. Compared to TiO_2/Al_2O_3 nanolaminate pulsed CVD[39], the HfO_2/TiO_2 nanolaminate film in this study is more suitable for subsequent etching.[40-43] Therefore, the selective amorphous HfO_2/TiO_2 nanolaminate CVD process can be suitable for the nanoscale hard mask in the patterning process for nanometer-scale MOSFET fabrication.

Chapter 2, in full, is a reprint of the material as it appears in Applied Surface Science. Y. Cho, J. Huang, C.F. Ahles, Z. Zhang, K. Wong, S. D. Nemani, E. Yieh, and A.C. Kummel, “Inherent Selective Pulsed Chemical Vapor Deposition of Amorphous Hafnium Oxide / Titanium Oxide Nanolaminates”, *Applied Surface Science vol.600*, 154010 (2022). The dissertation author was the primary investigator and author of this paper.

Chapter 3

Inherent Selective Pulsed Chemical Vapor Deposition of Aluminum Oxide in nm scale

3.1 Abstract

Inherent selective pulsed chemical vapor deposition (CVD) of aluminum oxide on Si and SiO_2 in preference to SiCOH has been studied. SiCOH is alkyl ($-C_xH_y$) terminated SiO_2, which was used as a non-reactive surface. For aluminum oxide deposition, pulsed CVD processes using aluminum tri sec-butoxide (ATSB) and trimethylaluminum (TMA) were tested. ATSB alone can induce a pulsed thermal CVD reaction to selectively deposit aluminum oxide at 300°C sample temperature; around 4 nm of aluminum oxide were selectively deposited on Si and SiO_2 in preference to SiCOH. By adding a periodical pulse of TMA during ATSB pulses, higher selectivity was achieved with ~12 nm and ~14 nm of aluminum oxide on Si and SiO_2 with around 0.4 – 0.6 nm root mean square (RMS) roughness at 330°C sample temperature. The high selectivity persisted on the nanoscale: STEM showed that ~10 nm of aluminum oxide could be selectively deposited on patterned surfaces with sub 50 nm features. The selectively deposited AlO_x films showed low k (~4) dielectric performance with low leakage (around 10^{-6} A/cm^2 at ±2V for a 15 nm thick film). This selective aluminum oxide pulsed CVD process has the potential to be applicable in nanoscale fabrication, such as low k spacer and etch stop layer.

3.2 Introduction

As nanoscale fabrication becomes an important issue in leading-edge semiconductor fabrication, area selective deposition of nanoscale features has become a field of interest. Area selective deposition of oxides can be applied to double patterning on the nanoscale.[5,32] In addition, selective oxide deposition can be employed for etch stop barriers[39,44] or dielectric-on-dielectric structures for fully self-aligned vias.[45,46] For selective deposition, three methods are available: inherent selective deposition, selective deposition using surface passivation, and selective deposition using activation. The inherent selective deposition uses reactivity differences between precursors and different surfaces.[6-9,32,33,39,44] This method is more desirable as it does not require additional steps for passivation or activation and, therefore, is often less sensitive to defects; however, few studies have been done about inherent selective deposition. The majority of selective depositions are based on selective deposition using passivation. This method uses a passivant, such as long-chain alkanes, to prevent nucleation of precursors on a particular surface, thereby inducing selective deposition on an un-passivated surface.[11-13] In addition, selective activation, such as electron beam-induced ALD, can induce selective deposition.[16-17] However, selective activation requires additional steps to activate the surface and may require specific sample geometry.

CVD is a widely used deposition method in the semiconductor industry. Among various CVD methods, thermal CVD uses high sample temperature, which decomposes one or more precursors and forms reactive ligands such as hydroxyl (-OH) to promote film formation.[6,32,39,44] For selective oxide deposition, water-free deposition is desirable as water can induce poor selectivity[1] and damage metals and low k dielectrics, such as SiCOH. It was previously reported that metal alkoxide precursors could thermally decompose and form

oxide films. [6,32,39,44] Since metal alkoxide precursors have abundant oxygen on their ligands, no additional oxygen precursor, such as water, was required during deposition. For example, with the pulsed CVD process of titanium isopropoxide ($Ti(O^iPr)_4$) and hafnium tertbutoxide ($Hf(O^tBu)_4$), selective TiO_2[32] and HfO_2[6] deposition were achieved, respectively, on Si and SiO_2 in preference to SiCOH. SiCOH is porous methyl-terminated SiO_2, a low k dielectric used in the semiconductor industry.[23-26] This selective deposition process with metal alkoxide precursors was also demonstrated with a passivation process which covers the sample surface with $–(O)C_xH_y$ bonds.[6] However, as oxide films became thicker, crystallization occurred along with the resulting formation of a rough film. To solve the film roughness issue, selective oxide deposition with a nanolaminate structure was performed by periodically depositing two different oxide films.[39,44] However, the nanolaminate structure has the drawback of complicating the etching process for use as a temporary etch stop layer.

Al_2O_3 is a desirable material to selectively deposit because it is amorphous regardless of its thickness, reducing the risk of forming a rough surface. Al_2O_3 is also a well-known capping and dielectric layer in the semiconductor industry. L. Cao et al. studied AlO_x ALD using aluminum tri-sec-butoxide (ATSB) and oxygen precursors such as H_2O and O_2 plasma.[47] The authors showed that ATSB without coreactant has a thermal CVD reaction above 250°C sample temperature. However, the study focused on the AlO_x ALD process using oxygen-containing coreactants and did not study selective deposition. Liu et al.[48] and Bobb-Semple et al.[11] studied selective AlO_x ALD. For AlO_x deposition, both studies used TMA and water, which is a commonly used AlO_x deposition method. For selective deposition, both Liu et al. and Bobb-Semple et al. used liquid phase octadecylphosphonic acid to passivate oxide or metal surfaces to have selective aluminum oxide deposition on the

unpassivated surfaces. Liu et al. reported a maximum of ~30 nm of selective AlO_x deposition.[48] However, these studies focused on selective deposition using a passivant, not on inherent selective deposition nor selective deposition in the nm scale.

The present study investigated the inherent selective AlO_x CVD using ATSB and trimethylaluminum (TMA). The pulsed CVD with ATSB at 300°C sample temperature demonstrated ~4 nm of selective AlO_x deposition on Si and SiO_2 in preference to SiCOH. TMA was employed since it has the potential to react with excess oxygen from nucleated metal alkoxide precursors to increase selectivity. Pulsed CVD with ATSB and TMA at 300°C sample temperature increased the selectivity; ~10 nm of AlO_x were selectively deposited on Si and SiO_2. However, excess TMA inhibited the film growth on Si and SiO_2. Higher sample temperature (330°C) increased the reactivity of ATSB; therefore, more TMA pulses could be added, inducing an increase in selectivity; 12 and 14 nm of AlO_x were selectively deposited on Si and SiO_2. The AlO_x films were smooth with 0.4 - 0.6 nm RMS roughness. From the electrical characterization, the AlO_x film showed dielectric behavior with k = ~4 and around 10^{-6} A/cm^2 leakage current at ±2V; the desirable and unusual low dielectric constant of the AlO_x was consistent with sub-stoichiometric composition. The pulsed CVD with ATSB and TMA at 330°C sample temperature was tested on Cu/SiCOH nanoscale patterned sample and demonstrated ~10 nm of selective AlO_x deposition on the Cu surfaces and no detectable AlO_x on SiCOH.

3.3 Experimental

The selective AlO_x pulsed CVD was tested on three different substrates: Si, SiO_2, and SiCOH. The size of each substrate was ~2 x ~12 mm. The samples were sequentially degreased with acetone, methanol, and deionized water for 15 seconds each. To remove surface native oxide, degreased Si and SiO_2 were wet cleaned in a 0.5% diluted hydrofluoric acid solution for 30 seconds. After the cleaning, the samples were blown with an N_2 air gun to remove residual solution on the sample surface. The three samples were loaded into the chamber on a single sample holder, so they had the same CVD process to quantify the selectivity. For the nanoscale selectivity test, a Cu/SiCOH nanoscale patterned sample was used. The Cu/SiCOH sample was wet cleaned with the same degreasing process explained above. Since the SiCOH surface of the patterned sample was damaged from the initial chemical mechanical polishing (CMP) process and, thus, not fully covered with $-OC_xH_y$ or $-C_xH_y$ bonds, an additional passivation process was done after degreasing the sample with a proprietary passivation process from Applied Materials. After the passivation, the patterned sample was loaded with a blanket SiCOH sample to check selective deposition in the Cu region.

The vacuum chamber system consisted of three chamber parts. A load lock chamber was employed to load and retrieve samples. It also worked as a buffer chamber between the deposition chamber and ultra-high vacuum (UHV) X-ray photoelectron spectroscopy (XPS) chamber to prevent gas phase precursor flows into the UHV chamber. The load lock chamber was pumped by a turbopump (Pfeiffer TPU 060) and a mechanical backing pump (Edwards RV3). The deposition chamber was also pumped by a turbopump (Pfeiffer TPU 060) and a mechanical backing pump (Edwards RV3). A Cu sample holder with a cartridge heater

inserted inside was located at the end of the transfer arm of the deposition chamber. Dosing lines for ATSB, TMA, and N_2 purge gas were connected to the deposition chamber. The UHV chamber was employed for *in-vacuo* XPS. The chamber was pumped by an ion pump (Agilent Varian VacIon 300 StarCell) to UHV pressure (low 10^{-9} torr). The samples were transferred *in-vacuo* for XPS analysis to prevent exposure to the ambient air.

During the CVD process, the deposition chamber wall and dosing lines were kept at 150°C. Samples were heated up to 300°C and 330°C using the cartridge heater inside the Cu platform. The precursor pulse pressure was controlled by a pneumatic valve open time and the precursor bottle temperature. The ATSB bottle was heated to 110°C to have a sufficient vapor pressure. The TMA bottle was kept at room temperature (~21°C). In addition, no push gas was used for both ATSB, and TMA doses. The valve open time for each precursor was set to 800 ms and 15 ms for ATSB and TMA, respectively. The precursor pulses were monitored by the pressure spikes inside the chamber. N_2 gas was continuously purged during the CVD process to remove the residual precursors inside the dosing chamber. AlO_x CVD was tested with the single precursor pulsed CVD with ATSB and the pulsed CVD with supercycle of ATSB and TMA. For ATSB single precursor pulsed CVD, three different purging times between each ATSB pulse were tested: 10, 60, and 240 seconds. For the supercycle with ATSB and TMA, one pulse of TMA was employed with every 80/120/160 ATSB pulses to check the effect of TMA pulse frequency on the selectivity of the CVD process. The purge time between different precursor pulses was set to 60 seconds. The purge time between ATSB pulses was set to 10 seconds. Both CVD processes were tested at 300°C and 330°C sample temperatures to check the effect of the sample temperature on the selectivity.

After the AlO_x deposition, *in-vacuo* XPS analysis was performed. A monochromatic Al Kα source (1486.7 eV) and XM 1000 MkII/SPHERA (Omicron Nanotechnology) hemispherical analyzer were used for the measurement. The anode voltage, the filament emission current, and hemisphere analyzer pass energy were set to 10 kV, 25 mA, and 50 eV, respectively. The XPS detector was aligned to 30° from the sample surface. The XPS analysis was performed with CASA XPS v.2.3 and utilized Shirley background subtraction. Each element composition was derived by normalizing to the sum of all elements. The oxide film thickness was derived from Si substrate signal attenuation from the XPS result.[6,32] When the Si signal was not detected (film thickness more than 4 nm), the thickness was measured by ex-situ ellipsometry (J. A. Woollam M-2000D). After the whole in-vacuo CVD and XPS, the ex-situ atomic force microscopy (AFM) (Park Systems XE7/tapping mode) and scanning transmission electron microscopy (STEM) (FEI F200X G2) were performed.

For the electrical characterization of the AlO_x film, capacitors were fabricated. The bottom electrode was the Si substrate, while thermal evaporation (Denton 502A) was employed to fabricate the top electrode (Ni). The Ni top electrode had a contact diameter of 150 um and a thickness of 30 nm. For the post-deposition anneal, O_2 anneal (450 °C for 30min), and sequential forming gas anneal (330 °C, 350 °C, and 380 °C three steps anneal for 15 min each) were employed. The capacitance-voltage (C-V) and current-voltage (I-V) characteristics of the capacitor were probed by the Keithley 4200A SCS parameter analyzer.

3.4 Results and Discussion

3.4.1 Selectivity of the AlO_x pulsed CVD with Aluminum tri-sec butoxide

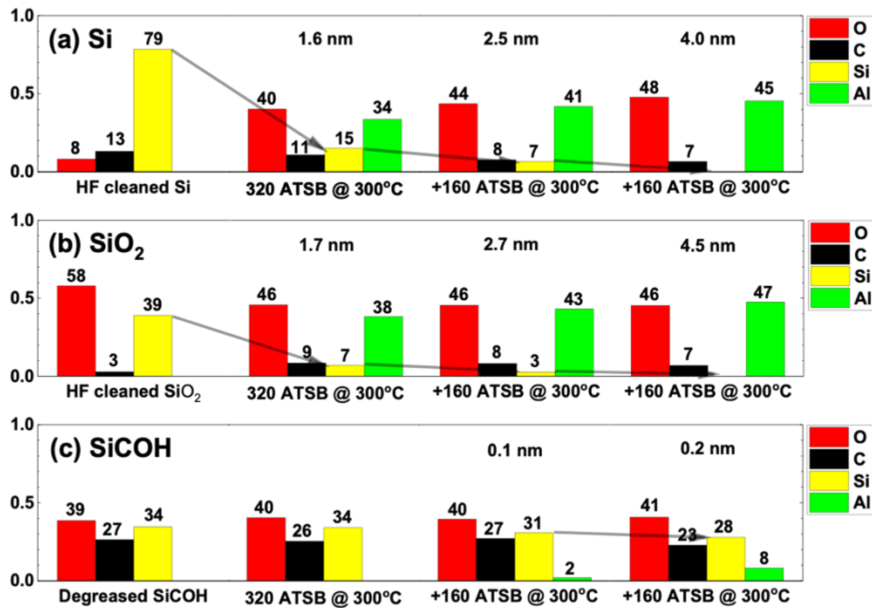

Figure 3.1 Analysis of AlO_x Pulsed CVD with ATSB at 300°C (10 seconds purge time). XPS chemical composition of (a) HF cleaned Si, (b) HF cleaned SiO_2, and (c) degreased SiCOH during AlO_x pulsed CVD with ATSB.

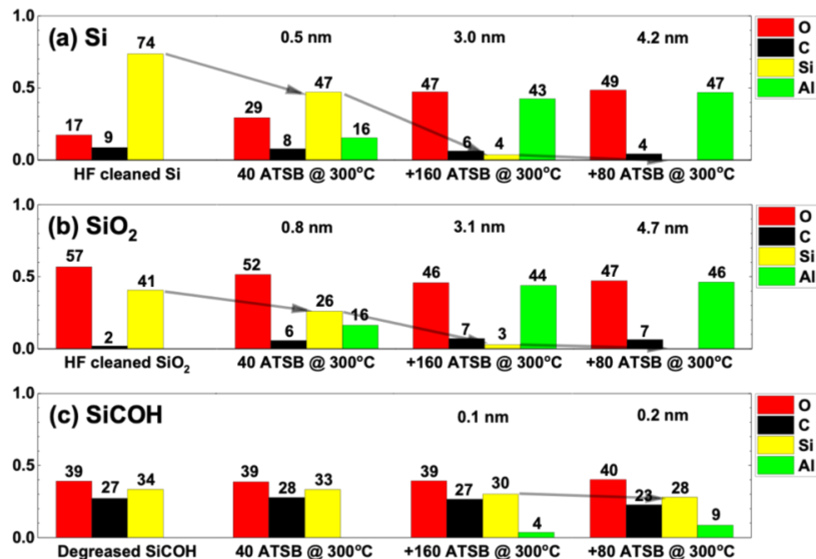

Figure 3.2 Analysis of AlO_x Pulsed CVD with ATSB at 300°C (60 seconds purge time). XPS chemical composition of (a) HF cleaned Si, (b) HF cleaned SiO_2, and (c) degreased SiCOH during AlO_x pulsed CVD with ATSB.

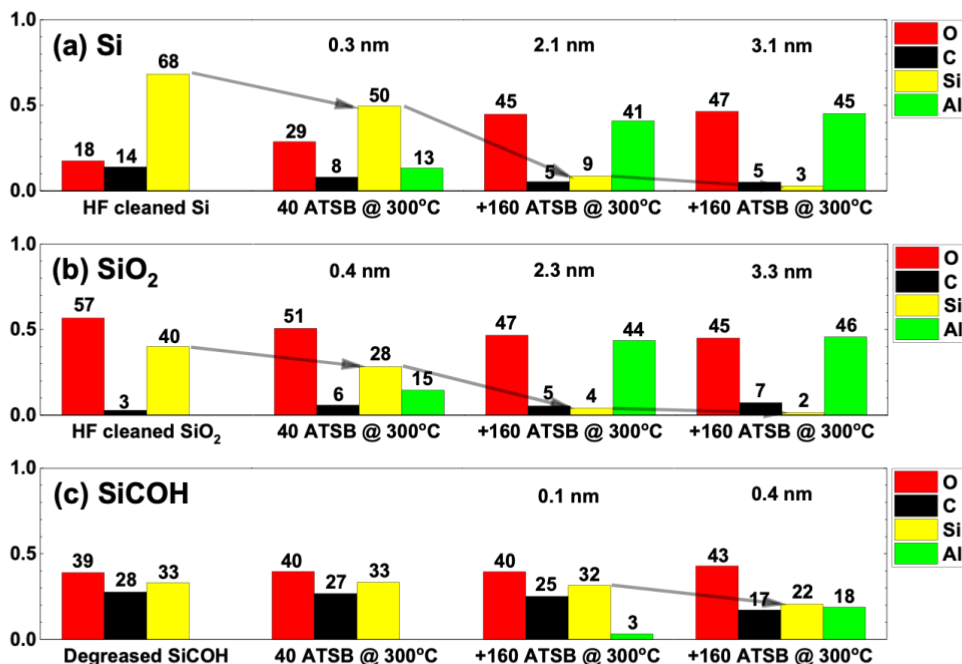

Figure 3.3 Analysis of AlO_x Pulsed CVD with ATSB at 300°C (240 seconds purge time). XPS chemical composition of (a) HF cleaned Si, (b) HF cleaned SiO_2, and (c) degreased SiCOH during AlO_x pulsed CVD with ATSB.

The inherent selectivity of single precursor (ATSB) pulsed CVD was first tested. ATSB pulses were dosed with constant purge time. Three purge times (10, 60, and 240 seconds) were tested. Figure 3.1 shows the XPS chemical composition of Si, SiO_2, and SiCOH surface during the ATSB pulsed CVD process at 300 °C sample temperature. The purge time between ATSB pulses was set to 10 seconds. At 300 °C sample temperature, thermal decomposition of ATSB prevailed and induced AlO_x film deposition.[47] As more ATSB pulses were dosed, AlO_x films were formed on Si and SiO_2 surfaces, as shown in Figure 3.1; Si signal composition became smaller, and Al signal appeared as the deposition continued. After 640 ATSB pulses, Si peaks were fully attenuated from Si and SiO_2. The AlO_x thickness on Si and SiO_2 was 4.0 nm and 4.5 nm, respectively. On SiCOH, however,

less than a monolayer (~0.2 nm) of AlO_x was deposited after 640 ATSB pulses. The selective deposition was due to the inherent reactivity difference of precursor-mediated chemisorption of ATSB.

ATSB pulsed CVD at 300 °C sample temperature was also tested with 60 and 240 seconds purge times. The XPS analysis of ATSB pulsed CVD with 60 seconds and 240 seconds purge times are shown in Figure 3.2 and 3.3, respectively. However, no further increase in selectivity was detected. The CVD with 60 seconds purge time showed similar selectivity to the result with 10 seconds purge time. Selectivity became lower as the purge time was increased to 240 seconds. In sum, the ATSB pulsed CVD at 300 °C had a most selective process with a purge time between 10 and 60 seconds.

ATSB pulsed CVD was also tested at 330 °C sample temperature to check whether a higher sample temperature can improve selectivity. The XPS analysis is shown in Figure 3.4. After 350 ATSB pulses, Si and SiO_2 had around 4.4 and 5.6 nm of AlO_x deposition, respectively. It was observed that the growth rate per ATSB pulse increased as the sample temperature increased. This higher temperature and consequently higher growth rate were used in the pulsed CVD process with ATSB and TMA in a later section. However, the CVD process at 330 °C showed similar selectivity compared to the result at 300 °C (around 4-5 nm of AlO_x on Si and SiO_2 and less than a monolayer (0.2-0.3 nm) of AlO_x on SiCOH), consistent with a large temperature process window for the selective pulsed CVD.

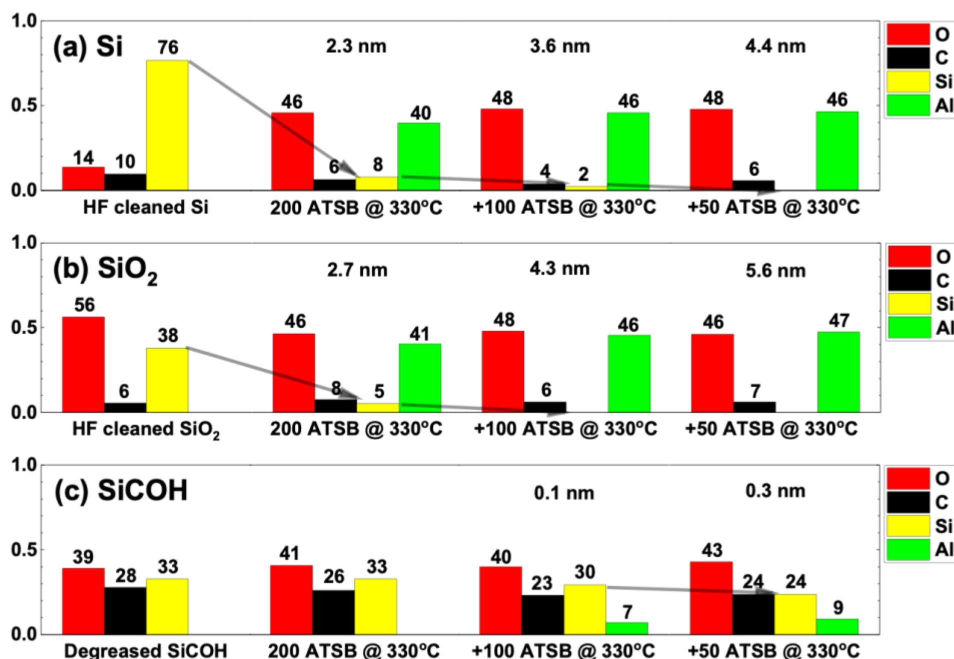

Figure 3.4 Analysis of AlO_x Pulsed CVD with ATSB at 330°C (10 seconds purge time). XPS chemical composition of (a) HF cleaned Si, (b) HF cleaned SiO_2, and (c) degreased SiCOH during AlO_x pulsed CVD with ATSB.

3.4.2 Selectivity of the AlO_x pulsed CVD with Aluminum tri-sec butoxide and TMA

Pulsed CVD with ATSB and TMA was tested to determine if adding TMA increases the selectivity of the AlO_x CVD. In each supercycle, one pulse of TMA was dosed, and the number of sequential ATSB pulses varied from 80 to 160 at 300 °C sample temperature. The 1st test was done with one pulse of TMA and 160 pulses of ATSB per supercycle. As shown in Figure 3.5, after six supercycles, the AlO_x thickness on Si and SiO_2 were 5.9 and 6.5 nm, respectively, while less than a monolayer (~0.2 nm) of AlO_x was deposited on SiCOH. Compared to the selectivity of the AlO_x CVD with ATSB only at 300 °C in Figure 3.1, ~2 nm of more AlO_x was selectively deposited.

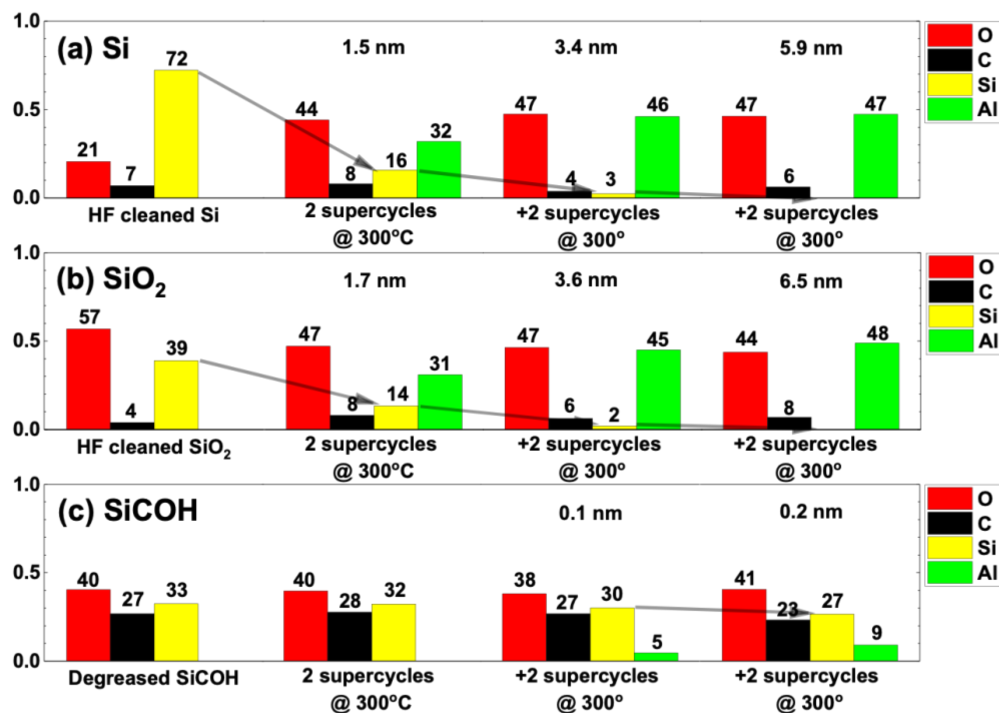

Figure 3.5 Analysis of AlO_x Pulsed CVD with one pulse of TMA and 160 pulses of ATSB per supercycle at 300°C. XPS chemical composition of (a) HF cleaned Si, (b) HF cleaned SiO_2, and (c) degreased SiCOH during AlO_x pulsed CVD with ATSB and TMA.

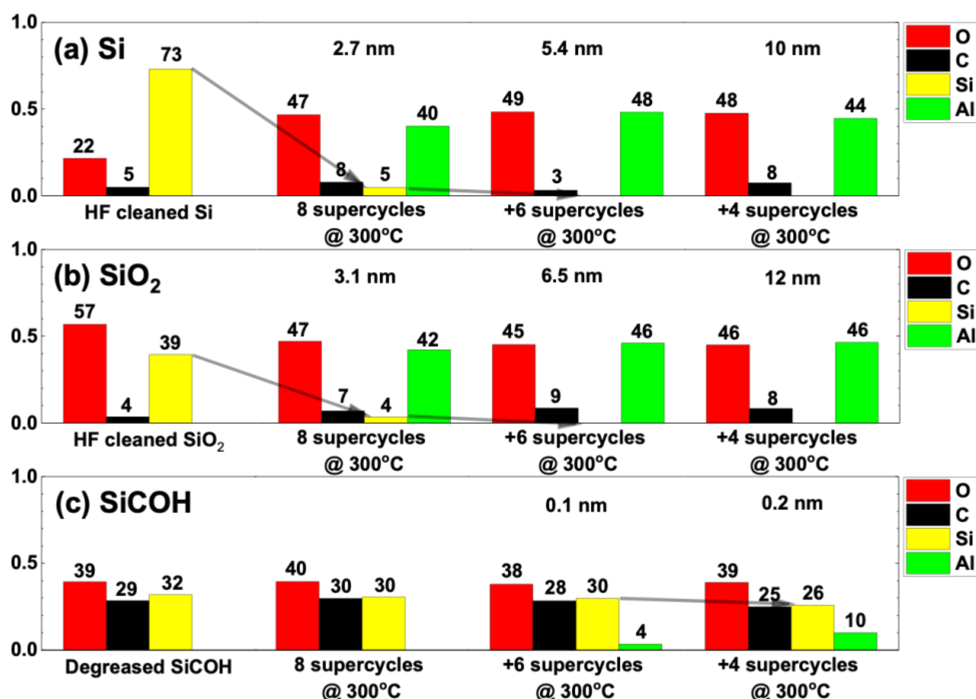

Figure 3.6 Analysis of AlO_x Pulsed CVD with one pulse of TMA and 120 pulses of ATSB per supercycle at 300°C. XPS chemical composition of (a) HF cleaned Si, (b) HF cleaned SiO_2, and (c) degreased SiCOH during AlO_x pulsed CVD with ATSB and TMA.

To check if a further increase in selectivity can be achieved, more frequent TMA pulsing was tested with one pulse of TMA and 120 pulses of ATSB per supercycle at 300 °C sample temperature, which is shown in Figure 3. The 1st 8 supercycles showed slow growth as the precursor slowly nucleated on Si and SiO_2 surfaces with around 3 nm of AlO_x deposition. After additional 10 supercycles, around 10 and 12 nm of AlO_x were selectively deposited on Si and SiO_2 in preference to SiCOH (~0.2 nm). This selectivity was higher than the CVD process with ATSB and the CVD process with less TMA pulse (1 pulse of TMA + 160 pulses of ATSB/supercycle).

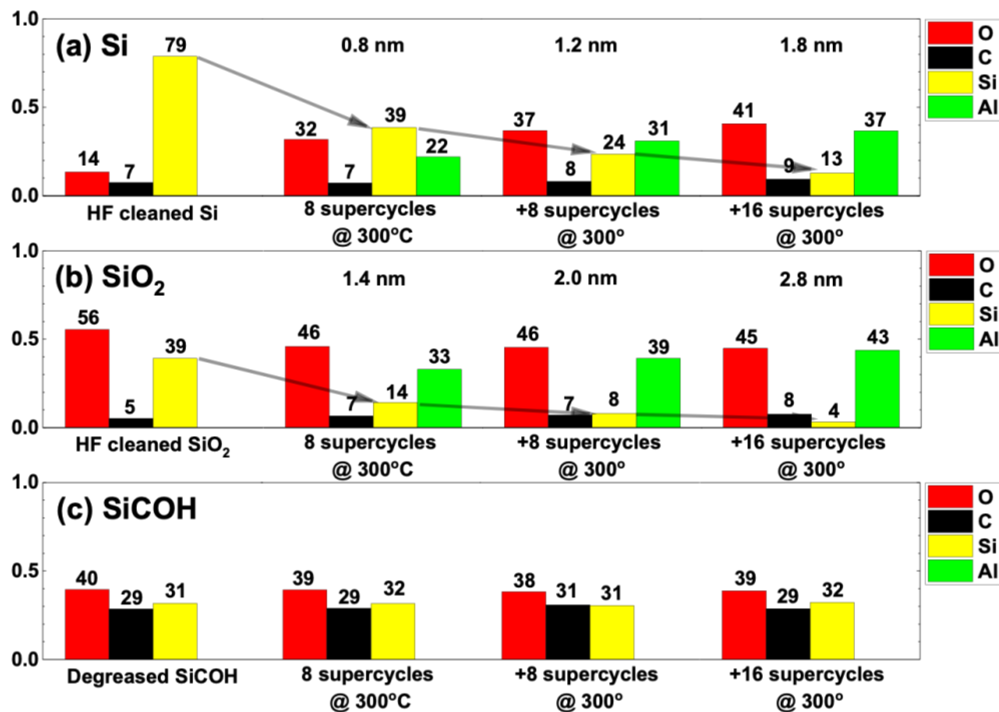

Figure 3.7 Analysis of AlO_x Pulsed CVD with one pulse of TMA and 80 pulses of ATSB per supercycle at 300°C. XPS chemical composition of (a) HF cleaned Si, (b) HF cleaned SiO_2, and (c) degreased SiCOH during AlO_x pulsed CVD with ATSB and TMA.

To check selectivity with even higher TMA frequency supercycles, an additional sample set with one pulse of TMA and 80 ATSB pulses per supercycle was tested at 300 °C sample temperature. The XPS analysis of the CVD process is shown in Figure 3.7. After 32 supercycles, SiCOH remained nuclei-free. However, the growth rate slowed down both on Si and SiO_2: AlO_x growth rate during each dosing changed as 0.100 nm/cycle → 0.050 nm/cycle → 0.037 nm/cycle on Si and 0.175 nm/cycle → 0.075 nm/cycle → 0.050 nm/cycle on SiO_2. It is hypothesized that TMA reacts on oxide nuclei formed by metal alkoxide precursor (ex: ATSB, $Hf(O^tBu)_4$, and $Ti(O^iPr)_4$) and leaves a less reactive methyl bond on the surface.[39] As fewer ATSB pulses were dosed per cycle with the same number of TMA

pulse, fewer reactive AlO_x nuclei were formed during the ATSB half cycle. Therefore, the density of reactive sites after the TMA half-cycle decreased as the number of ATSB pulses per supercycle decreased, inducing growth inhibition. Further growth mechanisms for the AlO_x CVD with TMA and ATSB will be discussed below.

The periodical pulsing of TMA helped increase the selective AlO_x deposition, but too frequent TMA pulsing stopped the oxide growth on growth surfaces such as Si and SiO_2. Therefore, it was found that one pulse of TMA and 120 pulses of ATSB per supercycle was the optimal process condition to achieve the highest selectivity at 300 °C sample temperature. An additional test with 120 pulses of ATSB dosing followed by one pulse of TMA per supercycle tested whether the order of two precursors affects the selectivity. However, as shown in XPS analysis in Figure 3.8, similar selectivity (9 nm on Si, 11 nm on SiO_2 vs. 0.2 nm on SiCOH) was achieved, proving the order of precursors does not affect the selectivity.

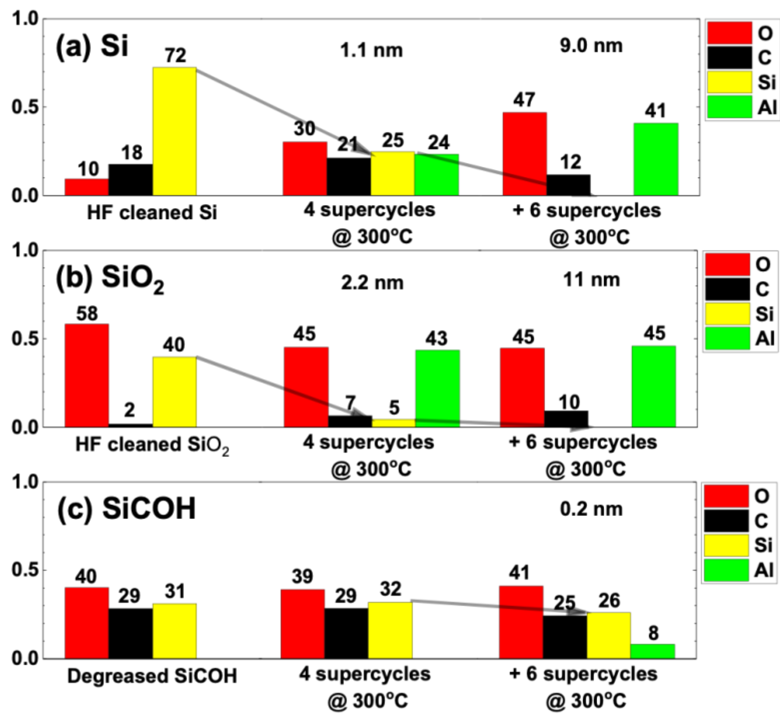

Figure 3.8 Analysis of AlO_x Pulsed CVD with 120 pulses of ATSB and one pulse of TMA per supercycle (reverse order of precursors) at 300°C. XPS chemical composition of (a) HF cleaned Si, (b) HF cleaned SiO_2, and (c) degreased SiCOH during AlO_x pulsed CVD with ATSB and TMA.

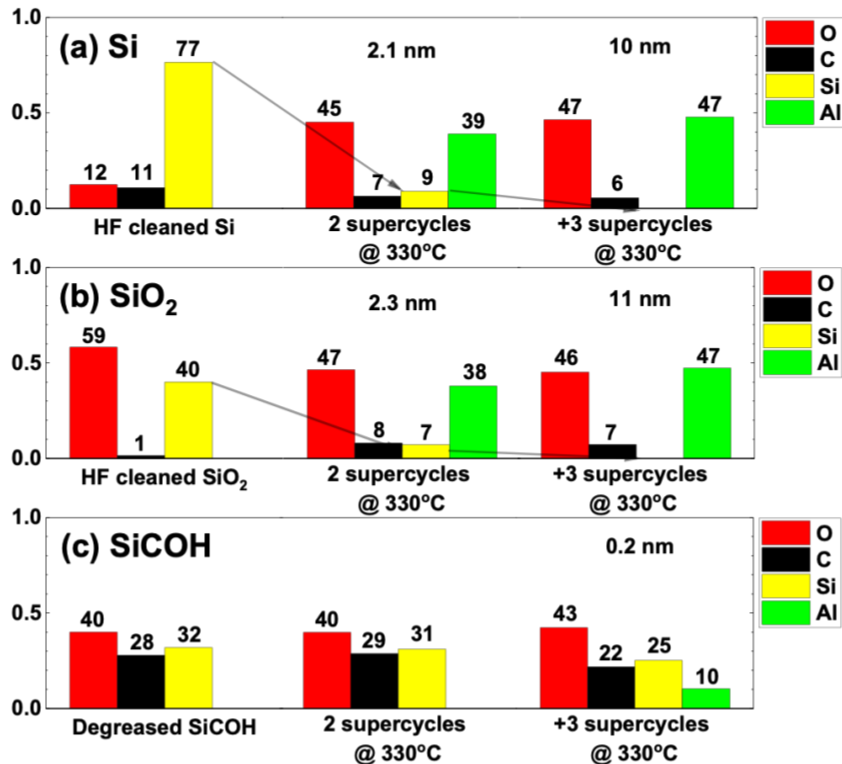

Figure 3.9 Analysis of AlO_x Pulsed CVD with one pulse of TMA and 120 pulses of ATSB per supercycle at 330°C. XPS chemical composition of (a) HF cleaned Si, (b) HF cleaned SiO_2, and (c) degreased SiCOH during AlO_x pulsed CVD with ATSB and TMA.

The CVD process with TMA and ATSB was tested at a higher sample temperature, 330 °C. The TMA + ATSB CVD process (1 pulse of TMA + 120 pulses of ATSB / supercycle), optimized at 300 °C sample temperature, was tested at 330 °C. However, as shown in Figure 3.9, the amount of selective AlO_x deposition on Si and SiO_2 was similar to that achieved at 300 °C with the same process. After 5 supercycles, around 10 nm and 11 nm of AlO_x were selectively deposited on Si and SiO_2, respectively, while less than a monolayer (0.2 nm) was deposited on SiCOH. Similar to the AlO_x CVD with ATSB only, the selectivity of the AlO_x CVD with ATSB and TMA was not affected by the sample temperature. This

similarity in both CVD processes is consistent with the nucleation of metal alkoxide precursor on nonreactive SiCOH surfaces determining the limit of selectivity.[32]

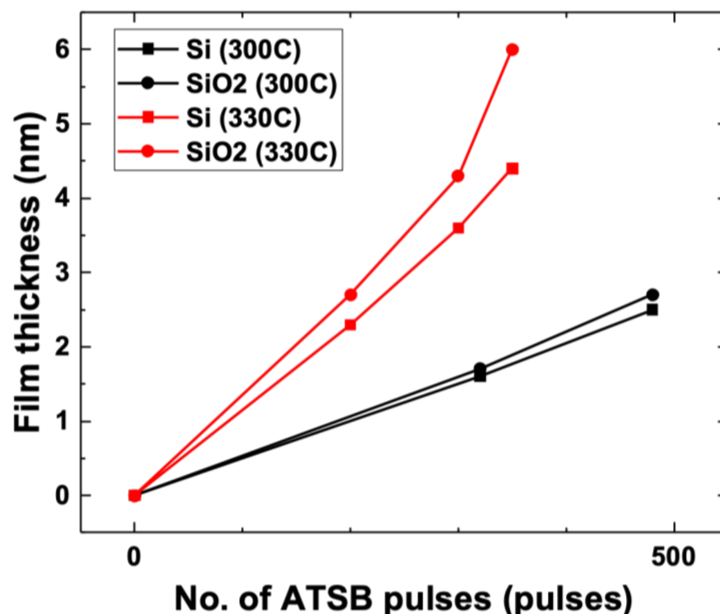

Figure 3.10 The growth curve of AlO_x Pulsed CVD with ATSB on Si (square) and SiO_2 (circle) at 300°C (black) and 330°C (red).

Even with the similar selectivity in both temperatures, it was observed that ATSB had a higher growth rate on Si and SiO_2 at 330 °C than at 300 °C. Figure 3.10 shows the AlO_x film growth from ATSB pulsed CVD at 300 °C and 330 °C. With a similar number of ATSB pulses, around 2x faster film growth was observed on both Si and SiO_2 at 330 °C. From the TMA + ATSB CVD process study at 300 °C sample temperature, periodical TMA pulses helped increase the selectivity, but excess TMA per a certain amount of ATSB nucleation could inhibit the film growth. Since ATSB had a higher growth rate at 330 °C, it was hypothesized that more frequent TMA could be added in each supercycle at 330 °C, thereby increasing selectivity. The CVD process with more frequent TMA was tested to prove the hypothesis. In each supercycle, the number of ATSB pulses was decreased from 120 to 80 to

increase the TMA frequency. This TMA richer process showed growth inhibition at 300 °C sample temperature, as shown in Figure 3.7. However, the TMA richer process showed decent film growth without a growth inhibition at 330 °C, as shown in Figure 3.11. After 15 supercycles, 12 nm and 14 nm of AlO_x were deposited on Si, and SiO_2, respectively, with small nucleation (~0.2 nm) on SiCOH. In conclusion, more frequent TMA could be implemented at a higher sample temperature (330 °C) to increase the selectivity.

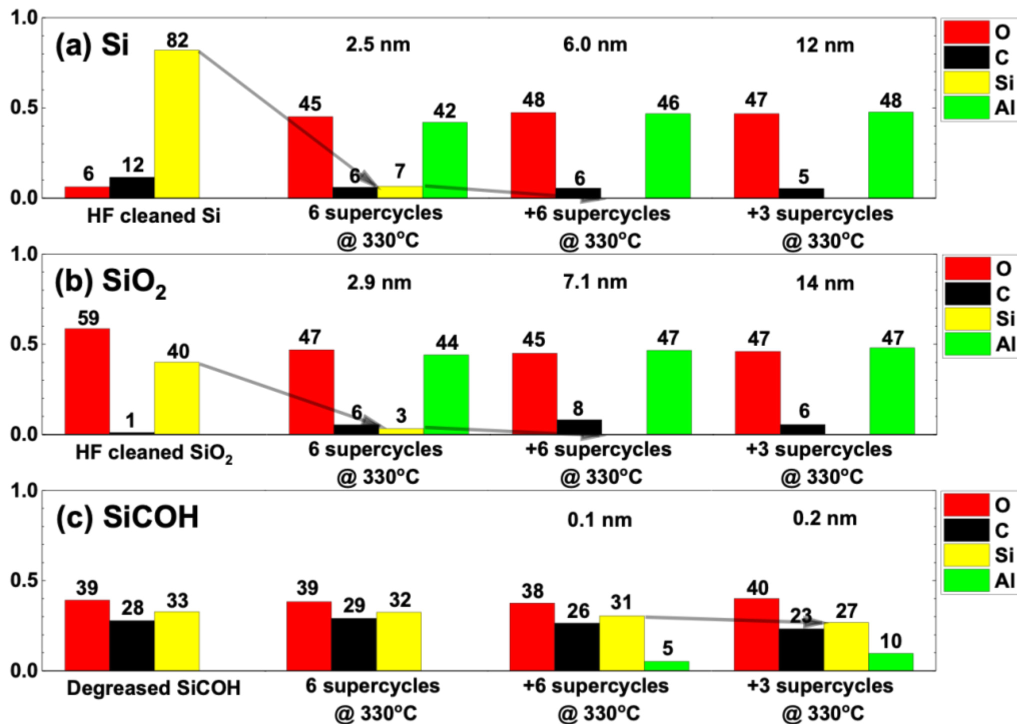

Figure 3.11 Analysis of AlO_x Pulsed CVD with one pulse of TMA and 80 pulses of ATSB per supercycle at 330°C. XPS chemical composition of (a) HF cleaned Si, (b) HF cleaned SiO_2, and (c) degreased SiCOH during AlO_x pulsed CVD with ATSB and TMA.

3.4.3 Mechanism and Nanoscale selectivity of the AlO_x pulsed CVD (TMA+ATSB)

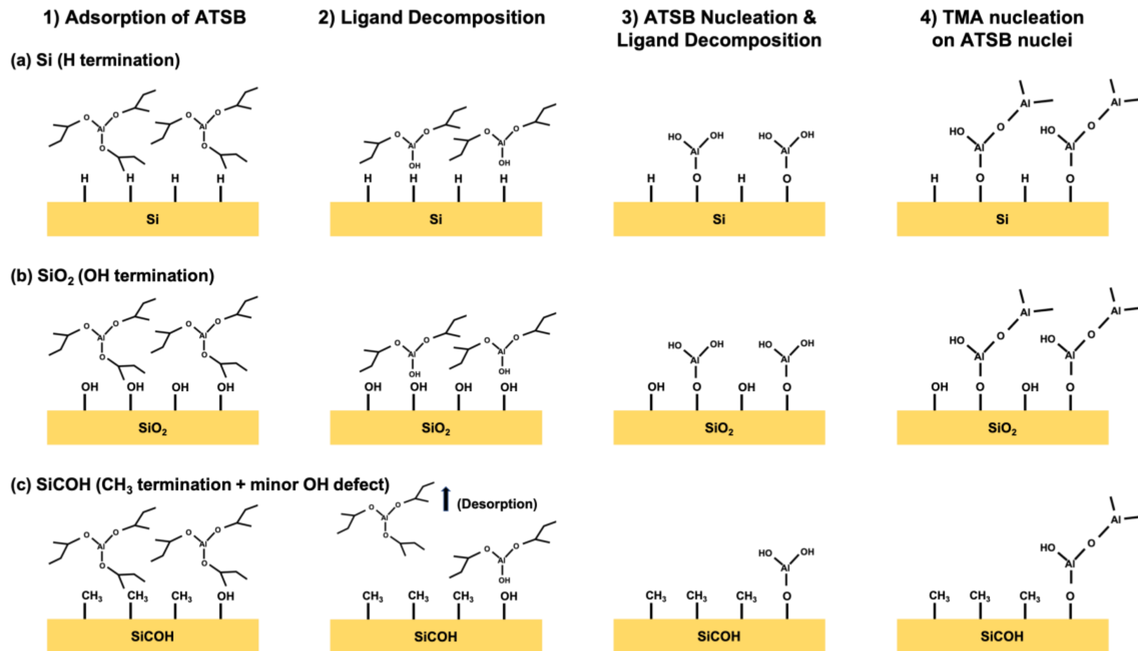

Figure 3.12 Proposed reaction mechanism of the AlO_x Pulsed CVD with TMA and ATSB. On (a) Si and (b) SiO_2, ATSB readily adsorbs and undergoes thermal decomposition due to the high density of reactive sites. On (c) SiCOH, there are only minor OH defective nucleation sites; thus, only a few ATSB nucleate while most ATSB desorb away. TMA can react on ATSB nuclei on surfaces, critically suppressing the further nucleation on SiCOH by leaving less reactive methyl ligands.

Based on the above study, the proposed mechanism of the AlO_x pulsed CVD with ATSB and TMA is shown in Figure 3.12. ATSB can adsorb on the sample surfaces. Due to high sample temperature, ligands start to thermally decompose and form reactive OH ligands. These OH ligands on adsorbed ATSB can react with H or OH bonds on Si and SiO_2, respectively. Si and SiO_2 have a high density of reactive sites, so ATSB can easily nucleate on them. However, the SiCOH surface has less reactive CH_3 bonds with only a minor number of OH defect sites; therefore, only a few adsorbed ATSB can react with the minor OH sites, and most ATSB are desorbed from the SiCOH surface. Conversely, TMA can react with OH

bonds on ATSB nuclei. However, TMA does not have oxygen in its ligands but only has less reactive methyl ligands. Therefore, when TMA reacts with AlO_x nuclei on the surface, it reduces the number of reactive sites and replaces them with less reactive methyl sites. For Si and SiO_2, unless too much TMA is dosed, there are still enough H or OH reactive sites for sequential film growth. However, as SiCOH has very few reactive sites or AlO_x nuclei, their reaction with TMA critically suppresses the further nucleation, inducing higher selective deposition with periodical TMA pulse during ATSB pulses.

Based on the mechanism, the AlO_x CVD with ATSB and TMA can be applied to other surfaces with OH bonds in preference to SiCOH. Metal, such as Cu, tends to form a metal oxide layer on the surface. Therefore, the AlO_x CVD with ATSB and TMA was dosed on Cu/SiCOH nanoscale patterned samples to test the process for nanoscale fabrication. For the AlO_x deposition, one pulse of TMA and 80 pulses of ATSB were dosed per supercycle at 330 °C sample temperature, which showed the highest selectivity.

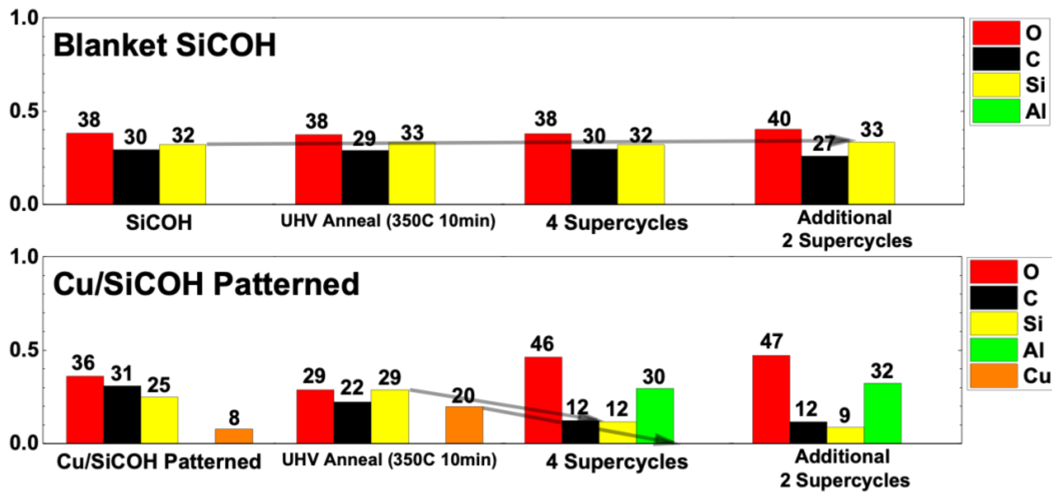

Figure 3.13 XPS of Selective AlO_x pulsed CVD with ATSB and TMA on a Cu/ SiCOH Nanoscale Patterned Sample. XPS chemical composition of blanket SiCOH and Cu/SiCOH patterned sample during the AlO_x pulsed CVD process with one pulse of TMA and 80 pulses of ATSB per supercycle at 330 ^{o}C sample temperature.

As shown in XPS chemical composition in Figure 3.13, the passivation on the Cu region of the patterned sample desorbed during the UHV anneal (350 °C 10 min) before the deposition process; the carbon fraction decreased, and the Cu fraction increased after the UHV anneal. This proves that the passivation selectively passivated the damaged SiCOH. After 6 supercycles of the AlO_x CVD process using one pulse of TMA and 80 pulses of ATSB per supercycle at 330 °C, the Cu peak was fully attenuated, consistent with selective deposition on the Cu surface. The Si percentage from the SiCOH surface of the patterned sample also decreased from 29 % to 9 %, while the blanket SiCOH was still clean.

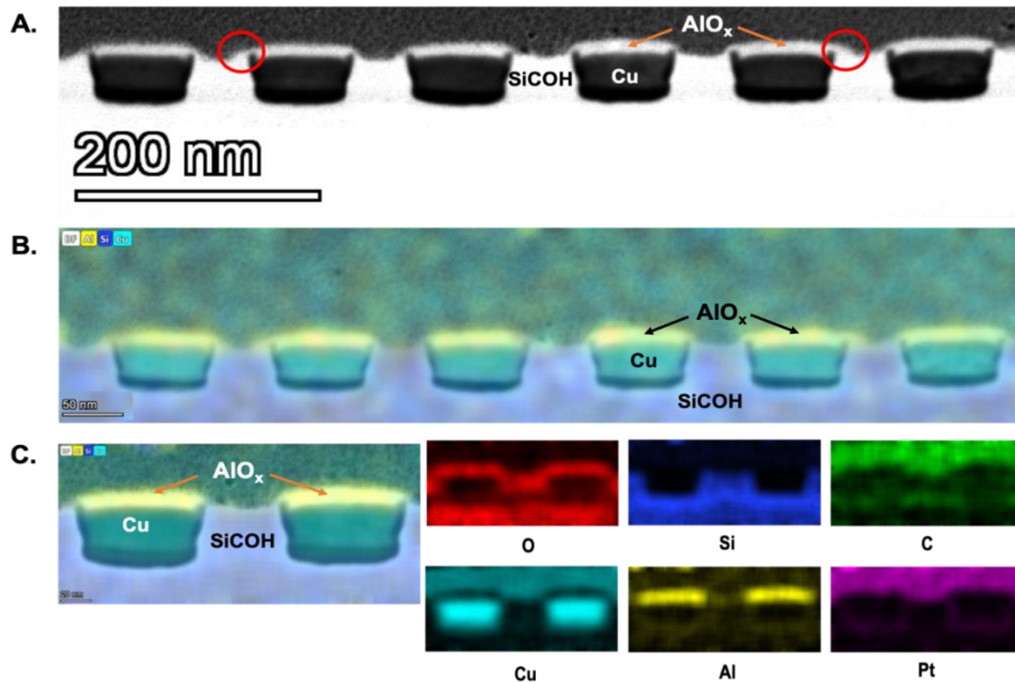

Figure 3.14 STEM Analysis of The Selective AlO_x Pulsed CVD with ATSB and TMA on a Nanoscale Patterned Sample (A) Wider view TEM image of Cu/SiCOH patterned sample after 6 supercycles of AlOx pulsed CVD with ATSB and TMA. (B) Magnified view of TEM and EDX images on each element.

Figure 3.14 shows the cross-sectional STEM image of the patterned sample after the CVD process in Figure 3.13 using one pulse of TMA and 80 pulses of ATSB per supercycle at 330 °C. The patterned sample surface was composed of Cu and SiCOH with around 90 nm and 50 nm widths, respectively. From the STEM images, around 10 nm of AlO_x was selectively deposited on the Cu surface. The selective deposition was confirmed by energy dispersive X-ray (EDX) analysis in Figure 3.14 B and 3.14 C. However, AlO_x had an isotropic growth that induced growth over the SiCOH surface (red circled region in Fig 3.14 A). Therefore, it is consistent with the Si percentage decrease only from the patterned sample. In addition, the AlO_x film showed a smooth surface in the STEM images. (see confirmation

by AFM below). By combining with selective AlO_x etch process[49] as an etch-back process, it could be possible to remove any unwanted nuclei from the SiCOH surface.

3.4.4 Film Morphology and Electrical Characteristics of the AlOx film

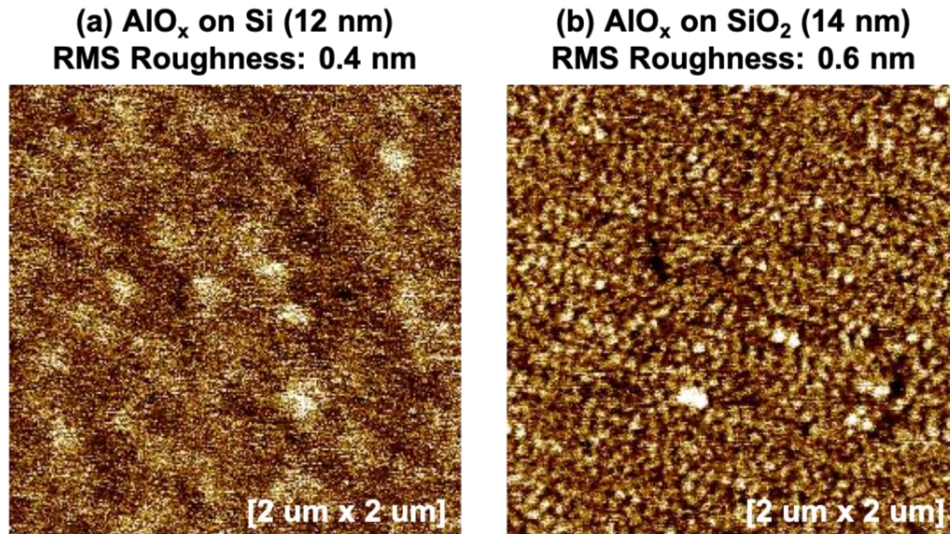

Figure 3.15 AFM image of AlO_x films on Si and SiO_2 deposited by the Pulsed CVD with ATSB and TMA at 330°C. AFM image of (a) 12 nm of AlO_x film on Si and (b) 14 nm of AlO_x film on SiO_2 deposited by the pulsed CVD with one pulse of TMA and 80 pulses of ATSB per supercycle at 330 °C sample temperature.

The ex-situ atomic force microscopy (AFM) was employed to check the film roughness. Figure 3.15 shows the AFM images of the AlO_x film on (a) Si and (b) SiO_2, deposited by the pulsed CVD with one pulse of TMA and 80 pulses of ATSB per supercycle at 330 °C sample temperature (the samples shown in Figure 3.11). The AlO_x film showed a smooth surface with 0.4 – 0.6 nm RMS roughness. This is advantageous compared to other oxides such as TiO_2 and HfO_2, which tend to form a rough surface with nm scale RMS roughness as film thickness increases due to the crystallization.[31,32]

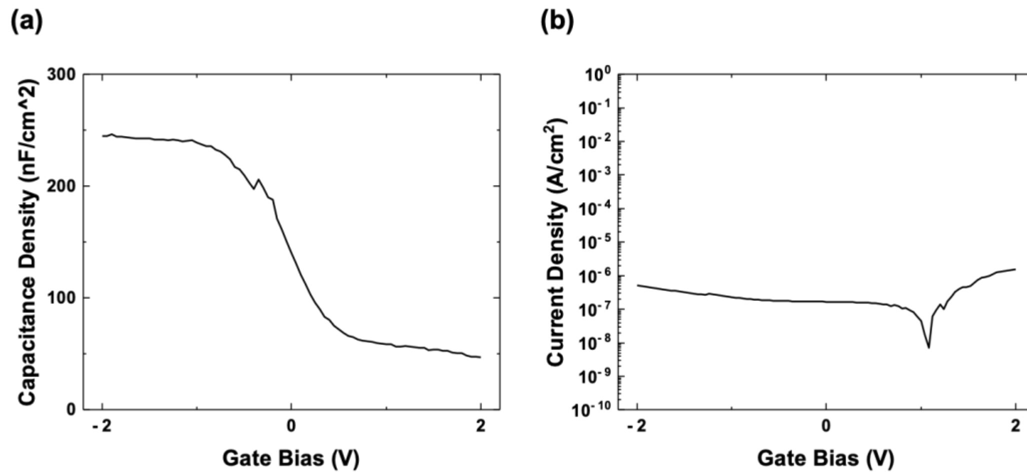

Figure 3.16 Electrical characteristics of the AlO_x film deposited by the Pulsed CVD with ATSB and TMA at 330°C. (a) Capacitance per unit area (1MHz) and (b) Leakage current density of the AlO_x film on Si substrate. The AlO_x film thickness was around 15 nm.

Capacitance-voltage (C-V) and leakage current (I-V) were measured to check the AlO_x film's characteristics as a dielectric material. A capacitor was made on 15 nm AlO_x film on a Si sample with Ni dot top electrode deposited. The C-V and I-V characteristics were measured from -2 V to 2 V, as shown in Figure 3.16.; however, similar results were obtained by the split I-V and C-V methods. The dielectric constant of the AlO_x film, estimated from the C-V curve (Fig 3.16 a), was around 4, which is lower than the usual dielectric constant of Al_2O_3. The lower dielectric constant is consistent with the AlO_x film in this process being oxygen-deficient.[50,51] The XPS chemical compositions above showed that the selective AlO_x CVD process had around a 1:1 ratio for Al:O, which means the AlO_x film was close to Al_1O_1 rather than Al_2O_3. The 1:1 Al:O ratio continued even after the post-deposition anneal, as shown in Figure 3.17. Figure 3.17 showed that the bulk of AlO_x film also had a 1:1 Al:O ratio. The leakage current after the post-deposition anneal was low

(around 10^{-6} A/cm^2 at ±2V as shown in Fig 3.16 b), showing the insulating behavior of the AlO_x film. In conclusion, as the selectively deposited AlO_x film was non-stoichiometric, it did not show the same behavior as Al_2O_3; however, it showed low k dielectric behavior with a dielectric constant close to SiO_2.

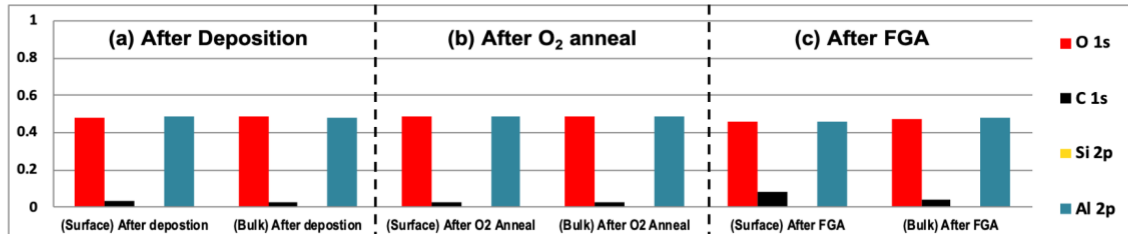

Figure 3.17 XPS chemical composition of the AlO_x film, deposited by the selective CVD with ATSB and TMA at 330 °C, before and after each post-deposition anneal. Surface sensitive (Left) and bulk sensitive (Right) XPS chemical composition of the 15 nm AlOx film on Si substrate. By increasing the angle between the XPS detector and the sample surface (30° → 60°), XPS can analyze the bulk-sensitive chemical composition of the film. Both surface/bulk sensitive XPS was analyzed after (a) the film deposition, (b) O_2 anneal, and (c) forming gas anneal. However, the AlOx film maintained a 1:1 Al:O ratio.

3.5 Conclusions

Inherent selective deposition of AlO_x through thermal pulsed CVD was studied. Aluminum tri-sec butoxide (ATSB) is a liquid metal alkoxide precursor, which has oxygen in each ligand. Through thermal decomposition, it can solely form an oxide film without a secondary oxygen precursor, such as water; it enables halogen and water-free selective oxide deposition, which can protect water-sensitive insulators (ex: SiCOH) and halogen-sensitive metal (ex: Cu) substrates. Due to the reactivity difference of ATSB on Si, SiO_2, and SiCOH, around 4-5 nm of AlO_x film was selectively deposited on Si and SiO_2 before significant nuclei

were deposited on SiCOH. With the combination of oxygen-rich metal alkoxide precursor ATSB and strong oxygen scavenger TMA, selective AlO_x pulsed CVD was developed. An adequate amount of TMA per supercycle inhibited the nucleation on SiCOH and increased the selective deposition on Si and SiO_2 to 12-14 nm at 330 °C sample temperature. The film was smooth with 0.4-0.6 nm RMS roughness. As the film was non-stoichiometric with a 1:1 Al:O ratio, the dielectric constant of the AlO_x was around 4, which is lower than the usual Al_2O_3 dielectric constant. The film showed around 10^{-6} A/cm^2 of leakage current, proving the film has insulating behavior. The AlO_x pulsed CVD with ATSB and TMA showed around 10 nm of selective deposition on the Cu region of the Cu/SiCOH nanoscale patterned sample. The AlO_x pulsed CVD combines the attributes of selectivity over 10 nm, a smooth film formation, and the potential to be readily etched since it is a uniform amorphous oxide. Therefore, it will be suitable as a spacer or mask in nanoscale MOSFET fabrication.

Chapter 3, in full, is currently being prepared for submission for publication of the material. Y. Cho, J. Huang, Z. Zhang, K. Wang, P.C. Lee, C. Kim, K. Wong, S. D. Nemani, E. Yieh, and A.C. Kummel. The dissertation author was the primary investigator and author of this material.

References

1. Atanasov, S.; Kalanyan, B.; Parsons, G. N. Inherent substrate-dependent growth initiation and selective-area atomic layer deposition of TiO2 using "water-free" metal-halide/metal alkoxide reactants, Journal of Vacuum Science and Technology A 34 (2016) 01A148.

2. Li, H.; Farmer, D. B.; Gordon, R. G.; Lin, Y.; Vlassak, J. Vapor Deposition of Ruthenium from an Amidinate Precursor, Journal of The Electrochemical Society 154 (12) (2007) D642-D647

3. www.beneq.com/en/technology (last access: Nov. 29th 2021)

4. Lee, Han-Bo-Ram; Bent, S. F.; A Selective Toolbox for Nanofabrication, Chem. Mater. 32 (2020) 3323-3324

5. Mackus, A. J. M.; Bol, A. A.; Kessels, W. M. M. The use of atomic layer deposition in advanced nanopatterning, Nanoscale 6 (2014) 10941-10960.

6. Choi, J. Y.; Ahles, C. F.; Cho, Y.; Anurag, A.; Wong, K. T.; Nemani, S. D.; Yieh, E.; Kummel, A. C. Selective pulsed chemical vapor deposition of water-free HfO_x on Si in preference to SiCOH and passivated SiO_2, Applied Surface Science 512 (2020) 145733

7. Yang, M.; Aarnink, A. A. I.; Schmitz, J.; Kovalgin, A. Y. Inherently area-selective hot-wire assisted atomic layer deposition of tungsten films, Thin Solid Films 649 (2018) 17-23.

8. Choi, J. Y.; Ahles, C. F.; Hung, R.; Kim, N.; Kummel, A. C. Selective atomic layer deposition of $MoSi_x$ on Si (001) in preference to silicon nitride and silicon oxide, Applied Surface Science 462 (2018) 1008-1016.

9. Lemaire, P. C.; King, M.; Parsons, G. N. Understanding inherent substrate selectivity during atomic layer deposition: Effect of surface preparation, hydroxyl density, and metal

oxide composition on nucleation mechanisms during tungsten ALD, J. Chem. Phys. 146 (2017) 052811.

10. Cao, K.; Cai, J.; Chen, R. Inherently Selective Atomic Layer Deposition and Applications, Chem. Mater. 32 (2020) 2195-2207

11. Bobb-Semple, D.; Nardi, K. L.; Draeger, N.; Hausmann, D. M.; Bent, S. F. Area-Selective Atomic Layer Deposition Assisted by Self-Assembled Monolayers: A Comparison of Cu, Co, W, and Ru, Chem. Mater. 31 (2019) 1635-1645.

12. Hashemi, F. S. M.; Bent, S. F. Sequential Regeneration of Self-Assembled Monolayers for Highly Selective Atomic Layer Deposition, Advanced Materials Interfaces 3 (2016) 1600464.

13. Hashemi, F. S. M.; Prasittichai, C.; Bent, S. F. A new resist for area selective atomic and molecular layer deposition on metal-dielectric patterns, The Journal of Physical Chemistry C 118 (2014) 10957.

14. Prasittichai, C.; Pickrahn, K. L.; Hashemi, F. S. M.; Bergsman, D. S.; Bent, S. F. Improving Area-Selective Molecular Layer Deposition by Selective SAM Removal, ACS Appl. Mater. Interfaces 6 (2014) 17831-17836.

15. Hashemi, F. S. M.; Birchansky, B. R.; Bent, S. F. Selective Deposition of Dielectrics: Limits and Advantages of Alkanethiol Blocking Agents on Metal−Dielectric Patterns, ACS Appl. Mater. Interfaces 8 (2016) 33264−33272.

16. Mameli, A.; Karasulu, B.; Verheijin, M. A.; Barcones, B.; Macco, B.; Mackus, A. J. M.; Kessels, W. M. M. E.; Roozeboom, F. Area-Selective Atomic Layer Deposition of ZnO by Area Activation Using Electron Beam-Induced Deposition, Chem. Mater. 31 (2019) 1250-1257.

17. Mameli, A.; Kuang, Y.; Aghaee, M.; Ande, C. K.; Karasulu, B.; Creatore, M.; Mackus, A. J. M.; Kessels, W. M. M.; Roozeboom, F. Area-Selective Atomic Layer Deposition of In_2O_3:H Using a u-Plasma Printer for Local Area Activation, Chem. Mater. 29 (2017) 921-925.

18. Farm, E.; Lindroos, S.; Ritala, M.; Leskela, M. Microcontact Printed RuO_x Film as an Activation Layer for Selective-Area Atomic Layer Deposition of Ruthenium, Chem. Mater. 24 (2012) 275-278.

19. Mackus, A. J. M.; Mulders, J. J. L.; van de Sanden, M. C. M.; Kessels, W. M. M. Local deposition of high-purity Pt nanostructures by combining electron beam induced deposition and atomic layer deposition, Journal of Applied Physics 107 (2010) 116102.

20. Chaukulkar, R. P.; Agarwal, S. Atomic layer deposition of titanium dioxide using titanium tetrachloride and titanium tetraisopropoxide as precursors, Journal of Vacuum Science and Technology A 31 (2013) 031509.

21. Anderson, V. R.; Cavanagh, A. S.; Abdulagatov, A. I.; Gibbs, Z. M.; George, S. M. Waterless TiO_2 atomic layer deposition using titanium tetrachloride and titanium tetraisopropoxide, Journal of Vacuum Science and Technology A 32 (2014) 01A114.

22. Ramos, K. B.; Clavel, G.; Marichy, C.; Cabrera, W.; Pinna, N.; Chabal, Y. J. In Situ Infrared Spectroscopic Study of Atomic Layer-Deposited TiO2 Thin Films by Nonaquesous Routes, Chem. Mater. 25 (2013) 1706-1712.

23. McGahay, V. Porous Dielectrics in Microelectronic Wiring Applications, Materials 3 (2010) 536-562.

24. Grill, A. Plasma enhanced chemical vapor deposited SiCOH dielectrics: from low-k to extreme low-k interconnect materials, Journal of Applied Physics 93 (2003) 1785.

25. Edelstein, D. C.; Gates, S. M.; Grill, A.; Lane, M.; Miller, R. D.; Neunmayer, D. A.; Nguyen, S. V. SiCOH dielectric material with improved toughness and improved Si-C bonding, semiconductor device containing the same, and method to make the same. US 2005/0194619 A1.

26. Canaperi, D. F.; Nguyen, S. V.; Priyadarshini, D.; Shobha, H. K. Advanced ultra low k SiCOH dielectrics prepared by built-in engineered pore size and bonding structured with cyclic organosilicon. US 9209017 B2.

27. Triyoso, D. H.; Hegde, R. I.; Zollner, S.; Ramon, M. E.; Kalpat, S.; Gregory, R.; Wang, X. -D.; Jiang, J.; Raymond, M.; Rai, R.; Werho, D.; Roan, D.; White, B. E. Jr.; Tobin, P. J. Impact of titanium addition on film characteristics of HfO_2 gate dielectrics deposited by atomic layer deposition, Journal of Applied Physics 98 (2005) 054104.

28. Triyoso, D. H.; Hegde, R. I.; Wang, X. -D.; Stoker, M. W.; Rai, R.; Ramon, M. E.; White, B. E. Jr.; Tobin, P. J. Characteristics of Mixed Oxides and Nanolaminates of Atomic Layer Deposited HfO_2-TiO_2 gate Dielectrics, Journal of The Electrochemical Society 153(9) (2006) G834-G839.

29. Sasaki, T.; Ebina, Y.; Kitami, Y.; Watanabe, M. Two-Dimmensional Diffraction of Molecular Nanosheet Crytallites of Titanium Oxide, J. Phys. Chem. B 105 (2001) 6116-6121

30. Shchukarev, A. V.; Korolkov, D. V. XPS Study of Group IA Carbonates, Central European Science Journals 2(2) (2004) 347-362

31. Rammula, R.; Aarik, J.; Mandar, H.; Ritslaid, P.; Sammelselg, V. Atomic layer deposition of HfO2: Effect of structure development on growth rate, morphology and optical properties of thin films, Applied Surface Science 257, (2010) 1043-1052.

32. Cho, Y.; Ahles, C. F.; Choi, J. Y.; Huang, J.; Jan, A.; Wong, K.; Nemani, S.; Yieh, E.; Kummel, A. C.; Inherently Selective Water-Free Deposition of Titanium Dioxide on the Nanoscale: Implications for Nanoscale Patterning, ACS Appl. Nano Mater. 5, 1 (2022) 476-485.

33. Suh, T.; Yang, Y.; Zhao, P.; Lao, K. U.; Ko, H. Y.; Wong, J.; DiStasio Jr, R. A.; Engstrom, J. R.; Competitive Adsorption as a Route to Area-Selective Deposition, ACS Appl. Mater. Interfaces 12 (2020) 9989-9999.

34. Testoni, G. E.; Chiappim, W.; Pessoa, R. S.; Fraga, M. A.; Miyakawa, W.; Sakane, K. K.; Galvao, N. K. A. M.; Vieira, L.; Maciel, H. S.; Influence of the Al_2O_3 partial-monolayer number on the crystallization mechanism of TiO_2 in ALD TiO_2/Al_2O_3 nanolaminates and its impact on the material properties, *J. Phys. D: Appl. Phys.* 49 (2016) 375301.

35. Elam, J. W.; Sechrist, Z. A.; George, S. M.; ZnO/ Al_2O_3 nanolaminates fabricated by atomic layer deposition: growth and surface roughness measurements, Thin Solid films 414 (2002) 43-55.

36. Igor Iatsunskyi; Coy, E.; Viter, R.; Nowaczyk, G.; Jancelewicz, M.; Baleviciute, I.; Zaleski, K.; Jurga, S.; Study on Structural, Mechanical, and Optical properties of Al_2O_3-TiO_2 Nanolaminates Prepared by Atomic Layer Deposition, J. Phys. Chem. C 119 (2015) 20591-20599.

37. Hausmann, D. M.; Gordon, R. G.; Surface morphology and crystallinity control in the atomic layer deposition (ALD) of hafnium and zirconium oxide thin films, Journal of Crystal Growth 249 (2003) 251-261.

38. Lee, B.; Hande, A.; Park, T. J.; Chung, K. J.; Ahn, J.; Rousseau, M.; Hong, D.; Li, H.; Liu, X.; Shenai, D.; Kim, J.; ALD of $LaHfO_x$ nano-laminates for high-k gate dielectric applications, Microelectronic Engineering 88 (2011) 3385-3388

39. Huang, J.; Cho, Y.; Zhang, Z.; Jan, A.; Wong, K. T.; Nemani, S.; Yieh, E.; Kummel, A. C.; Selective Pulsed Chemical Vapor Deposition of Water-Free TiO_2/Al_2O_3 and HfO_2/Al_2O_3 Nanolaminates on Si and SiO2 in Preference to SiCOH, ACS Appl. Mater. Interfaces (2022) 14, 13, 15716-15727

40. Kang, P. S.; Woo, J. C.; Joo, Y. H.; Kim, C. I.; Etch characteristics of HfO_2 thin films by using CF_4/Ar inductively coupled plasma, Vacuum 93 (2013) 50-55.

41. Hotovy, I.; Hascik, S.; Gregor, M.; Rahacek, V.; Predanocy, M.; Plecenik, A.; Dry etching characteristics of TiO_2 thin films using inductively coupled plasma for gas sensing, Vacuum 107 (2014) 20-22.

42. Choi, K. R.; Woo, J. C.; Joo, Y. H.; Kim, C. I.; Dry etching properties of TiO_2 thin films in O_2/CF_4/Ar plasma, Vacuum 92 (2013) 85-89.

43. Tegen, S.; Moll, P.; Etch Characteristics of Al_2O_3 in ICP and MERIE Plasma Etchers, Journal of The Electrochemical Society, 152 (4) (2005) G271-G276

44. Cho, Y.; Huang, J.; Ahles, C. F.; Zhang, Z.; Wong, K.; Nemani, S.; Yieh, E.; Kummel, A. C.; Inherent Selective Pulsed Chemical Vapor Deposition of Amorphous Hafnium Oxide/Titanium Oxide Nanolaminates, Applied Surface Science 600 (2022) 154010.

45. Chen, H. P.; Wu, Y. H.; Huang, H. Y.; Tsai, C. H.; Lee, S. K.; Lee, C. C.; Wei, T. H.; Yao, H. C.; Wang, Y. C.; Liao, C. Y.; Chang, H. K.; Lu, C. W.; Shue, Winston S.; Cao Min; Fully Self-Aligned Via Integration for Interconnect Scaling beyond 3nm Node, IEEE IEDM 21-486 (2021)

46. Nguyen, S. V.; Shobha, H.; Peethala, C. B.; Haigh, T.; Huang, H.; Li, J.; Demarest, J.; Haran, B.; Hausmann, Dennis; Lemaire, P.; Sharma, K.; Ramani, P.; Mahorowala, A.; Selective deposition of AlOx for Fully Aligned Via in nano Cu interconnects, IEEE IITC (2021) S7-4

47. Cao, L.; Mattelaer, F.; Sajavaara, T.; Dendooven, J.; Detavernier, C.; A liquid alkoxide precursor for the atomic layer deposition of aluminum oxide films, J. Vac. Sci. Technol. A 38 (2) Mar/Apr (2020)

48. Liu, T. L.; Bent, S. F.; Area-Selective Atomic Layer Deposition on Chemically Similar Materials: Achieving Selectivity on Oxide/Oxide Patterns, Chem. Mater. 33,2, 513-523 (2021)

49. Yang, X.; Woo, J. C.; Um, D. S.; Kim, C. I.; Dry Etching of Al_2O_3 Thin Films in $O_2/BCl_3/Ar$ inductively Coupled Plasma, Trans. Electr. Electron. Mater. 11(5) 202 (2010)

50. Hamelmann, F.; Heinzmann, U.; Szekeres, A.; Kirov, N.; Nikolova, T.; Deposition of silicon oxide thin films in TEOS with addition of oxygen to the plasma ambient: IR spectra analysis, Journal of Optoelectronics and Advance Materials Vol. 7, No. 1, February (2005) p. 389-392

51. Kassmi, M.; Pointet, J.; Gonon, P.; Bsiesy, A.; Vallee, C.; Jomni, F.; Low-frequency dielectric properties of intrinsic and Al-doped rutile TiO_2 thin films grown by the atomic layer deposition technique, J. Appl. Phys. 119 (2016) 244101